AN EXPERIMENTAL STUDY OF COAXIAL TURBULENT MIXING OF LIQUID AND GASEOUS FUEL WITH AIR

C. W. LaPointe

This document is subject to special export controls and each transmittal to foreign governments or foreign nationals may be made only with prior approval of the Air Force Aero Propulsion Laboratory, ARPC, Wright Patterson Air Force Base Ohio 45433.

FOREWORD

This report covers work performed on contract number F33615-67-C-1122, BPS 7(63-301201-62405214) during the period 15 November 1967 through 15 November 1968 at The University of Michigan. The work, sponsored by the Air Force Aero Propulsion Laboratory and monitored by W. Lee Bain, is directed toward problems arising in the development of SCRAMJET. The author, whose Ph. D. topic is derived from this research, gratefully acknowledges this support.

Helpful guidance has been provided by the author's Doctoral Committee: Professor J. A. Nicholls, Dr. F. S. Simmons, Professor A. M. Kuethe and Assistant Professor V. Kibens. Assistant Professor S. W. Bowen was particularly helpful during the initial design phases of this research. Messers D. E. Geister, C. J. Iott, W. J. Lane, G. Banasiak and L. J. Oswald contributed materially to the experimental program.

This report was submitted by the author on 3 June 1969.

Publication of this report does not constitute Air Force Approval of the report's findings or conclusions. It is published only for the exchange and stimulation of ideas.

ABSTRACT

Non-interfering means have been used to measure fluid concentration in non-homogeneous media. Light scattering and absorption spectroscopy are applied to gas-liquid and gas-gas axisymmetric diffusion respectively. Path-integrated transmission measurements are point-resolved by means of the Abel transformation. Centerline values are obtained either by numerical Abel inversion or by a graphical technique.

Water, centrally injected into a Mach three coaxial air jet, displays monodisperse light scattering characteristics. The droplet diameter, determined from transmission measurements at two wavelengths (1.6 and 2.38 microns), is 7.35 ± 0.10 microns throughout the jet. The measurements are obtained at an initial mass flux ratio, $\rho u_w / \rho u_a = 0.44$, and between the axial stations, $17 < (z/r_o) < 43$ ($r_o = 0.893$ cm, the outer jet's exit radius). The monodisperse behavior or, equivalently, the narrowness of the particle size distribution is attributable to turbulent shear stresses causing water jet disintegration. This narrowing of the range of surviving particle sizes increases with relative airstream velocity.

Particle number density profiles are obtained as a function of jet radial position and axial distance. Two regions, corresponding to the outer jet's potential core and subsequent fully developed region, are investigated. In the potential region, the droplet density radial distribution

is gaussian. The centerline particle density decays as $z^{-5/3}$ in the potential region; as $z^{-7/3}$ in the fully developed region. The jet width spreads linearly with axial distance in the potential region and as $z^{5/3}$ in the fully developed region. The average particle velocity, computed from particle density profiles and the overall water mass flow rate, varies as $z^{-1/3}$ in the potential region and as z^{-1} in the fully developed region. There is no average slip velocity between the particles and surrounding air jet in the regions investigated.

Increasing the initial mass flux ratio has the effect of increasing particle density according to the relation, $N \sim (\rho u_w/\rho u_a)^{2/3}$. The jet width varies as, $r_N \sim (\rho u_w/\rho u_a)^{1/12}$. These relations hold in the range, $0.15 < (\rho u_w/\rho u_a) < 1.5$.

A non-interfering diagnostic system utilizing absorption spectroscopy and a tracer gas (HF) has also been developed to study gas-gas axisymmetric mixing. Functions are developed for the interpretation of absorption data in terms of absorber density and temperature.

In the course of HF mass flow calibration, a measurement of the viscosity of gaseous HF has been obtained. Derived from the Reynolds number dependence of the flow measuring orifice, the values obtained for a temperature of 90^{o}F lie between 7.8×10^{-7} and 9.5×10^{-7} lb sec/ft^2.

TABLE OF CONTENTS

LIST OF ILLUSTRATIONS

NOMENCLATURE

Symbol		Units
$A(f)$	voltage amplitude spectrum	volts/Hz
a	Voigt parameter	
a_λ	fractional attenuation due to scattering	
a_ν	spectral absorptance	
B_e	HF line spacing 20.939	cm^{-1}
$B_{j,k}$	weighting coefficients defined by Eq. (54)	
b	half-width at half-height spectral line	cm^{-1}
C	orifice discharge coefficient	
c	speed of light	$3x10^{10}$ cm/sec
$\mathcal{D}$	detectivity	$cm\sqrt{Hz}$/watt
D	particle diameter	μ
D_t	eddy diffusivity	cm^2/sec
E	state energy	ergs
e	2.7183	
$\mathcal{F}_N, \mathcal{F}_p$	temperature functions defined by Eq. (114) and (117)	
f	frequency	Hz
f_J	oscillator strength	
$f/$	optical "speed"	
$\mathcal{J}_N, \mathcal{J}_p$	temperature functions defined by Eq. (120) and (123)	
g	statistical weight	
$g(\nu-\nu_m)$	slit function	
h	Planck's constant 6.6251×10^{-27}	erg-sec
I_λ	spectral radiance	watts $ster^{-1}$ μ^{-1} cm^{-2}
I_ν	spectral radiance	watts $ster^{-1}$ μ^{-1} cm^{-2}

Symbol		Units
i	$\sqrt{-1}$	
J	rotational quantum number	
j	transverse coordinate index	
j_ν	spectral emission coefficient	watts ster^{-1} cm cm^{-3} atm^{-1}
K_λ	scattering extinction coefficient	cm^{-1}
K_s	scattering-area coefficient	
k	Boltzmann's constant	1.38x10^{-16} erg/^{o}K
k	radial coordinate index	
k_ν	spectral absorption coefficient	cm^{-1} atm^{-1}
L	optical path length	cm
Le_t	turbulent Lewis number	
ℓ	optical path coordinate	cm
M	Mach number	
$\mathcal{M}$	molecular weight	gm/gm mole
m	mass	gm
$\dot{m}$	mass flow rate	lb/sec
N	number density	cm^{-3}
n	diffraction order	
P_N	noise power spectrum	watts/Hz
Pr_t	turbulent Prandtl number	
p	pressure	atm
Q	partition function	
R	jet radius	cm
$\mathcal{R}$	responsivity	volts/watt
r	radial coordinate	cm

Symbol		Units
r_o	exit radius outer jet	cm
r_1	particle density integral radius, Eq. (61)	cm
r_2	particle density integral radius, Eq. (62)	cm
r_K	half radius scattering coefficient profile	cm
r_N	half radius number density profile	cm
r_W	half radius equivalent width profile	cm
Sc_t	turbulent Schmidt number	
S_J	line strength	$cm^{-2}\ atm^{-1}$
S_1	specific responsivity	$watt/cm^2$
T	temperature	^oK
t	time	seconds
u	axial velocity	cm/sec
V	electrical potential	volts
v	radial velocity	cm/sec
v	vibrational quantum number	
W_ν	equivalent width	cm^{-1}
X	absorption variable defined by Eq. (127)	
X_j	Abel program input (Eq. 55)	
x	$pSL/2\pi b$	
Y_s	mass fraction of species "s"	
y	transverse coordinate	cm
y_W	half width equivalent width profile	cm
z	axial coordinate	

Symbol		Units
α	$\pi D/\lambda$, scattering parameter	
α_s	broadening efficiency	
ϵ	eddy kinematic viscosity	cm^2/sec
$\phi(\alpha)$	particle distribution function	
$\Delta\nu$	spectral slit width	cm^{-1}
Λ	filter transmission	
λ	wavelength	μ
μ	coefficient of viscosity	$lb\ sec/ft^2$
ν	wavenumber	cm^{-1}
ρ	density	gm/cm^3
$\rho u_w/\rho u_a$	initial mass flux ratio inner to outer jet	
τ	time constant	sec
Ω	solid angle	steradians
ω_e	HF band center 4138.52	cm^{-1}

Subscripts

a	air
c_i	inner core
c_o	outer core
D	Doppler
ℓ	lower state
m	line center
s	species "s"
u	upper state
w	fuel

Superscripts

$\bar{(\ )}$	average
$(')$	fluctuating

SECTION I

INTRODUCTION

Fluid transport phenomena determine the efficiency if not the feasibility of many devices. Yet, except for idealized situations, performance prediction is largely an empirical procedure. Such is the case with the supersonic combustion ramjet (SCRAMJET). The task to be performed here is to efficiently mix fuel with supersonic air and then to extract the fuel's energy within a reasonable combustor length. The little understood areas of high speed, turbulent, compressible diffusion and combustion are introduced in this application.

It is well established that fluid transport (mass, momentum, energy) in turbulent flow is considerably enhanced in comparison to its laminar equivalent. The specification of turbulent transport, in terms of fluid properties, is by no means as complete as the specification of laminar transport is in terms of molecular properties, however. Indeed, whereas molecular transport depends only on conditions at a point, eddy transport depends on conditions removed from the point in question, on the past history of the fluid itself.

There are two ways of attacking turbulence problems: statistically and phenomenologically. The former method, involving correlations and spectra of fluctuations is elegant mathematically but difficult to apply in anything but homogeneous isotropic turbulence. The main

diagnostic tool of this method is the hot wire anemometer which cannot, as yet, be used in combusting flows. Mention is made of this approach because of the insight which it lends toward the interpretation of phenomenological coefficients. The latter approach involves the description of events by the same formulae used to describe laminar phenomena; the various transport coefficients being modified accordingly. The coefficients, eddy diffusivity (D_t), eddy kinematic viscosity (ϵ), and eddy conductivity (κ), are determined empirically. This determination, in terms of flow variables, presents the central problem.

There are several theories, useful in restricted situations, which attempt to describe these coefficients. Prandtl's mixing length theory[1], analogous to the mean free path concept of molecular viscosity, is useful for the description of ϵ in certain types of flows. Taylor's vorticity transfer theory[2] yields better agreement with experiment for other flows. The flows where either apply are subsonic and hence, incompressible. Attempts[3,4,5] at extending either hypothesis to compressible flows have met with limited success. A simple extension to flows with variable density has not as yet been found.

In order to better predict supersonic diffusion phenomena, a number of probe type experiments have been performed[5,6,7]. These have usually taken the form of species (thermal conductivity cell),

velocity (pitot) and enthalpy (energy balance) probes. Quantities of interest in coaxial mixing situations are the centerline decay of fuel concentration and velocity, the rate of apreading of the fuel jet and the form of concentration profiles. Correlation of these variations with initial fuel/air mass flux ratio has been attempted[5]. In the case of centerline fuel concentration, for example, the axial variation has exhibited a power-law dependence ranging from z^{-1} to z^{-2}. Why this happens is the subject of on-going speculation[3].

This report describes the development of diagnostic techniques which may be applied, in situ, to the determination of flow behavior under conditions pertinent to SCRAMJET. The measurements are, of necessity, made in a non-interfering manner and fall into two independent categories: light scattering and spectroscopy. The former technique is applied to the supersonic mixing of liquid fuel with air. Experimental results and their interpretation are developed and reported in Section IV. The spectroscopic technique, applied to a tracer gas m molecule (HF), is described and the data reduction developed in Section V; experiments are currently under way. In the next section, the fluid mechanical formulation of axisymmetric turbulent mixing is summarized and problem areas outlined.

SECTION II

FLUID MECHANICAL DESCRIPTION OF AXISYMMETRIC TURBULENT FLUID MIXING

A. INTRODUCTION

In this section, the mathematical framework is presented for the description of compressible turbulent mixing of dissimilar co-flowing fluids. Care must be exercised when attempting to describe such flow solely by a gradient diffusion—turbulent exchange coefficient type of analysis because density variations arise from more than one cause. The experimental configuration is described and various magnitudes defined.

B. DEFINITIONS

We consider axisymmetric coaxial jets in which the outer annular jet is air while the central (injector) jet is fuel (gas or liquid). The jets exhaust into still air. In the absence of a central jet, a supersonic submerged air jet will itself constitute a mixing situation. There will be ambient air mass entrained throughout its length. Associated with a perfectly expanded supersonic jet, as in the subsonic case, is a uniform velocity region called the potential core, (Fig. 1). Its length, z_{c_o}, is dependent upon Mach number. According to the theory of Abramovich[2],

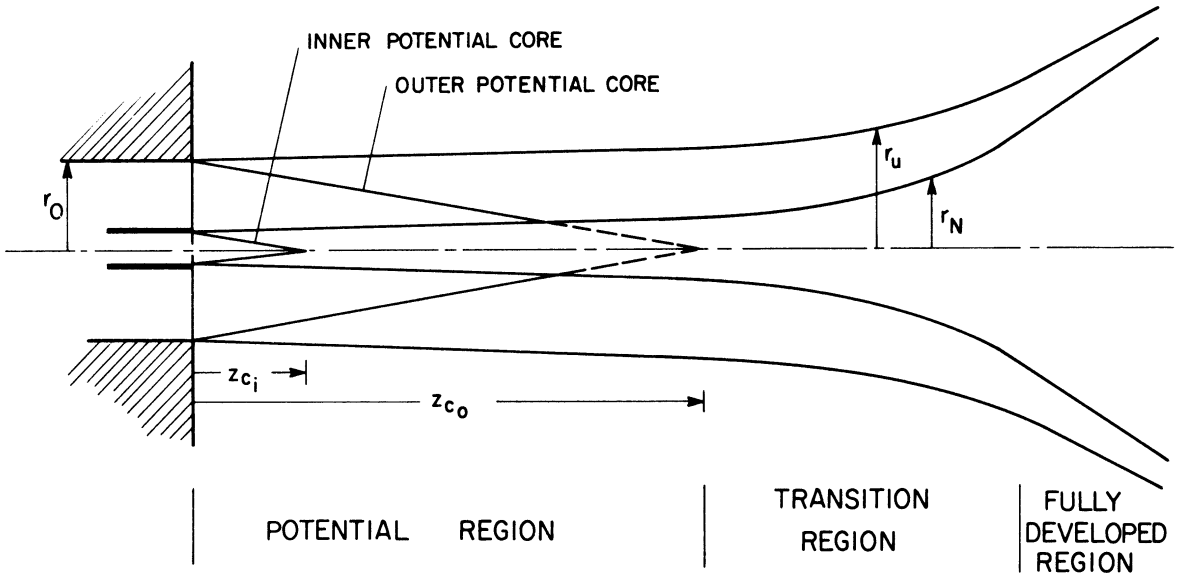

Figure 1. Supersonic Coaxial Free Jet Mixing Configuration

it is approximately 24 nozzle radii in length for an exit Mach number of three. Introduction of an additional jet (the injector) actually presents a three-fluid mixing problem even if all three fluids are air. The inner jet also possesses a potential core of length, z_c.

The classification of jet subregions, according to the behavior of velocity profiles, usually includes an initial (potential) region followed by a so-called transition region and ultimately a fully developed region wherein velocity profiles exhibit similarity behavior. It is seen that, when there are two jets, the number of possible subregion classifications is increased. In the interest of brevity, we will base our classification on the outer jet's behavior noting that the inner jet can not be fully developed without the outer jet's being in the same physical state. These regions are delineated in Fig. 1.

It should be mentioned that, with a central injector, the outer potential core is actually a wedge-shaped annulus whose inner boundary is defined by the region of influence of the injector exit periphery. The magnitude of z_{c_o} is therefore much less than is indicated in the figure. We note, however, that the concept of a potential core is an approximation based on the neglect of boundary layer influence internal to the nozzle. If the injector area is a small fraction of the outer jet's area, its influence could be equally small. At any rate, it shall be shown (Sec. IV) that the virtual position, z_{c_o}, does indeed mark the beginning of a transition region in flows with small overall fuel/air ratio.

The majority of fluid mixing studies to date have dealt with like fluid (unary) mixing such as, e.g., heated air mixing with cooler air or simply moving air mixing with still air. Under these circumstances, a dimension associated with the radial profile of the axial component of velocity, u, may be used to characterize the jet's boundaries. In practice, that radius, r_u, at which u is equal to one-half its centerline value, u(o), is commonly employed. For low speed flows of air into air, velocity is the only quantity which varies perceptibly throughout the flow field. It is therefore possible to correlate local mixing layer velocity profiles by the parameter u_i/u_o, the inner to outer stream velocity ratio.

If now the jet's exhaust velocity is increased to the point where compressibility is influential, not only the velocity, but density, ρ, and static temperature, T, vary across the jet.* Typical profiles of u, ρ, T, and ρu, for a single compressible free air jet whose stagnation temperature is equal to the ambient temperature are sketched in Fig. 2. In order to describe the jet spreading in this case, one must discuss many profiles. As in the subsonic case where mixing layer correlation is obtained with

---

*The static pressure, consistent with the boundary layer approximations is assumed constant over the flow field There are, of course, conditions which can invalidate this assumption[8].

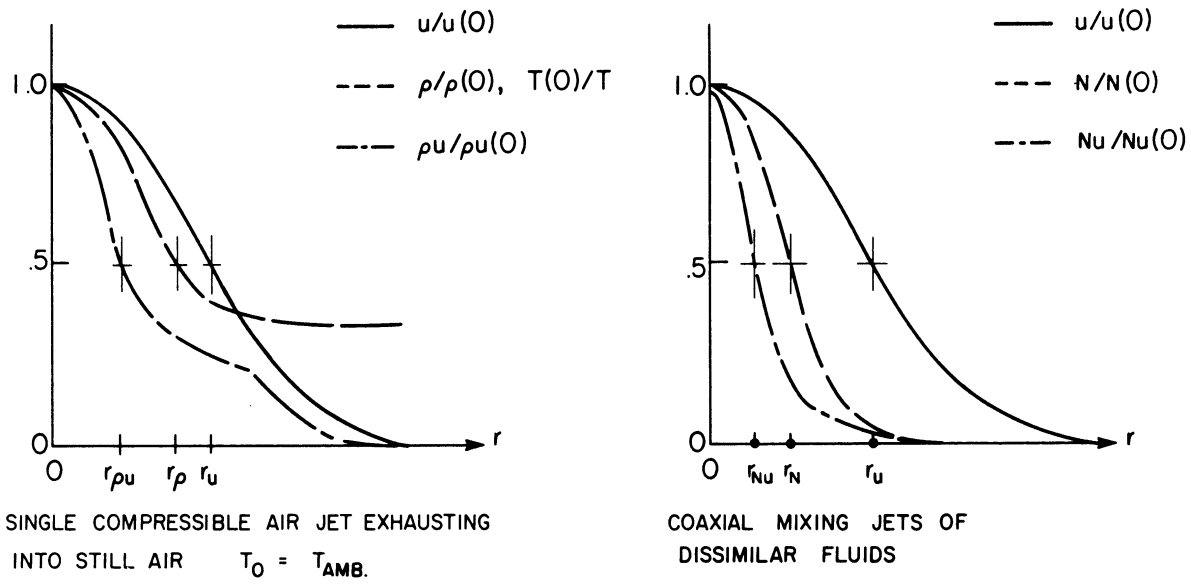

Figure 2. Radial Profiles of Velocity, Density, and Mass Flux in Compressible Unary and Binary Gas Mixing

the velocity ratio, a natural parameter to consider for compressible correlation is the mass flux ratio, $\rho u_i/\rho u_o$. One may also wish to attempt to fully describe the jet width by the half-radius, $r_{\rho u}$, of the mass flux profile. Difficulty is encountered in the latter endeavor because density does not go to zero at a jet boundary. The compressible ρu profile therefore exhibits a plateau which could render ambiguous the determination of $r_{\rho u}$. The grouping $\left[\rho(r) - \rho_\infty\right] / \left[\rho(o) - \rho_\infty\right]$ does go to zero and has been used in theoretical treatments which ascribe an analytical dependence to it. The half-radius of this profile is, of course different than r_ρ.

Considering the situation in which a different gas, whose number density is N, mixes subsonically with a surrounding free jet, it is seen that the profile, N(r), does go to zero at the inner jet's boundary but that this boundary does not generally coincide with the edge of the outer jet's velocity profile. The half radii in this case obey $r_{Nu} < r_N < r_u$. Thus it is seen that density profiles, in these two different situations, do not share a common boundary with velocity.

The reason for stressing these features stems from the fact that, for a single incompressible heated jet exhausting into still air, Reichardt's[9] inductive theory of turbulent mixing leads to the simple relation

$$\frac{T(r) - T_\infty}{T(o) - T_\infty} = \left[\frac{u}{u(o)}\right]^{Pr_t} \tag{1}$$

between temperature and velocity. A similar relation presumably would exist between density and velocity wherein the exponent would be the turbulent Schmidt number, Sc_t. Clearly, for these relations to hold, both profiles must share a common boundary. For this simple situation, the value of Pr_t is given by Taylor's[10] vorticity transfer theory as $Pr_t = 0.5$.

Presuming such a relation to hold for the purely compressible situation, it is instructive to estimate the value which Pr_t would assume. This may be accomplished by considering the one-dimensional energy equation and assuming stagnation temperature to be constant throughout the flow. The value Pr_t would assume in this, non-mixing, case is two. Extrapolating this result to the situation where both binary mixing and compressibility are influential, the effective turbulent Prandtl number obtained from such a relation would presumably lie between 2 and 0.5 if a single value could be obtained at all.

Describing axisymmetric mixing profiles by an approximate analytic function reveals certain gross features concerning the behavior of the various half-radii. A simple gaussian profile is a fairly good approximation out to moderate radii[6]. Thus

$$\frac{T(r) - T_\infty}{T(o) - T_\infty} = e^{-\ln 2\left(\frac{r}{r_T}\right)^2} \tag{2}$$

and

$$\frac{u(r)}{u(o)} = e^{-\ln 2\left(\frac{r}{r_u}\right)^2} \tag{3}$$

where r_T and and r_u are the half radii of temperature difference and velocity respectively. Inserting these relations into Eq. 1 yields

$$Pr_t = \left(\frac{r_u}{r_T}\right)^2 \tag{4}$$

A similar expression involving density and velocity yields

$$Sc_t = \left(\frac{r_u}{r_\rho}\right)^2 \tag{5}$$

If $Pr_t = Sc_t = 1$, all profiles coincide with each other. Experiments of single jet fluid mixing [11, 12, 6] have generally been in agreement that

$$Pr_t \simeq 0.7$$

$$Sc_t \simeq 0.7 \tag{6}$$

$$Le_t = \frac{Pr_t}{Sc_t} = \left(\frac{r_\rho}{r_T}\right)^2 = 1$$

That is, density and temperature diffuse at an equal rate which is faster than that of momentum. Although these simple relations cannot be expected to hold in either of the two situations of Fig. 2, the concept of greater diffusion rate for mass and energy compared to velocity is probably a valid one.

C. GOVERNING EQUATIONS

The equations governing the axisymmetric, compressible mixing of multi-component turbulent fluids have been derived by a number of authors; see e.g., Ref. 13, 5, and 6. In general they are the boundary layer equations obtained by expressing the instantaneous values of dependent variables in terms of mean and fluctuating quantities and then averaging over times long compared to the period of several fluctuations but short compared to periods of macroscopic change. This process results in an excess of terms over and above the laminar equations. These terms may be identified with the turbulent transport of mass, momentum (Reynolds stresses) and energy.

The general species continuity equation, neglecting molecular diffusion, is[13]

$$\bar{\rho} \frac{D\bar{Y}_s}{Dt} = -\nabla \cdot \left(\bar{\rho} \overline{Y_s' \vec{u}'} + \bar{Y}_s \overline{\rho' \vec{u}'} \right) \tag{7}$$

where $\overline{Y}_s$ = average mass fraction of species, s

$Y'_s = Y_s - \overline{Y}_s$, mass fraction fluctuation

$\vec{u}' = \vec{u} - \overline{\vec{u}}$, velocity fluctuation

$\rho' = \rho - \overline{\rho}$, density fluctuation

$D/Dt = \partial/\partial t + \overline{\vec{u}} \cdot \nabla$, the convective derivative

In the boundary layer approximation for axisymmetric flow, this reduces to

$$\overline{\rho}\,\overline{u}\,\frac{\partial \overline{Y}_s}{\partial z} + \overline{\rho}\,\overline{v}\,\frac{\partial \overline{Y}_s}{\partial r} = -\frac{1}{r}\frac{\partial}{\partial r}\left(r\,\overline{\rho}\,\overline{Y'_s v'} + r\,\overline{Y}_s\,\overline{\rho' v'}\right) \tag{8}$$

From the overall continuity equation, it follows also that $\nabla \cdot \overline{\rho' \vec{u}'} = 0$ which in the boundary layer approximation leads to $\overline{\rho' v'}$ = constant with respect to r. Thus

$$\overline{\rho}\,\overline{u}\,\frac{\partial \overline{Y}_s}{\partial z} + \overline{\rho}\,\overline{v}\,\frac{\partial \overline{Y}_s}{\partial r} = -\frac{1}{r}\frac{\partial}{\partial r}\left(r\,\overline{\rho}\,\overline{Y'_s v'}\right) - \overline{\rho' v'}\,\frac{\partial \overline{Y}_s}{\partial r} \tag{9}$$

It has been argued [12] that, near a wall, $\overline{\rho' v'} \to 0$, and therefore must be zero throughout the boundary layer. Such an argument does not apply in free turbulence. The term, $\overline{\rho' v'}$, may be thought of as the correlation, at a point, of the density and velocity fluctuation, a correlation which is non-zero for highly compressible flows. The final term in the above equation may not be neglected; it is the term which accounts for compressibility.

In analogy with laminar diffusion, the turbulent diffusion flux is often replaced by the gradient approximation[14],

$$\bar{\rho}\,\overline{Y_s'v'} = -\,\bar{\rho}\,D_t\,\frac{\partial \bar{Y}_s}{\partial r} \tag{10}$$

where D_t = eddy diffusivity of mass. With this relation, Eq. (10) becomes

$$\bar{\rho}\bar{u}\,\frac{\partial \bar{Y}_s}{\partial z} + \bar{\rho}\bar{v}\,\frac{\partial \bar{Y}_s}{\partial z} = \frac{1}{r}\,\frac{\partial}{\partial r}\left(r\,\bar{\rho}\,D_t\,\frac{\partial \bar{Y}_s}{\partial r}\right) - \overline{\rho'v'}\,\frac{\partial \bar{Y}_s}{\partial r} \tag{11}$$

Specialize to a binary mixing situation. Let $\bar{Y}$ be the mass fraction of a gas centrally injected into an annular, co-flowing stream. The conservation equation for injected mass may be integrated with respect to r with the aid of the overall continuity equation, yielding

$$D_t = \frac{\dfrac{\partial}{\partial z}\displaystyle\int_0^r \bar{\rho}\bar{u}\,\bar{Y}\,r\,dr - \bar{Y}\,\dfrac{\partial}{\partial z}\displaystyle\int_0^r \bar{\rho}\bar{u}\,r\,dr}{r\,\bar{\rho}\,\dfrac{\partial \bar{Y}}{\partial r}} \tag{12}$$

This relation has been used by several authors[5, 6] to infer $D_t(r, z)$ from probe measurements of $\bar{\rho}$, $\bar{u}$, and $\bar{Y}$. Their purpose was to compare the measured D_t with several empirical formulae relating D_t to flow variables. This task is a formidable one. Numerical data must be differentiated, the denominator goes to zero at the centerline and

boundaries, and the difference of two large, nearly equal numbers must be taken. It is not surprising, in view of these considerations, that conflicting results have been obtained for the variation of $D_t(r, z)$.

A similar situation arises in connection with the turbulent momentum equation. Additional stresses due to fluctuations must be added to the stress tensor, τ_{ij}. These stresses, the Reynolds stresses, involve fluctuations of both density and velocity such that the turbulent part (the dominant part) of the stress tensor becomes[12]

$$\tau_{ij} = -\overline{\rho u_i' u_j'} - u_i \overline{\rho' u_j'} - \overline{\rho' u_i'} u_j + O\left(u_j'^3\right) \tag{13}$$

The last term is neglected since it is of higher order in fluctuation. The first term is the only one occuring in constant density flows. A gradient transport description, called the Boussinesq hypothesis, is often used to represent this turbulent momentum flux:

$$\overline{\rho u_i' u_j'} = -\bar{\rho} \epsilon_{ij} \frac{\partial \bar{u}_i}{\partial x_j} \tag{14}$$

The tensor character of the eddy viscosity is undeniable; there are no Reynolds stresses in isotropic turbulence. In spite of this, as pointed out by Harlow and Nakayama[18], in many cases, the macroscopic behavior of nonisotropic turbulence may differ little from that predicted on the basis of isotropy. Thus, e.g., the Reynolds stress appropriate to the boundary layer momentum equation in incompressible flow is written

$$\tau = -\bar{\rho}\overline{u'v'} = \bar{\rho}\epsilon\frac{\partial \bar{u}}{\partial r} \tag{15}$$

and, for compressible flow[12],

$$\tau = -\bar{\rho}\overline{u'v'} - \bar{u}\overline{\rho'v'} \tag{16}$$

In view of this relation, there should be a component of τ which is proportional to $\bar{u}$ in the boundary layer approximation. The ratio of the second to the first term in Eq. (16) has been estimated to increase as the square of Mach number[12]. As the Mach number increases, it is therefore probable that τ can be approximated by a linear function of velocity. The constant of proportionality would still depend on flow geometry.

As in the case of the species continuity equation, the axisymmetric turbulent boundary layer equation in the absence of pressure gradients may be integrated with respect to r and solved for ϵ[6].

$$\epsilon = \frac{\frac{\partial}{\partial z}\int_0^r \bar{\rho}\bar{u}^2\, r\, dr - \bar{u}\frac{\partial}{\partial z}\int_0^r \bar{\rho}\bar{u}\, r\, dr}{\bar{\rho} r \frac{\partial \bar{u}}{\partial r}} \tag{17}$$

Through the application of this equation to experimental data, it is theoretically possible to deduce the spatial variation of ϵ.

An example of the kind of expression used to relate D_t to flow variables is[5]

$$\bar{\rho} D_t = k r_u (\bar{\rho}\bar{u})_{\mathcal{L}} \tag{18}$$

where k is determined from experiment. It has been stated[15] that this is the only existing proposed expression which admits of a z^{-2} centerline decay when used in conjunction with Libby's[16] solution. Whether z^{-2} is the appropriate decay rate is not definitely established by experiment, however.

To see how D_t is related to velocity, the transferrable property, in this case $\bar{Y}_s$, may be treated as is the molecular distribution function of kinetic theory, and, by means of the Krook[17] approximation to the Boltzmann equation and a first order Taylor expansion of $Y_s(t)$, the following expression derived[12]

$$D_t = \int_0^\infty u'(t - t'') \, u'(t) \, e^{-\beta t''} \, dt'' \tag{19}$$

where β is an efficiency of property transfer. Thus it is seen that D_t depends on the autocorrelation of velocity fluctuation and an undetermined material property. This relation also illustrates the dependence of D_t on past history. If $\beta = 0$ (no material dependence), the integral, after inserting a gaussian autocorrelation function, becomes

$$D_t = \overline{u'^2} \, \tau = \overline{u'\ell} \tag{20}$$

where τ is the integral time scale and ℓ is a characteristic length formally identifiable with Prandtl's mixing length. The same analysis applies to other transport coefficients with the only difference being evidenced by the factor, β. Thus, consistent with the mixing length hypothesis, when material factors are ignored, all properties diffuse at the same rate. Relating the turbulent transport coefficients are the dimensionless Schmidt, Prandtl and Lewis numbers:

$$Sc_t = \frac{\epsilon}{D_t} \tag{21}$$

$$Pr_t = \frac{\bar{\rho} C_P \epsilon}{\kappa} \tag{22}$$

$$Le_t = \frac{\bar{\rho} C_P D_t}{\kappa} \tag{23}$$

where C_P is the specific heat at constant pressure.

Kline[4] has pointed out that the eddy viscosity is related to the relative rates of production and dissipation of turbulent kinetic energy and, as such, should be a constant only in flow regions where there is a balance between these two processes. These regions do not include regions of strong turbulence production or developing regions. Assuming ϵ dependent only on axial distance in wake or jet flows has proven to be a useful assumption provided radial correction for the effect of intermittency is made.

Expressions[3, 6] which have been proposed for ϵ in compressible flow involve some characteristic radius and the mean mass flux. The radius enters when one assumes the mixing length proportional to a flow dimension. The mass flux enters when one assumes u' proportional to u. Thus[3]

$$\bar{\rho}\epsilon \sim r_u \left| (\bar{\rho}u)_i - (\bar{\rho}u)_o \right| \tag{24}$$

has been proposed as an extension of Prandtl's eddy viscosity to include compressibility effects. The subscripts i and o refer to the inner and outer jet respectively. Another form which has been suggested[3] involves a compressibility transformation

$$\bar{\rho}^2\epsilon = 2\frac{\bar{\rho}^2_{\mathfrak{L}}}{y2}\epsilon_o \int_o^y \frac{\bar{\rho}}{\bar{\rho}_{\mathfrak{L}}}\, y'dy' \tag{25}$$

where ϵ_o is the constant density eddy viscosity.

Each of the proposed forms requires knowledge of the axial variation of the jet spreading rate, centerline density and velocity and, in some cases, the radial distributions as well. It has been pointed out by Boehman[6] that r_u and $\bar{\rho}u$ may not be specified independently; they are related by the mass and momentum conservation equations. It is the purpose of this experimental investigation to determine the forms which these quantities assume in a compressible mixing situation.

SECTION III

EXPERIMENTAL APPARATUS

A. OBJECTIVES AND APPROACH

The desirability of non-interference diagnostics in flow measurement is well established. Relating measurements to the original phenomena which produce them becomes increasingly difficult if the instrument alters the medium. In supersonic flow, an immersed probe produces a shock wave whose influence is felt over relatively large regions. If chemical composition is the desired measurement, then not only the shock but the probe itself can influence the measurement. And if the medium is at an elevated temperature, the use of immersed probes may not be possible at all. It is desired to make measurements under all of these conditions. The use of optical techniques is therefore a natural approach to be considered.

Spectroscopy offers a way of determining chemical composition. For coaxial mixing flows, the complication introduced by non-homogeniety can be overcome by taking advantage, mathematically, of the cylindrical symmetry. It remains to relate the molecular absorption, emission, or both, to the thermodynamic state of the spectrally active species under scrutiny. In this regard, it is convenient to deal with spectrally simple species. Perhaps the simplest useful species, spectroscopically, is the diatomic vibrator-rotator molecule. The energy

state transitions associated with a diatomic molecule are far better described and understood than those associated with, say, electronic transitions of a monatomic gas.

The desire to employ vibration-rotation spectroscopy implies use of the infrared region of the spectrum. This, in turn, places further restrictions on the choice of molecule to use as a tracer gas. There are atmospheric constituent (e.g.: H_2O, CO_2, CO) absorption bands throughout the IR spectrum and these are to be avoided. Products of combustion may also be considered as noise pertinent to the IR region. It is therefore advisable to choose, as a tracer absorbing (or emitting) molecule, one which has bands in regions unoccupied by these other prevalent species.

Spectral resolution, since it is proportional to wavelength, is such that, in the IR, it may be difficult to resolve an individual spectral line unless the lines of a band are well separated. The moment of inertia of the chosen molecule must therefore be small. A molecule made up of one hydrogen atom and one heavier molecule is indicated. Hydrogen fluoride was the molecule chosen for the present purposes. Its fundamental vibration-rotation band extends into regions devoid of water or CO_2 interference. This is demonstrated by the HF spectrum of Fig. 3 which was taken from the data of Simmons[19] and is characteristic of an extremely high temperature medium. Other reasons for the choice

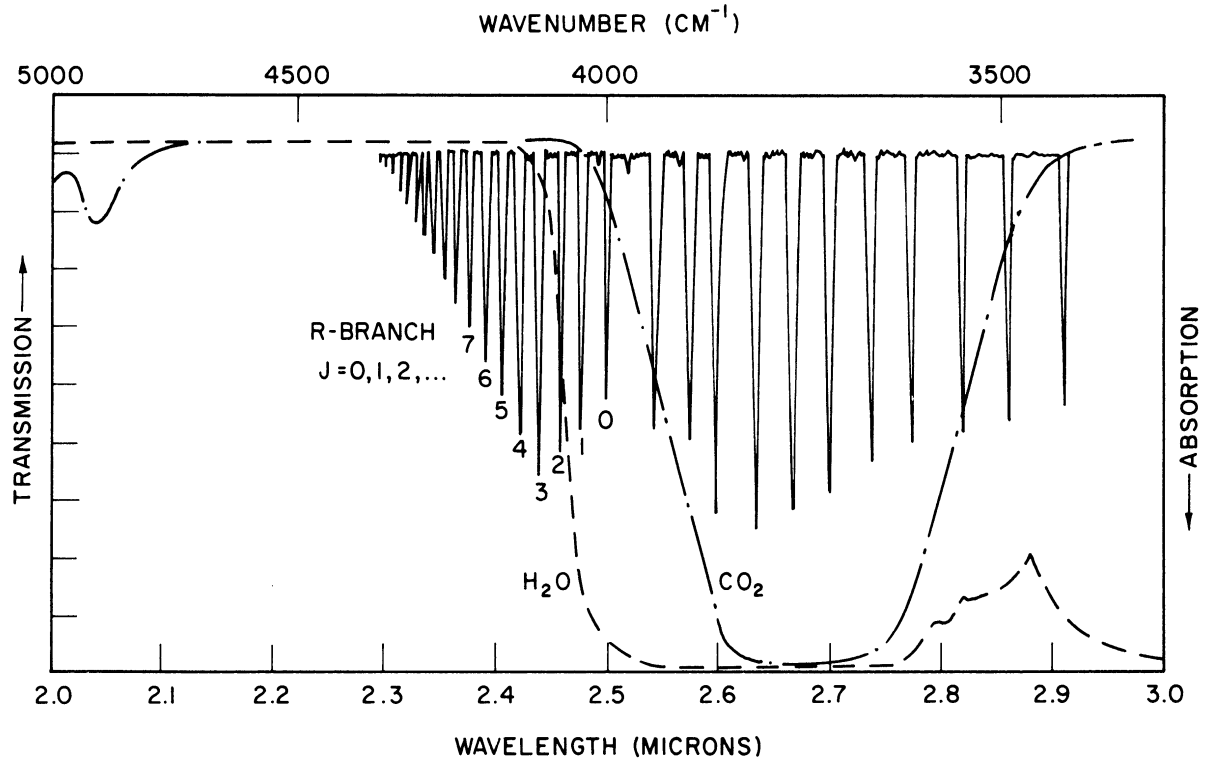

Figure 3. HF Fundamental Vibration-Rotation Absorption Band (R and P Branches). Spectral Location of Water and Carbon Dioxide Absorption Bands Indicated

of HF include: relative chemical inertness in H_2 and air, spectral proximity ($\lambda \sim 2.5\mu$) to the peak detectivity range of the PbS detector and well documented[19,20] spectral properties.

Hydrogen is not the only fuel worthy of consideration for application to the supersonic combustion process. Liquid hydrocarbon fuels are also of definite interest. In the design of the experimental facility it would therefore be expeditious if data on the supersonic mixing of liquid fuel with air were also obtainable. The same apparatus used for molecular absorption measurements can also be used for spectrally resolved transmission measurements made upon a stream of liquid particles. These measurements may be spatially resolved by the same mathematical techniques employed for molecular measurements.

Another experimental design criterion, imposed by the inherently violent nature of combustion processes, is that the diagnostic apparatus be remotely operated. The complexity imposed by this requirement is not insignificant. Motion must be precisely controlled and indicated. Valves must be reliably actuated and perhaps most important, all data must be conveyed over distances conducive to noise pickup. The latter difficulty is largely overcome through the use of synchronous detection.

With the foregoing considerations in mind, the diagnostic system described in this section has evolved. Also described in this section are the experimental conditions under which the system has been operated and the difficulties which arose and were overcome.

B. DESCRIPTION OF THE APPARATUS

The experimental apparatus consists of a coaxial fluid mixing system and an optical diagnostic system. Tracer fluid, either HF or H_2O, is injected centrally into a surrounding air jet while the optical system scans the jet in a transverse direction. The transverse data is then related to the radially symmetric phenomena which produced it.

B. 1. Hydrogen Fluoride Injector

Hydrogen fluoride is shipped as a liquid under its own vapor pressure which is approximately one atmosphere at room temperature In order to pump HF gas, one must either heat the liquid or entrain the vapor in another gas. The former alternative was selected because of a desire for an undiluted injectant. An upper limit is imposed upon the pressure attainable by heating the steel cylinder. A new bottle will become liquid-full at approximately $140^{o}F$ with an attendant large hydrostatic pressure rise. The vapor pressure associated with this temperature is 44 psia. The latent heat of vaporization is such that a mass flow of .003 lb/sec requires a continuous net heat input of 1/2 kw. It is also not recommended that heat be applied directly to the HF bottle. For this reason, a brass recirculating water jacket was constructed to envelop the bottle. Heating tapes (1.5 kw max) were wrapped around the brass cylinder and fiberglass insulation enclosed the wrappings. Bottle size No. 3 (9 lb net) was chosen such that a continuous flow rate

of .003 lb/sec would allow run times of 1 hr. The actual delivered dimensions of this size cylinder varied by as much as 5 in. lengthwise and necessitated the incorporation of adjustable legs on the water jacket.

Immersed in the water jacket are a temperature-controller feedback thermistor and a chromel-alumel thermocouple. During high-flow operation it was necessary to manually override the temperature controller due to the thermal gradient between the thermistor position and the inner wall of the HF cylinder. This posed no great problem once familiarity was gained with the systems flow characteristics. Care had to be taken in order to insure thermal compatibility between the glass-enveloped thermistor and the water prior to immersion. Thermistor breakage occurred otherwise. Due to the aforementioned thermal gradient, the bath's thermocouple output bore no particular relevance during a run. Its output was recorded, however, and provided pertinent pre-run information.

For safety, the HF heating position is located in a specially constructed shed adjacent to the test cell. The shed is insulated, heated, and ventilated. It also serves as a store for unused HF bottles. A steel bulkhead separates the heating area from the test area.

The corrosiveness of HF causes its bottle valve to stick. The torque required to initiate valve opening exceeds 30 ft-lb on occasion. Motor operated valve operation therefore becomes an unjustifiably

expensive operation. For this reason, a right-angle drive and an exterior valve stem were incorporated. With this arrangement, an operator can open an on-line pressurized bottle from the outside of the shed. An intercom was installed to provide communication with the main control room on the far side of the test cell.

A special monel adapter section joins the HF line to a dry nitrogen purge line immediately downstream of the bottle valve. Purging is initiated via a pitot-operated solenoid valve whose stainless steel plunger was replaced by one of pure nickle. Corrosion of the stainless steel plunger's tip necessitated its replacement. The valve body is brass and the valve seat is Teflon. In the absence of oxygen, brass is an acceptable material for use in contact with HF. The zinc in the alloy is leached out of a thin surface layer leaving pure copper which resists further deterioration. Teflon and other fluorocarbon polymers, such as Kel-F, are not attacked by HF. Saran is also good and was employed to cover otherwise exposed apparatus in the test cell itself.

Beyond the purging junction, as shown in Fig. 4, a monel needle valve regulates the flow. The needle valve was fitted with a slip-clutch and a reversible motor for remote regulation. Due to the exhorbitant pressure drop associated with this valve, it was removed from the system for high flow operation. Regulation is then effected through control of the heat input to the HF bath. Beyond this point, the HF line lies within the test cell.

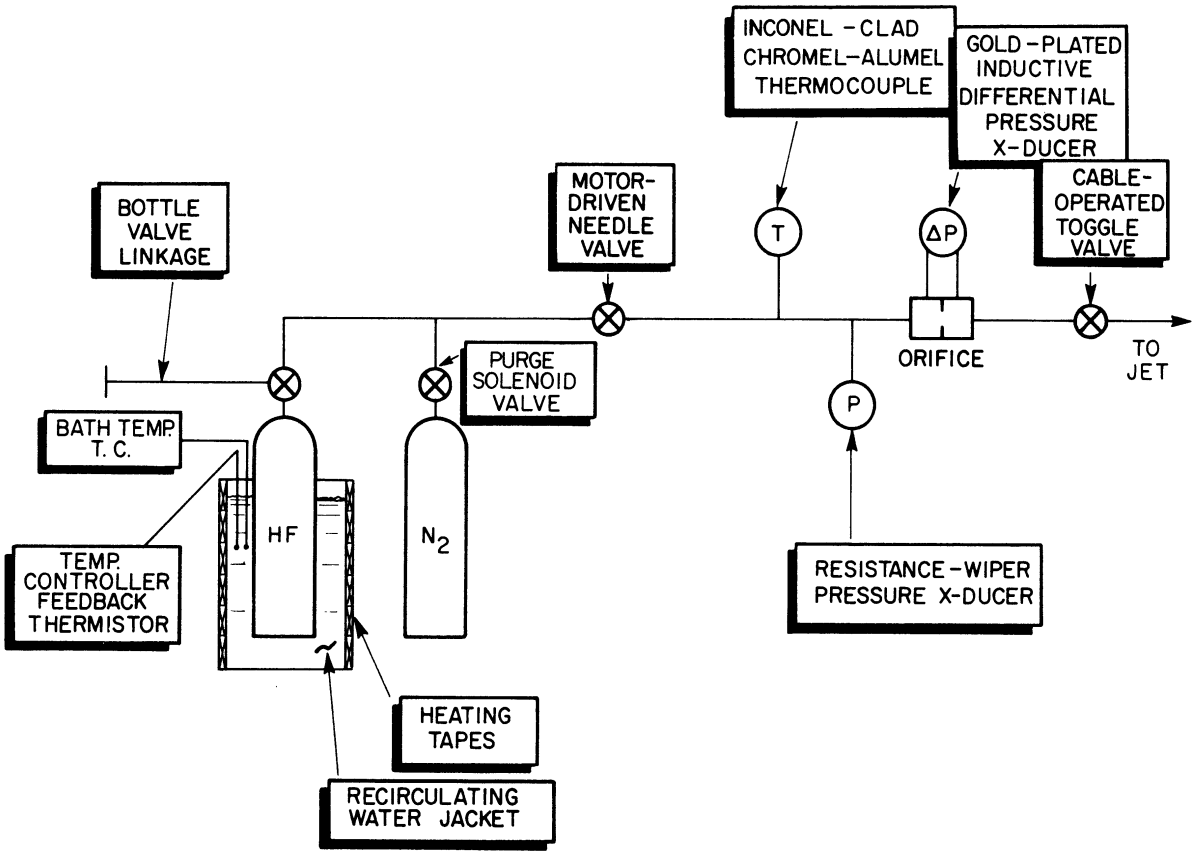

Figure 4. Hydrogen Fluoride Injection System

The HF line itself is primarily 1/4 in. monel pipe furnished by the International Nickel Corporation whose generosity is gratefully acknowledged. Pipe this large was specified in an effort to minimize friction losses, an acute requirement in view of the small driving pressure available. All fittings were silver soldered.

An inconel-clad chromel-alumel thermocouple monitors the HF temperature. Although darkened by HF contact, the thermocouple sheath has not required replacement.

The measurement of pressure in a corrosive environment poses a more difficult problem. Transducers rated for duty in HF are prohibitively expensive, special-order items. Both a differential and a static pressure measurement is required in order to obtain the HF mass flow rate. In view of the cost of two such transducers, an attempt was made to use transducers of non-resistant materials buffered by an appropriate inert liquid. Use of a capacitive differential pressure transducer would require such a buffer in any event due to the high dielectric constant of HF.

No such fluid could be found. The most promising candidate, Dupont Krytox 144A fluorocarbon oil, disappeared spectacularly from all reservoirs leaving a black residue. At the same time, a powdery white film was deposited on surfaces near the injector exit.

This measurement problem was solved by the following expedient. The static pressure is measured by a resistance-wiper transducer

treated as a disposable item. Its stainless steel diaphragm, coated with the oily residue mentioned above, has survived surprisingly well to this date. Its calibration has, in fact, not been significantly altered by over six hours of HF contact. The differential pressure measurement is effected by a surplus inductive transducer whose interior has been gold plated. The orifice across which this pressure is measured was specially designed and constructed of monel with Teflon "O"-rings. It's calibration is described in Appendix A wherein an indirect measurement of the vi scosity of gaseous HF is also reported.

The final valve in the HF injection system is a toggle-operated monel valve. Since this valve must be the most reliable, it is manually operated by a cable-pulley system extending through the control room's wall. Through its use, HF injection can be terminated even if there should be a power failure.

Downstream of this valve, a flexible hose section is inserted to allow nozzle travel. The hose is 1/4 in. I.D. Teflon covered with Neoprene. The final short segment of the system is 1/8 in. I.D. -3/16 in. O.D. stainless steel tubing treated as an expendable item. This section extends to the exit plane of the annular air nozzle.

B.2. Mixing Nozzles

Two nozzles, shown in Fig. 5, were employed; one for supersonic operation, the other subsonic. High pressure air (2200 psi max) is

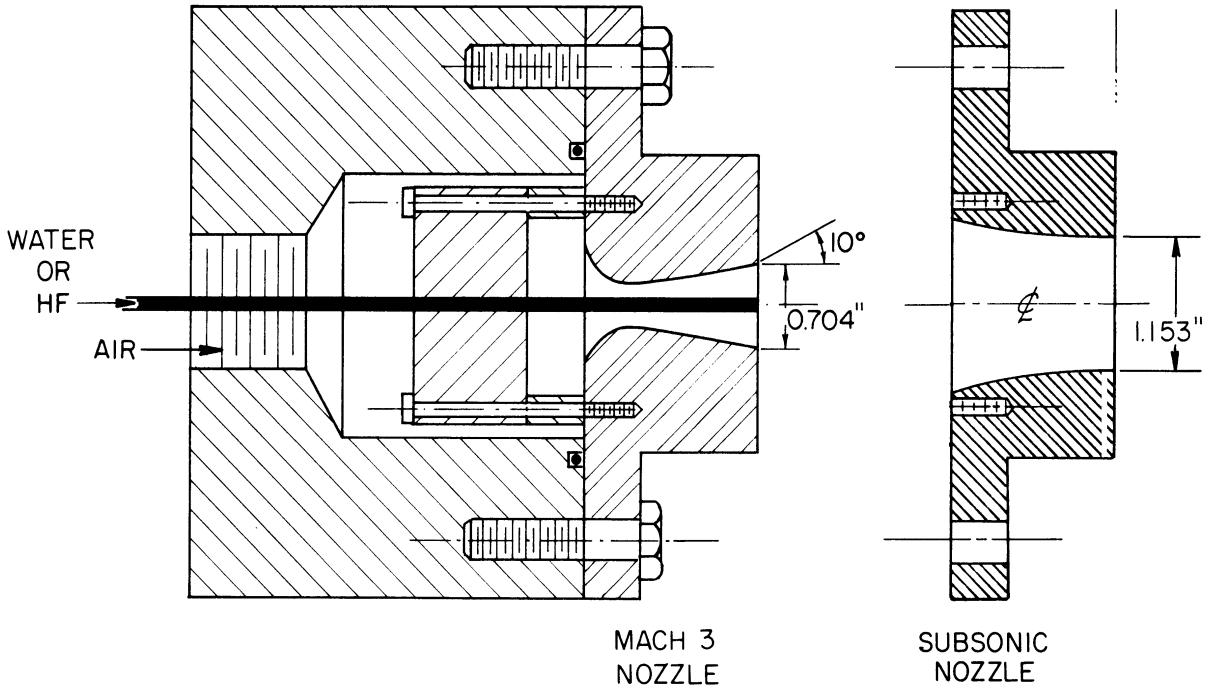

Figure 5. Coaxial Mixing Nozzles

supplied by mechanical pumps after being filtered and dried. Continuous operation at flow rates of 1/2 lb/sec are achievable. Supersonic runs at 1.1 lb/sec could be maintained for approximately one-half hour. Stagnation temperature and pressure are displayed on gages in the control room. Mass flow is monitored by an orifice meter with a square root dial. Nozzle chamber pressure is measured by a resistance-wiper type pressure transducer and displayed on a strip-chart recorder. Regulation is achieved by a dome-loader regulator or a pneumatically operated throttling valve depending on the flow rate required. In addition, the subsonic nozzle has an exit pressure tap which was used to calibrate the flow measuring orifice. A section of high pressure flexible hose connects the nozzles to the air supply.

The supersonic mixing nozzle is constructed of brass. It is designed for perfect expansion to atmospheric pressure at an exit Mach number of three. This implies a chamber pressure of 540 psia. Shadowgraphs exhibit a weak shock-diamond structure in the flow due to the finite expansion angle of the conical nozzle. This structure is apparent as far as 8 nozzle diameters (6 in.) downstream of the exit plane. It is largly obliterated during central injection as noted from shadowgraphs taken during CO_2 injection.

Further evidence of the weakness of these shocks is obtained from static and stagnation pressure probe data. The air jet was mapped by

this means both in the radial direction and to axial distances exceeding 40 nozzle radii. From these data the profiles of static temperature and pressure, density and velocity were determined. Integration of these profiles provided information on the mass entrainment rate and the total jet momentum as a function of downstream distance. The mass flow rate at the nozzle exit corresponded to that measured by the flow meter and served as an independent calibration. The momentum flux, as measured, remained constant with respect of downstream distance as, of course it should. Its magnitude, 67.5 lb, compares favorably with the nozzle thrust computed from the rocket thrust equation. These measurements were effected with immersed probes supported by a gantry attached to the movable optical platform described later in this section. The usual operating parameters of each nozzle are compiled below.

	Supersonic Nozzle	Subsonic Nozzle
Exit Diameter	1.786 cm	2.93 cm
Net Exit Area	2.33 cm^2	6.44 cm^2
Exit Mach Number	3.0	0.33
Exit Velocity	6×10^4 cm/sec	1.1×10^4 cm/sec
Stagnation Temperature	300^oK	300^oK
Exit Density	3.6×10^{-3} gm/cm^3	1.28×10^{-3} gm/cm^3
Mass Flow Rate	500 gm/sec	92 gm/sec
Thrust	67.5 lb	2.28 lb
Reynolds Number	2.38×10^6	2.2×10^5

These nozzles exhaust vertically into a hooded exhaust system. For operation with HF, a water ejector, located on the roof of the test cell, dilutes the effluent in order to render it disposable through conventional drains.

B. 3. Spectrometer Installation

In view of the intended application of the spectrometer system to arc jet diagnostics as well as to cold jets, it has been designed to perform the spatial scan itself rather than require that the nozzles be movable. This is accomplished by mounting the entire optical system: source, chopper, and monochromator, on a movable platform as shown in Fig. 6. Motion is controlled by means of a servo motor mounted on the underside of the optical platform. The platform itself is of an asbestos-cement composition chosen for its vibrational and dimensional stability and because it is non-magnetic. The latter requirement arises due to the strong field employed around the arc jet[21]. Shock-mounted ball bushings riding on parallel ways provide support for the 4 ft x 4 ft platform. All optical apparatus is also shock mounted.

The coaxial mixing jets issue vertically through a 16 in. hole in the optical platform. Axial scanning of the jet is accomplished manually, between runs, by positioning the jet on two vertical ways. Transverse position is sensed by a biased linear potentiometer attached to the platform. Its output is used to drive the abscissa of an x-y recorder.

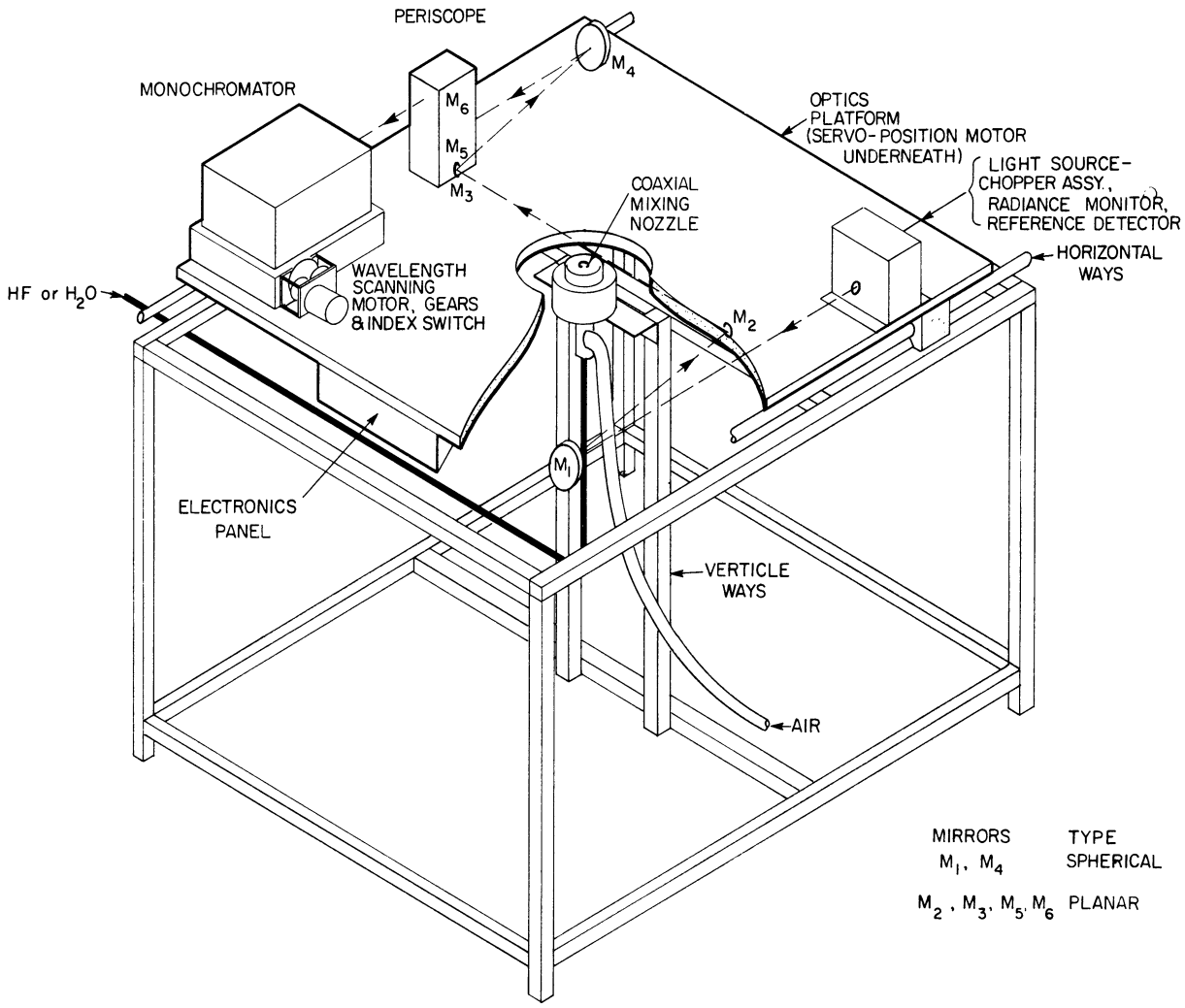

Figure 6. Jet Mixing Test Stand

The bridge-balance servo positioning system was calibrated using a dial micrometer to measure platform position as a function of abscissa on the x-y recorder and potentiometer setting on the control panel. Positional repeatability to within 0.2 mm was achieved for unidirectional approach while a 0.8 mm hysteresis was noted for opposite approaches. Total platform travel is 7.35 cm or 23 injector radii limited by the stroke of the servo positioner feedback potentiometer. Platform velocity is constant over 95% of the total range. This feature allowed x-t recordings to be compared with x-y recordings whenever an experimental ambiguity arose.

A schematic diagram of the optics and associated electronics is shown in Fig. 7. Components on the movable platform are enclosed by the dashed line. All other components are located within the control room and connected by low inductance, foil—shielded electrical cable layed in steel conduits.

A chopper-modulated light source is brought to a focus at the central plane of the jets and, continuing, again at the entrance slit of a scanning monochromator. The f/12 optical system is entirely reflective and arranged anti-symmetrically to minimize spherical abberations. All components on the platform are enclosed in two sheet aluminum housings flushed with dry nitrogen. The housings are sprayed with optically flat black paint and lined with flocked optical paper.

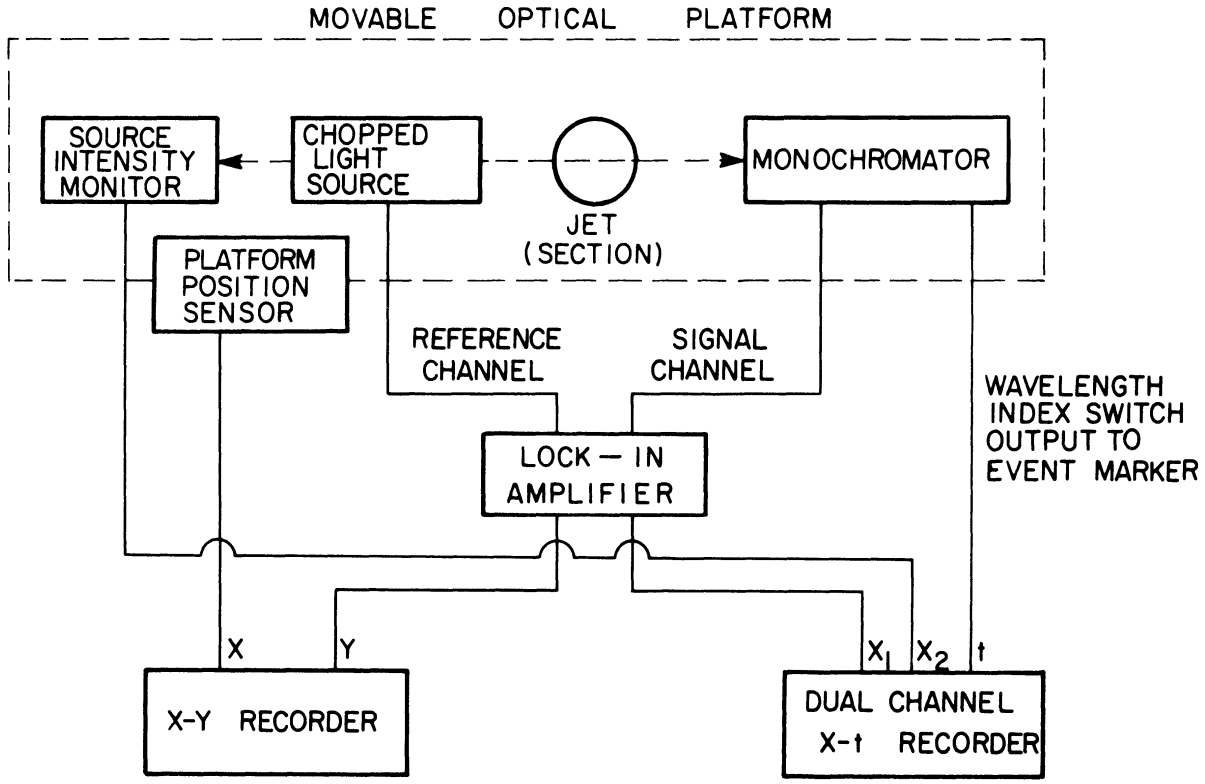

Figure 7. Block Diagram of Optical Instrumentation

The stability of the light source is monitored by a phototube whose output is displayed on a dual-channel x-t strip chart recorder. This was done to insure that changes in the monochromator output, displayed on the same chart, would not be interpreted as data. In the early development stages, before the source power supply (see below) was perfected, this was not an uncommon occurrence. A source drift compensation network was developed[22] to correct this behavior but was not needed for the later runs.

The monochromator output is also displayed as the ordinate of an x-y recorder whose abscissa is the platform position. Serving as the main signal processing unit is a PAR Model 120 lock-in amplifier tuned to the chopping frequency. Individual components of this data gathering system are described in greater detail in the ensuing subsections. The use and capability of the system as a whole is outlined in the final subsection.

B.4. Source and Power Supply

The IR source itself is a tungsten horizontal filament lamp (GE 18A/T10/2P-6V, SR-6A filament) mounted on its side such that the filament is vertical. In this way, the height of the optical path above the platform is minimized (2.5 in.). This particular lamp has unusually uniform radiance over the bottom leg of its "U" shape[23]. There is a convective instability associated with this lamp when

operated in the normal upright mode. It manifests itself as a slow (.5 Hz) output intensity ripple arising due to the off axis position of the filament. This was observed in this laboratory and was also mentioned in Ref. 23. No such instability occurs when it is mounted on its side.

The nominal filament current in the present experiment is 9 amp. Power is provided by the filament power supply shown in the schematic of Fig. 8. It operates on the principle of continuous charge and discharge of an automotive storage battery, the battery serving as an electrical surge tank. Provided all electrical contact points (e.g.: autotransformer and rheostat wiper arms) are kept clean, this power supply is entirely adequate for operation in excess of four hours. A one-hour warm up period is usually advisable.

The filament is housed as an integral unit along with the chopper and reference detector. An exploded view is shown in Fig. 9. A synchronous motor and drive belt run a two bladed chopper at a nominal frequency of 100 Hz chosen to lie in a relatively quiet region of the anticipated noise spectrum. Chopper radiance from one side of the filament is focussed by a diagonal mirror and Fresnel condensing lens on an LS-400 photoswitch (Texas Instruments) providing the stimulus for the reference channel of the lock-in amplifier. The spectral radiance emitted by this unit is detected by the lead sulphide cell of the monochromator described below.

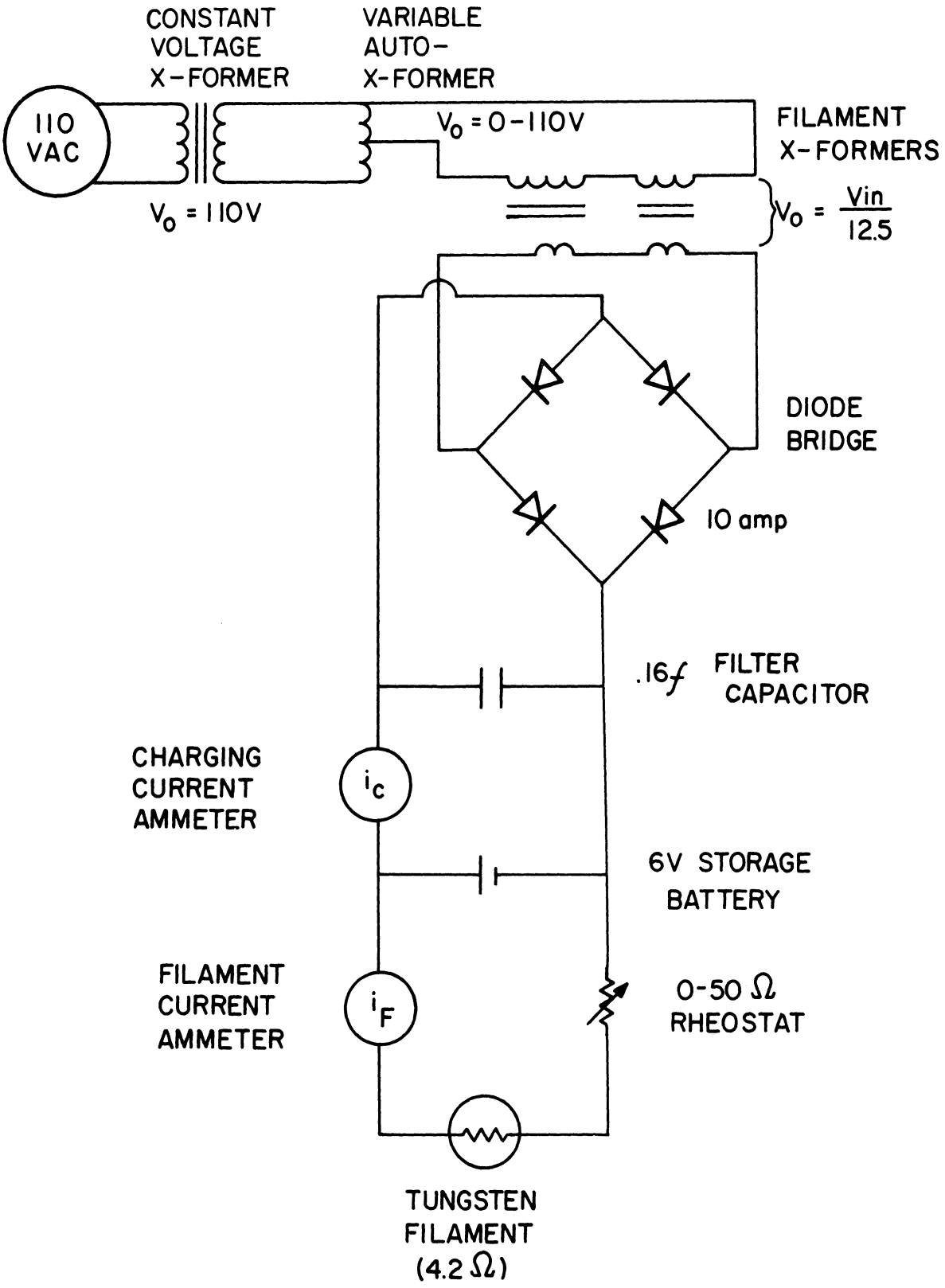

Figure 8. Light Source Power Supply

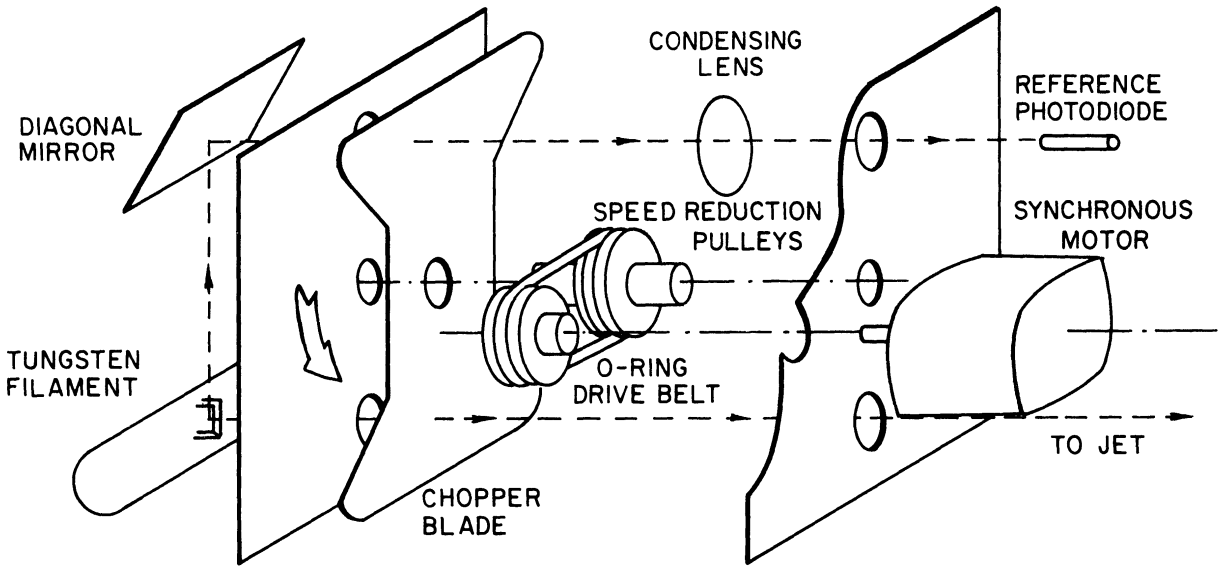

Figure 9. Source, Chopper, and Reference Detector

B. 5. Monochromator

The monochromator (Fig. 10) is a Perkin Elmer Model 98G fitted with a grating blazed at $\lambda = 2.5\mu$. Three spacers, when inserted individually in the grating mount, provide a total spectral scan range of more than 3μ centered at 2.5μ. The medium-sized spacer, used for the HF absorption runs, allowed continuous scanning from 1.6 to 2.75μ. A long wave pass filter screens out unwanted higher order diffraction beyond 1.6μ. The filter is mounted in front of the monochromator's entrance slit and is constructed of germanium evaporated on a sapphire substrate[22]. The entrance slit, when imaged backward on the jet central plane defines a spatial scanning resolution of 1.2 cm in the axial direction and of the order of the slit width in the radial direction. For the HF runs, a slit width of 70μ was employed. For the scattering runs, slit widths of 100μ and 150μ were employed at 2.38μ and 1.6μ respectively.

Spectral scanning is accomplished by rotating the grating. A synchronous motor (Insco Model 06700, 10 rpm, 41 in.-oz) with reduction gearing affords grating drive. Spectral location is indicated by a printed circuit spoked wheel affixed to the grating drive shaft. Wipers act as switch contacts which are "on" four times per revolution. This switch is connected to a marginal event marker on the x-t recorder and provides a chart marking which is $.00605\mu$ long independent of the gear

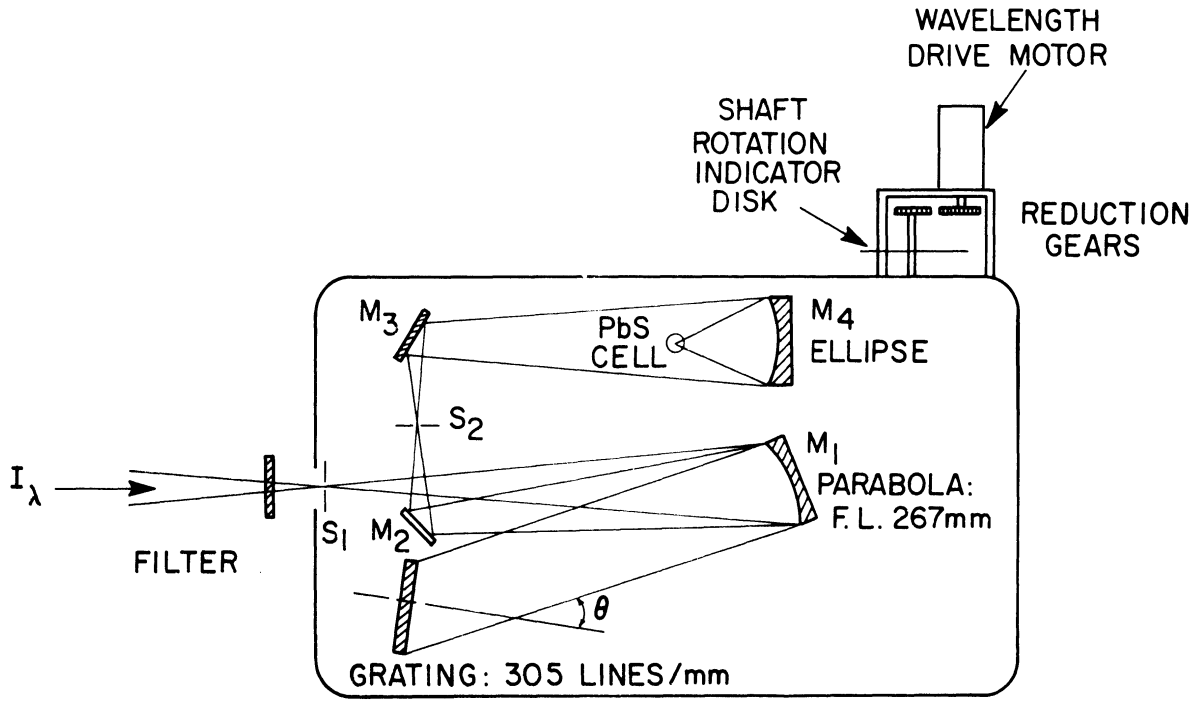

Figure 10. Perkin-Elmer Model 98-G Monochromator

ratio setting or chart speed. Adjustable limit switches, affixed to the wavelength drive mechanism, restrict the scanning range.

The calibration and capabilities of the monochromator/optics combination are reviewed in Appendix C.

B. 6. Detection Circuitry

Spectral radiance which has been dispersed by the grating is detected by a Kodak Ektron Type N photoconductive cell after undergoing six-power demagnification. The cell is biased as shown in Fig. 11. The output voltage is taken across a low-noise evaporated film load resistor and fed into the signal channel of the lock-in amplifier. A gold plated microphone connector and a doubly shielded cable layed in grounded copper tubing conducts the PbS output to the bias circuitry attached to the platform electronics panel shown in Fig. 6. The output of the reference photodetector is similarly conducted to the reference channel input.

Referring to Fig. 11, the operation of the lock-in amplifier is as follows. Both the reference signal and the PbS signal are preamplified in a tuned AC amplifier stage with a resonant Q = 10. It is the amplitude of the 100 Hz square wave which conveys the necessary information. The signal emerging from this stage therefore contains the data and whatever noise is contained in a 10 Hz bandwidth centered on 100 Hz.

The two channels are then mixed in a phase sensitive demodulator section. The effect of this section is to lock the two channels into phase

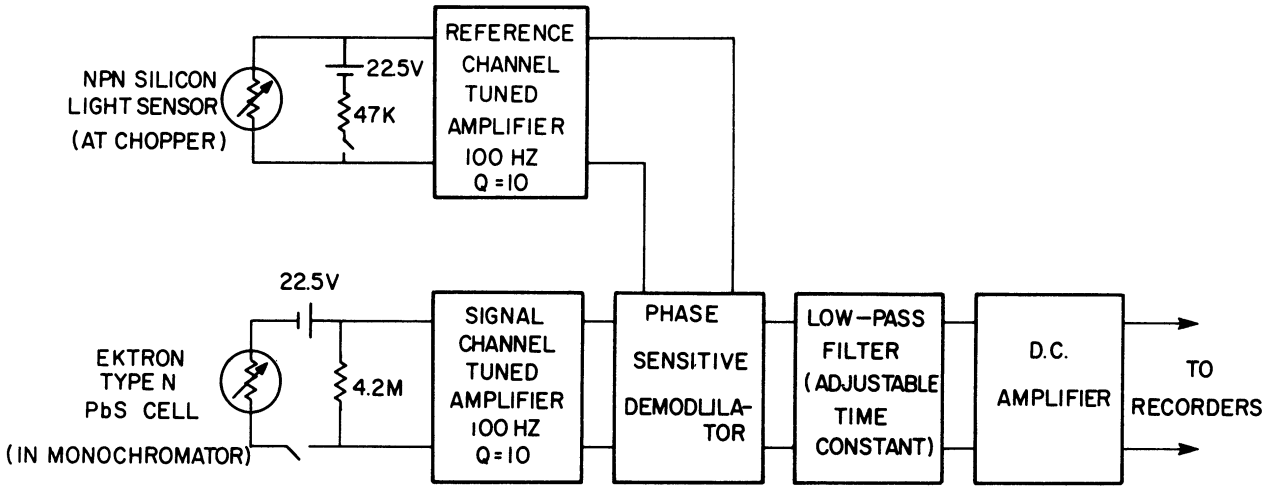

Figure 11. Block Diagram PAR Model 120 Lock-in Amplifier

synchronization and then to multiply the two voltages. Appearing at this stage's output is rectified (positive) 200 Hz coherent data and random (positive and negative) noise. A subsequent low frequency pass filter stage has the effect of averaging the two signals with the result that the random noise averages to zero. This stage has an adjustable integration (averaging) time constant, τ, which in practice was set at 0.3 sec. With the final filter stage removed from the circuit ($\tau = 0$), the output at this point exhibited some residual noise which passed through the 10 Hz preamplifier bandwidth as might be expected from lengthy, high impedance, cable operating in the presence of electrical machinery. The effective bandwidth for $\tau = 0.3$ sec is 0.05 Hz which was more than adequate to clear the signal for the final stage DC amplification.

C. EXPERIMENTAL PROCEDURE

The output of the lock-in amplifier is displayed both on an x-y and x-t recorder. In this way, both operational modes are recorded. The two modes are: spectral scanning while at one spatial location and spatial scanning while at one wavelength such as the center wavelength of a spectral line. During light scattering data runs, the latter mode was the only mode employed. This mode also provides better relative spatial resolution than does the stop-start method of the first mode. In practice, the platform position control was simply dialed to the

opposite extreme range setting and the table allowed to move continuously, thereby tracing an absorptance profile on the x-y recorder. One full range spatial scan takes slightly less than two minutes to complete.

Before each run, a zero transmission tare reading was obtained by physically blocking the light path. Full-range spectral scans were made before and after each run. All instruments were zeroed while all electrical circuits were in operation. The sequence of operations is outlined below.

Prior to each run, all measurement systems and the IR source were allowed to warm up for at least one hour. The HF injection system is purged with dry nitrogen. During this period, the HF heater bath is filled and heating is initiated. Bath temperature is monitored. When the bath temperature has stabilized at a predetermined value, air flow in the coaxial nozzle is initiated. No valves in the HF injection line are ever opened unless there is air ejector action maintained at the injector exit. Beakers of ammonia are set at strategic locations in the test cell to serve as HF leak detectors.

Hydrogen fluoride injection is begun by opening the HF cylinder's valve and charging the system as far as the final toggle valve. At this point, the HF pressure reading is compared to that expected from the bottle temperature. The final valve is opened manually.

Before optical measurements are taken, the HF line pressure and orifice differential pressure are allowed to stabilize. This is accomplished by adjusting the heat input. The mass of HF used during a run is compared to the integrated mass flow rate obtained from the orifice meter readings.

HF shutoff is begun by closing the bottle valve and purging again with nitrogen. The air flow is maintained throughout this operation. The toggle valve is closed, leaving a charge of nitrogen in the lines, and the air is shut off. After the run, the pressure transducers are inspected for damage and their calibration checked.

Water injection is effected by utilizing the natural siphoning action of the supersonic nozzle. The vacuum created, by the supersonic flow, in the deadwater region of the injector exit is shown in Fig. 12. The injector exit pressure was obtained by connecting a vacuum gage to the upstream side of the injector tube and varying the air stagnation pressure (mass flow). The air exit pressure was computed from the isentropic nozzle equations. As the air mass flow is decreased from its design value, the oblique exit shock pattern approachs the exit plane until an oscillating supersonic-subsonic region envelopes the injector exit. Lower mass flows (stagnation pressures) are insufficient to maintain supersonic flow at the exit with the result that injector suction is greatly reduced. All water injection was performed at air nozzle

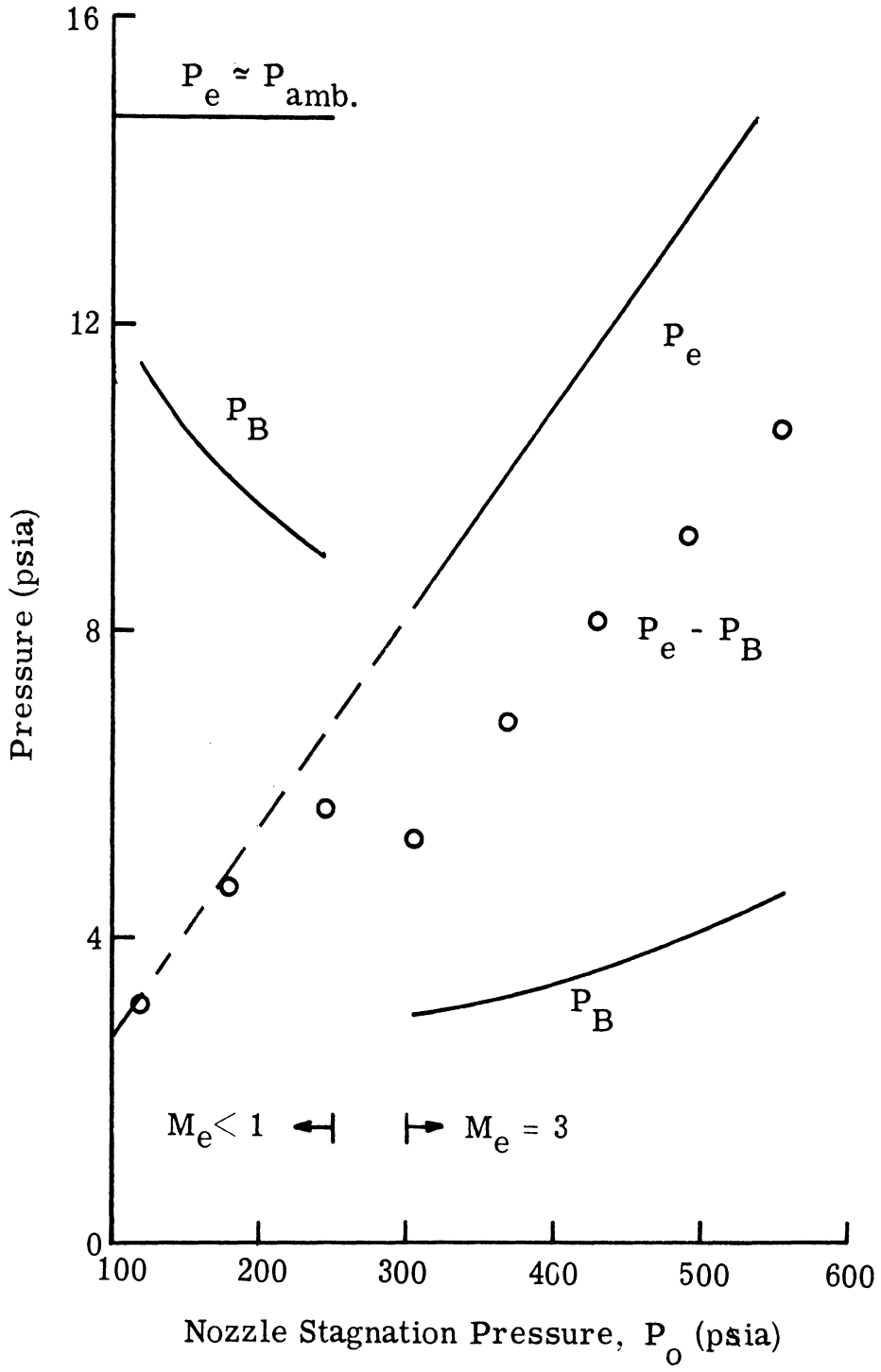

Figure 12. Exit Pressure and Base Pressure (Deadwater) Variation During Overexpanded Operation of 10^o Half-Angle Conical Mach 3 Air Jet (No Central Injection)

design conditions. The water flow rate was obtained by weighing the water reservoir before and after each run. Constancy of injection rate was established by monitoring centerline light path attenuation for long periods. Various injection rates were obtained by adjusting a needle valve in the injector tubing.

SECTION IV

LIGHT SCATTERING

A. INTRODUCTION

Interest in light scattering first centered around transmission through fog in the atmosphere. In this respect, scattering was an undesirable phenomenon which was sought to be minimized[24-27]. Yellow fog lights were one result of this research. As a diagnostic tool, however, light scattering has enjoyed increasing application. It is particularly suited to measurement in hostile environments, such as rocket motors[28, 29, 30], where some knowledge of particle size is desired. In solid propellant rockets, for example, metal particles are added to the propellant to improve specific impulse by effectively raising the chamber temperature. The resulting I_{sp} is slightly reduced due to particle-lag losses however. Computation of these losses requires knowledge of the particles' characteristics. Combustion efficiency in liquid propellant rockets is also heavily dependent on droplet size distributions. The application of scattering techniques to the measurement of super sonic mixing of liquid fuel and air is a natural one. As will be shown in this section, a number of factors combine to render this task less ambiguous in high-speed mixing than it would be at lower mixing velocities.

The experimental apparatus (SectionIII), designed primarily for spatial and spectral mapping of absorbing gases, is also ideally suited to scattering measurements of two-phase fluid mixing. No modification in the measurement system is required and only minor modifications are necessary in the fluid injection system. The decision to measure scattering was made, initially, only to assess its influence on absorption measurements (Section V). Data resulting from these tests, however, were sufficiently interesting to warrant a more complete study.

The measurement involves recording the transmission loss suffered by a beam of light as it traverses a cylindrical stream of water droplets. This is tantamount to a measurement of the total energy scattered into all solid angles (except the forward direction). By means of a numerical Abel inversion transform, the transverse profile of this measurement may be transformed into a radial profile of the scattering extinction coefficient, K_λ. In this way, a path-integrated measurement becomes a point measurement.

In order to relate K_λ to the physical variables upon which it depends, three independent measurements are needed: the total water mass flow rate, and $K_\lambda(r)$ measured at two separate wavelengths. The three variables measured by this technique are: droplet number density, $N(r,z)$, mean droplet diameter, $\overline{D}(z)$; and a measure of the particle velocity, $\langle u(z) \rangle$. From $N(r,z)$, the rate of spreading, $r_1(z)$, of the fuel jet can also be determined.

It will also be shown that all centerline values of these variables may be obtained without resorting to an Abel transformation. Advantage is taken of integral properties of the transformation to accomplish this. There is also a region of the jet in which the radial variation of $N(r, z)$ was found to be closely gaussian. The resulting simplification in the mathematical formulation facilitates study of the effects of fuel/air ratio variation.

In this section, the equations necessary to describe the scattering of light by particles in two-phase fluid flow are formulated. The methods of data interpretation are then developed. Data is then presented showing the axial variation of $N(r, z)$, $\bar{D}(z)$, $r_1(z)$, and $\langle u(z) \rangle$ at one fuel/air ratio in Mach 3 mixing. Finally, data is presented for one axial position with various fuel/air ratios.

B. MATHEMATICAL FORMULATION

Consider the optical geometry of Fig. 13 wherein light is incident upon a cylindrically symmetric jet of particles. The light beam lies in a plane perpendicular to the jet's axis of symmetry and that portion within the jet describes the chord of a circle. The length of the optical path within the jet is L a function of the transverse coordinate, y. It is customary to define the sense of the path variable, ℓ, such that $\ell = 0$ on the boundary nearest the observer and increases positively into the scattering medium. Thus light enters the jet at $\ell = L$ and emerges at

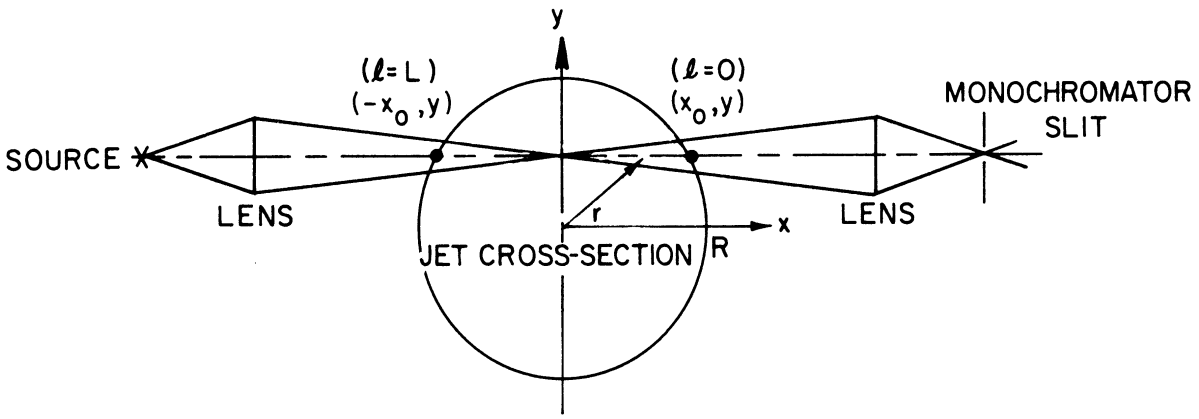

Figure 13. Coordinate System of Scattering or Absorption Experiment

$\ell = 0$. The differential attenuation suffered by the beam while traversing a length, $d\ell$, is given by

$$\frac{dI_\lambda}{d\ell} = K_\lambda I_\lambda \tag{26}$$

where

I_λ = spectral radiance
K_λ = scattering extinction coefficient

The extinction coefficient is proportional to the number of particles and their cross-section within the scattering volume. The efficiency with which a single particle scatters radiation is described by the scattering area coefficient, K_s. Thus K_λ, for a monodisperse medium, is written[31]

$$K_\lambda = K_s \frac{\pi}{4} D^2 N \tag{27}$$

where N is the particle number density and D is the particle diameter. In a polydisperse medium, this generalizes to

$$K_\lambda = \frac{\pi}{4} N \int_0^\infty K_s \left(\frac{\pi D}{\lambda}\right) \phi(D) D^2 \, dD \tag{28}$$

where $\phi(D)$ is the normalized particle size distribution function and λ is the light wavelength. Expressions for K_s and $\phi(D)$ are discussed in Appendix B. In what follows, it is convenient to express K_λ in terms

of the scattering parameter, $\alpha = \pi D/\lambda$, such that

$$K_\lambda(r,z) = \frac{\lambda^2}{4\pi} N(r,z) \int_0^\infty K_s(\alpha)\phi(\alpha)\alpha^2 d\alpha \tag{29}$$

Here, α itself can also be a function of the radial and axial coordinates, r and z. As defined in the appendix, this equation may be recast in terms of a particle average denoted by a single bar or by an area-average denoted by a double bar:

$$K_\lambda = \frac{\lambda^2}{4\pi} N \overline{K_s \alpha^2} \tag{30}$$

$$K_\lambda = \frac{\lambda^2}{4\pi} N \overline{\overline{K_s}\,\overline{\alpha^2}} \tag{31}$$

An observer measuring $I_\lambda(y,z)$ emerging from the near jet boundary sees only the cumulative effect of the non-homogeneous scattering between $\ell = 0$ and $\ell = L$. If the incident radiation is denoted by I_λ^o, then the fraction transmitted is given by

$$-\ln \frac{I_\lambda(y,z)}{I_\lambda^o} = \int_0^L K_\lambda(r,z)\, d\ell \tag{32}$$

Defining the absorptance, a_λ, as the fraction of incident spectral radiance lost by scattering, we have

$$-\ln[\,1 - a_\lambda(y,z)\,] = \int_0^L K_\lambda(r,z)\,d\ell \tag{33}$$

Expressing $d\ell$ in terms of cylindrical coordinates, this becomes,

$$-\ln[\,1 - a_\lambda(y,z)\,] = 2\int_y^{R(z)} K_\lambda(r,z)\,\frac{r\,dr}{(r^2 - y^2)^{1/2}} \tag{34}$$

where R is the jet radius. This is an Abel integral equation (32) the formal inverse of which is

$$K_\lambda(r,z) = \frac{1}{\pi}\int_r^{R(z)} \frac{d}{dy}\,\ln[\,1 - a_\lambda(y,z)\,]\,\frac{dy}{(y^2 - r^2)^{1/2}} \tag{35}$$

Thus the assumption of cylindrical symmetry allows a path-integrated measurement to be transformed into a point measurement. If a Cartesian mapping of data, $a_\lambda(y,z)$, is obtained, then this may be related to the polar mapping, $K_\lambda(r,z)$. Since a_λ is obtained in discreet form, the above integral is replaced by a summation in actual practice. A suitable shift of summation index avoids the difficulty of differentiating experimentally obtained data. The Abel inversion technique actually employed in the present investigation is discussed in Section IV-C.

A measurement of $K_\lambda(r,z)$ at a known wavelength leaves two unknowns in Eq. (29) : $\phi[\,\alpha(r,z)\,]$ and $N(r,z)$. The number of independent

data required for complete solution is effectively greater than two, however, because more than one parameter is required to specify $\phi(\alpha)$ in any real situation. A simple example of a two parameter distribution is the gaussian distribution specified by a mean α and a width. A monomodal distribution consisting of a single delta function can, of course, be described by a single parameter, its location in particle size space. The situation is further complicated, however, by the nature of K_s (see Fig. 23). In any experiment, a value of K_s which has at least two corresponding α's is obtained. In order to remove this degeneracy, additional information is required. The method devised to unambiguously measure K_s relies on a fluid mechanical measurement, the water mass flow rate. In the process, an additional unknown, the particle velocity, is introduced. A combination of measurements taken at two separate wavelengths and a measurement of the mass flow rate provide sufficient information for complete solution. The process is described below.

In axisymmetric flow, the water mass flow rate is given by

$$\dot{m}_w = 2\pi \int_0^R \rho u r \, dr \tag{36}$$

where ρ = water particle mass density and u = particle velocity. The water particle number flow rate is given by

$$\dot{N} = 2\pi \int_0^R N u r \, dr \tag{37}$$

Relating these two expressions is the mass density

$$\rho = \frac{\pi}{6} \rho_w N \int_0^\infty \phi(D) D^3 \, dD \tag{38}$$

where ρ_w is the particle material density.

From Eq. B-8 and B-10, this may also be written

$$\rho = \rho_w \frac{\lambda^3}{6\pi^2} N \overline{\alpha^3} \tag{39}$$

Thus the mass flow rate becomes

$$\dot{m}_w = \frac{\lambda^3}{3\pi} \rho_w \int_0^R \overline{\alpha^3} N u r \, dr \tag{40}$$

We now define a particle volume flux average velocity such that

$$\dot{m}_w = \frac{\lambda^3}{3\pi} \rho_w \langle u \rangle \int_0^R \overline{\alpha^3} N r \, dr \tag{41}$$

where

$$\langle u \rangle = \frac{\int_0^{R} \alpha^3 N u r \, dr}{\int_0^{R} \alpha^3 N r \, dr} \tag{42}$$

For brevity's sake, $\langle u \rangle$ will simply be called the effective particle velocity.

Substitution for N from Eq. (31) yields

$$\dot{m}_w = \frac{4}{3} \rho_w \lambda \langle u \rangle \int_0^{R} \frac{\alpha_{32}}{\overline{\overline{K}}_s} K_\lambda \, r \, dr \tag{43}$$

where α_{32} is an effective nondimensional particle size defined as the ratio of the third to the second moment of $\phi(\alpha)$. In other words, it is the ratio of mean particle volume to mean particle cross section:

$$\alpha_{32} = \frac{\int_0^{\infty} \alpha^3 \phi(\alpha) \, d\alpha}{\int_0^{\infty} \alpha^2 \phi(\alpha) \, d\alpha} = \frac{\pi}{\lambda} \frac{\overline{D^3}}{\overline{\overline{D^2}}} \tag{44}$$

The natural occurence of this ratio stems from the dependence of $\dot{m}_w$ on the particle volume together with the dependence of scattering on the particle cross section. This ratio is an integral part of the present analysis since we are treating $\dot{m}_w$ as one of our deterministic data.

It may be mentioned that α_{32} has also been introduced by other investigators [33] solely for the purpose of basing the scattering analysis on a volume density rather than a number density. In that case, α_{32} assumes the role of a conversion factor. Other scattering "diameters", appropriate in special situations, may also be defined by the moment-ratio method, i. e. [34],

$$\alpha_{pq} = \left[\frac{\int_0^\infty \alpha^p \phi(\alpha)\, d\alpha}{\int_0^\infty \alpha^q \phi(\alpha)\, d\alpha} \right]^{p-q} \tag{45}$$

We shall not need to make use of any α_{pq} other than α_{32}.

Proceeding formally, one further average is defined as

$$\left\langle \frac{\alpha_{32}}{\overline{\overline{K}}_s} \right\rangle = \frac{\int_0^R \frac{\alpha_{32}}{\overline{\overline{K}}_s} K_\lambda\, r\, dr}{\int_0^R K_\lambda\, r\, dr} \tag{46}$$

such that $\dot{m}_w$ may be expressed,

$$\dot{m}_w = \frac{4}{3} \rho_w \lambda \langle u \rangle \left\langle \frac{\alpha_{32}}{\overline{\overline{K}}_s} \right\rangle \int_0^R K_\lambda\, r\, dr \tag{47}$$

The ratio, $\overline{\overline{K}}_s / \alpha_{32}$, has been termed the specific scattering area coefficient [33].

Since no water is entrained from the atmosphere, $\dot{m}_w$ is a conserved quantity with respect to jet axial distance. Further, $K_\lambda(r,z)$ is a measureable quantity as shown earlier. Therefore the integral in Eq. (47) may be determined either numerically from the Abel-inverted data or by utilizing a property of the Abel transformation to obtain it directly. This is discussed in the section on data reduction. There remain but two unknowns in the equation: $\langle u \rangle$ and $\langle \alpha_{32}/\overline{\overline{K}}_s \rangle$. If the experiment is performed at two separate wavelengths, λ_1 and λ_2, with the same jet flow conditions, then the following ratio may be formed:

$$\frac{\left\langle \dfrac{\alpha_{32}}{\overline{\overline{K}}_s} \right\rangle_{\lambda_1}}{\left\langle \dfrac{\alpha_{32}}{\overline{\overline{K}}_s} \right\rangle_{\lambda_2}} = \frac{\lambda_2}{\lambda_1} \frac{\int_0^R K_{\lambda_2} \, r \, dr}{\int_0^R K_{\lambda_1} \, r \, dr} \tag{48}$$

The right hand side of this equation is measured. The left hand side depends only on $\phi(\alpha)$ for a particular scattering fluid. As it stands, the equation applies to a polydisperse medium whose $\phi(\alpha)$ may also depend on r and z. It is of questionable utility, however, unless further information on the behavior of $\phi(\alpha)$ with respect to r may be inferred. At this point, it is appropriate to scrutinize the average, Eq. (46) , more closely.

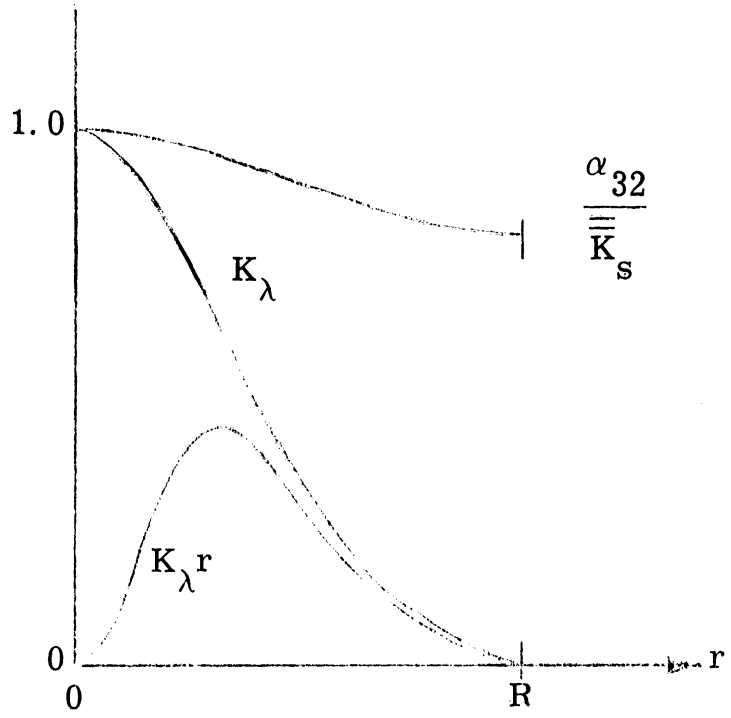

NORMALIZED RADIAL VARIATION OF VARIABLES IN THE DEFINITION OF $\langle \alpha_{32}/\bar{\bar{K}}_s \rangle$

For small variation of $\alpha_{32}/\bar{\bar{K}}_s$, the normalized radial curves for two wavelengths will be approximately the same shape and therefore the averages $\langle \alpha_{32}/\bar{\bar{K}}_s \rangle$ for each λ should be indicative of the same jet location. One could therefore remove the brackets and specify the ratio, Eq. (48), as

$$\frac{\left.\dfrac{\bar{\bar{K}}_s(r')}{\alpha_{32}(r')}\right|_{\lambda_2}}{\left.\dfrac{\bar{\bar{K}}_s(r')}{\alpha_{32}(r')}\right|_{\lambda_1}} = \frac{\lambda_2}{\lambda_1} \frac{\displaystyle\int_0^R K_{\lambda_2} \, r \, dr}{\displaystyle\int_0^R K_{\lambda_1} \, r \, dr} \tag{50}$$

where r' signifies the radial position given the greatest weight. The complete data reduction analysis, to be further specified below, could therefore be carried out and all results attributed to this heavily-weighted annular region. This, in itself, would constitute a worthwhile measurement. The situation actually measured has broader applicability than this, however. The qualitative behavior of the ratio above, as explained in Section IV-D, indicates that $\phi(\alpha)$ is sufficiently narrow as to be adequately represented by a delta function and, furthermore, the average particle size, α_{32}, does not vary to any measurable degree in the radial direction. This fortunate situation is attributable to the extreme velocity difference (Appendix B) between the supersonic outer jet and the subsonic fuel jet, a velocity difference which leads to narrow $\phi(\alpha)$ and small $\alpha_{32} \simeq \bar{\alpha}$. In what follows, the brackets on the average, $\langle \alpha_{32}/\bar{\bar{K}}_s \rangle$, will therefore be omitted and the specific scattering-area coefficient assumed independent of radius. The $\langle u \rangle$ must be retained however.

The data analysis procedure is as follows. A plot (Fig. 26) of $\bar{\bar{K}}_s/\alpha_{32}$ versus α_{32}, for various $\phi(\alpha)$, is constructed on log-log paper. The wavelengths λ_1 and λ_2 are chosen such that both α_{32} will lie in the region of most rapid $\bar{\bar{K}}_s/\alpha_{32}$ variation. This is estimated by extrapolation of existing subsonic data or by actually performing two measurements and checking the slopes obtained. It is a self-checking procedure.

Since D_{32} (or $\overline{D}$) is the same for both wavelengths, $\alpha_{32}(\lambda_1)$ will be related to $\alpha_{32}(\lambda_2)$ by the ratio λ_2/λ_1. Choose $\lambda_2 > \lambda_1$ such that $\alpha_{32}(\lambda_1)/\alpha_{32}(\lambda_2)$ is greater than one. On log-log paper, the abscissal separation of $\alpha_{32}(\lambda_1)$ and $\alpha_{32}(\lambda_2)$ is of length $\log(\lambda_2/\lambda_1)$. Similarly, the ordinal separation of $(\bar{\bar{K}}_s/\alpha_{32})_{\lambda_1}/(\bar{\bar{K}}_s/\alpha_{32})_{\lambda_2}$ is of length

$$\log\left[\frac{\lambda_1}{\lambda_2}\frac{\int_0^R K_{\lambda_1} r\,dr}{\int_0^R K_{\lambda_2} r\,dr}\right] \tag{51}$$

Thus, the slope defined by the two solution points $(\bar{\bar{K}}_s/\alpha_{32})_{\lambda_1}$ and $(\bar{\bar{K}}_s/\alpha_{32})_{\lambda_2}$ is a measurable quantity. From inspection of Fig. 26 it is seen that the slope of $\bar{\bar{K}}_s/\alpha_{32}$ is fairly constant at +3 on the Rayleigh scattering ($\alpha_{32} \ll 6$) side of the main peak and is predominantly negative at $\simeq -2$ on the Mie scattering side. This behavior can be utilized to qualitatively define the region of investigation. It is seen that a continuous range of α_{32} satisfies the slope criterion in the regions $\alpha_{32} \to 0$ and $\alpha_{32} \to \infty$. This is the reason for avoiding these regions by optimizing the choice of wavelengths. It might be mentioned that this slope method would not be needed in the $\alpha_{32} \to \infty$ region since $\bar{\bar{K}}_s$ could then be assumed known and equal to two. The short wavelengths needed to do so, however, would lie out of the responsive range of the PbS cell in the monochromator.

There are many ways to search $\bar{\bar{K}}_s/\alpha_{32}$ versus α_{32} for simultaneous solution points. A simple and entirely adequate method is to construct a transparent overlay upon which is printed a right triangle whose sides are the ordinal and abscissal lengths measured. In this way, the particle size, D_{32}, may be determined. An additional measurement at another wavelength may be needed to resolve a multiple valued solution among the side lobes of $\bar{\bar{K}}_s/\alpha_{32}$. This was unnecessary in the present investigation. Knowing D_{32}, a curve of $\overline{K_s\alpha^2}$ versus α_{32} for the appropriate $\phi(\alpha)$ then allows the determination of N(r) from

$$N(r) = \frac{4\pi\, K_\lambda(r)}{\lambda^2\, \overline{K_s\alpha^2}} \tag{52}$$

Note that $\dot{m}_w$ was not actually needed to determine D_{32} and N(r) although the expression for $\dot{m}_w$ was used as a guide to formulate the necessary ratios. Knowledge of $\dot{m}_w$ now allows the further determination of the effective particle velocity, $\langle u \rangle$, from Eq. (47) . This velocity, by reasoning analogous to that employed for $\langle \alpha_{32}/\bar{\bar{K}}_s \rangle$, should be representative of the particle velocity at a radial position slightly removed from the centerline. Viewed alternatively, it is the velocity all particles would have in a truly one dimensional, slug-type flow.

C. DATA REDUCTION

In the preceeding section, the formal light scattering equations were developed. There are a number of simplifications which can be made to facilitate data reduction. It will be shown here that all centerline values of N, together with $\overline{D}$ and $\langle u \rangle$ may be obtained without actually performing a numerical Abel inversion. The radial variation of K_λ and, consequently, of N is the only datum requiring inversion. Further, an integral radius, r_1, can be defined as a measure of the rate of spreading of the water jet. Finally, in the initial region of the jet, measured $K_\lambda(r)$ profiles were found to be closely gaussian. The resulting simplification in the scattering equations is developed herein.

C.1. Numerical Abel Inversion

There are many Abel inversion techniques reported in the literature [35, 36, 37]. The digital techniques essentially convert from plane to annular strata by ascribing a weight to individual segments of the optical path, fitting the data with a polynomial, and summing over the path. The simplest polynomial is a constant; that chosen is a parabola [36]. Higher order curve-fits rapidly compound the computational difficulty and may lead to over-fitting [38]. The inversion technique of Nestor and Olsen, outlined below, was programmed for digital computation on an LGP-30 computer.

If $a_\lambda(y)$ is an experimentally obtained transverse absorptance scan, then $K_\lambda(r)$ is the quantity sought. (See Eq. (35).) Let the transverse coordinate be subdivided into n equal segments such that

$$y = \frac{j}{n} R \quad , \quad j = 0, 1, \ldots, n$$

The absorptance is then read at n + 1 values of the transverse index, j. If k is the radial index, then the program output may be written

$$K_\lambda(r = \frac{k}{n}R) = -\frac{2n}{\pi R}\left[\sum_{j=k+1}^{n}(B_{k,j-1} - B_{k,j})X_j - B_{k,k}X_k\right] \quad (53)$$

where the $B_{j,k}$ are the weighting coefficients pertinent to the parabolic fit and the geometry:

$$B_{j,k} = \frac{[(j+1)^2 - k^2]^{1/2} - [j^2 - k^2]^{1/2}}{2j+1} \quad (54)$$

and the

$$X_j = -\ln[1 - a_\lambda(y = \frac{j}{n} R)] \quad (55)$$

are the program input data.

The grid size, n, is not arbitrary but depends on the quality of the data [38]. Runs with n = 10 and n = 20 were both employed. The program was checked by inserting a gaussian transverse distribution whose radial inversion is also gaussian. Characteristically, the machine-inverted profile lies below the analytically inverted profile (Fig. 14);

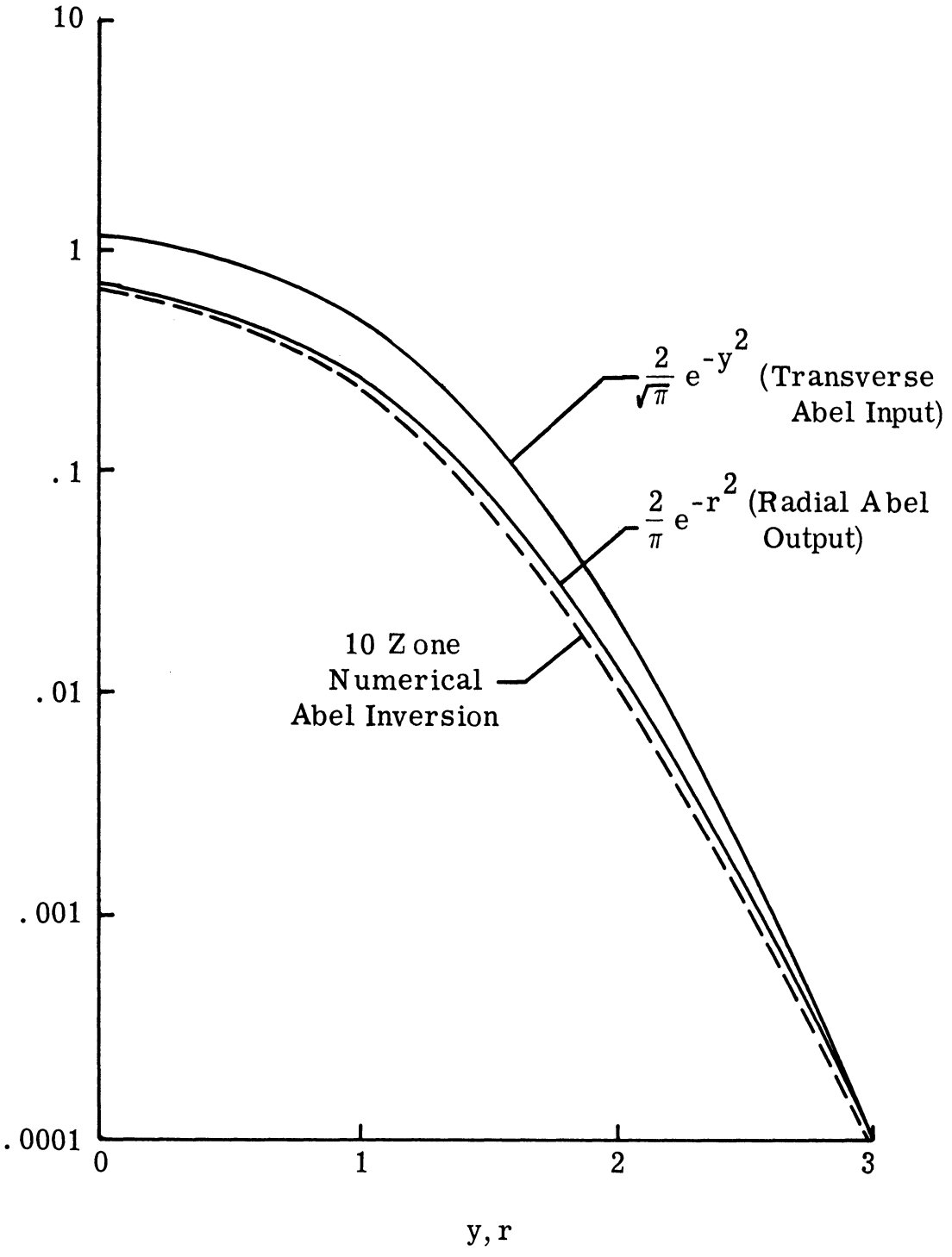

Figure 14. Numerical Abel Inversion of a Gaussian Transverse Profile

the agreement improving as n increases. With n = 20, the computed and actual radial profiles are indistinguishable when plotted. Actual data runs, with their associated uncertainties, exhibited anomalous behavior, to varying degree, at the end points. Since the point, R, at which the absorptance vanishes is difficult to pinpoint, the value of $K_\lambda(R)$ occasionally went negative when coarse grids were used. This is due to the parabolic fit which requires integral consistency of K_λ over three adjacent annuli. The interior points all fell on a smooth curve so that no difficulty was encountered in extrapolating to r = R where K_λ is defined equal to zero. Instead of setting $a_\lambda(R) = 0$ exactly, a very small, and unmeasurable, value was inserted in an attempt to remedy the r = R anomaly. In this case, $K_\lambda(R)$ did not go as far negative but the interior points showed no change within measurement accuracy (three significant figures). Therefore, all subsequent runs were performed with $a_\lambda(R) = 0$.

On the other hand, fine grid sizes produced no significant discrepancy at r = R but did behave erratically at r = 0. What is occuring here is that the final computational annulus (a cylinder of radius, R/n) has to compensate for all accumulated error over the relatively large path leading up to it. Thus, a small data smoothing error affecting the radius of curvature at r = 0, will cause $K_\lambda(0)$ to vary disproportionately.

As with the coarser grid runs, interior points were much more faithfully reproduced and extrapolation to r = 0 was possible. This was not necessary, however, because $K_\lambda(0)$ is determinable with greater accuracy by an integral technique to be discussed below.

C. 2. Integral Relations and Centerline Values

This section deals with a number of simplifications which may be applied in the data reduction process. Without loss of generality, most variables of interest, including the centerline variation of number density, may be obtained without Abel inversion.

The expression, Eq. (47), for $\dot{m}_w$ contains the integral of K_λ with respect to cross-sectional area. Since K_λ is determinable via an Abel transform, this integral represents but one more operation on the reduced data. These two operations may be circumvented by the relation[32]

$$\pi \int_0^R K_\lambda(r)\, r\, dr = - \int_0^R \ln [1 - a_\lambda(y)]\, dy \qquad (56)$$

which states that the area under the transverse data is simply equal to the cross-sectional integral of the physical quantity sought. This relation is often used to check Abel transforms.

Whereas $- \ln [1 - a_\lambda(y)]$ is one of the transform pairs, what is initially measured is $a_\lambda(y)$ itself. Due to the presence of the natural logarithm in the above integrand, the integral may be further simplified

after integration by parts. The result is

$$\int_0^R K_\lambda(r)\, r\, dr = \frac{1}{\pi} \int_0^{a_\lambda(0)} \frac{y}{1 - a_\lambda}\, da_\lambda \tag{57}$$

where $a_\lambda(0)$ is the centerline value of the measured absorptance. In no instance was there ever measured complete absorptance so that the denominator of the integrand was never zero. The integral in question is depicted by the shaded area in the sketch below

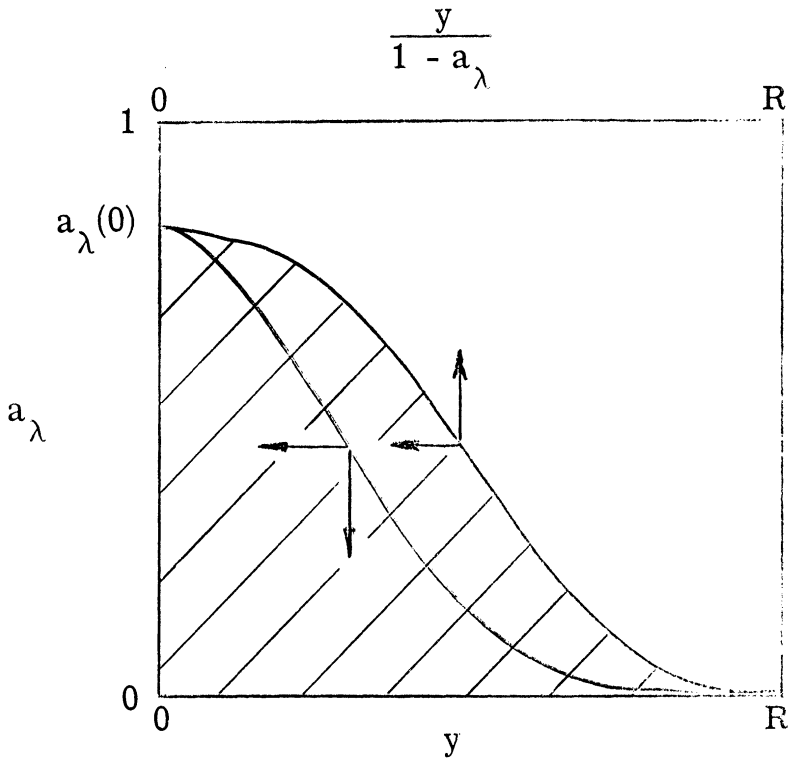

GRAPHICAL DETERMINATION OF

$$\pi \int_0^R K_\lambda(r)\, r\, dr$$

The centerline value of K_λ may be determined directly from the definition of the Abel transform (Eq. (35)) by setting the lower limit of integration equal to zero, i.e.,

$$K_\lambda(0, z) = \frac{1}{\pi} \int_0^R \frac{d}{dy} \ln [1 - a_\lambda(y)] \frac{dy}{y} \tag{58}$$

As in the previous case, this integral may be partially integrated to yield:

$$K_\lambda(0, z) = \frac{1}{\pi} \int_0^{a_\lambda(0)} \frac{da_\lambda}{y(1 - a_\lambda)} \tag{59}$$

The denominator in this case does go to zero within the range of integration but the integral is, of course, convergent since K_λ is everywhere finite. In practice, the area under the divergent portion of the integrand contributes relatively little to the integral as shown below. Since the other factors entering into K_λ do not vary significantly, $K_\lambda(0)$ is essentially a measure of N(0).

The maximum path-integrated extinction coefficient may also be obtained directly from the Abel transform definition, Eq. (34), i.e.,

$$2 \int_0^R K_\lambda(r)\, dr = - \ln [1 - a_\lambda(0)] \tag{60}$$

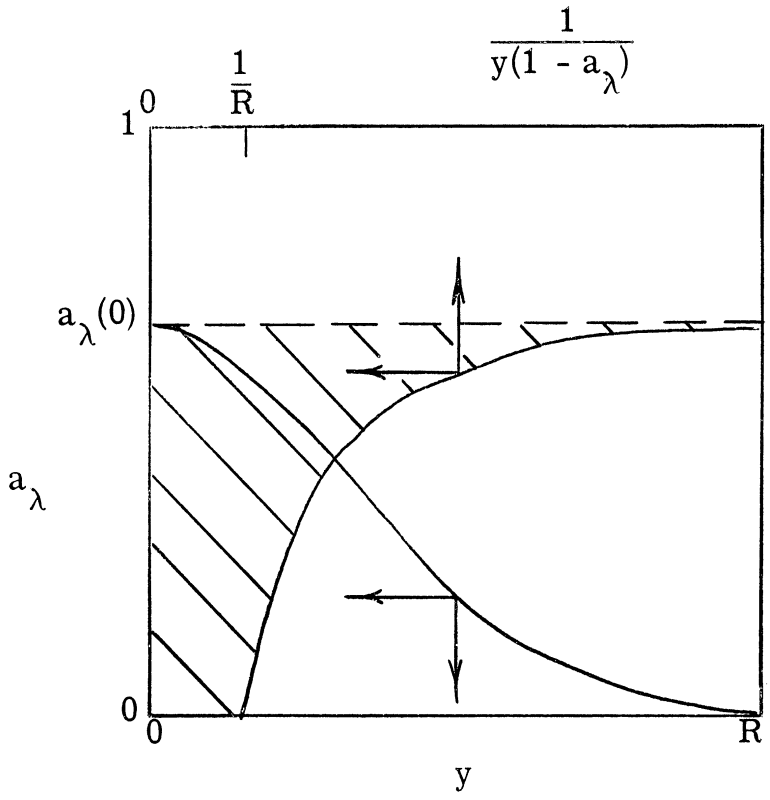

GRAPHICAL DETERMINATION OF $K_\lambda(0)$

With the aid of Eq. (57), a characteristic inner jet radius, r_1, may now be defined:

$$r_1(z) = \frac{\int_0^R K_\lambda \, r \, dr}{\int_0^R K_\lambda \, dr}$$

$$= - \frac{2 \int_0^{a_\lambda(0)} \frac{y}{1 - a_\lambda} \, da_\lambda}{\pi \ln [1 - a_\lambda(0)]} \qquad (61)$$

This radius is directly proportional to the number density "half-radius", r_N, for flows exhibiting similarity in their radial profiles (Sections IV-C.3 and IV-D). The necessity of determining the radius at which an inverted radial profile falls to one-half its centerline value is circumvented in this definition.

Another characteristic inner radius, r_2, may also be defined using the integral quantities developed in this section. It is

$$r_2(z) = \frac{\int_0^R K_\lambda \, dr}{K_\lambda(0)}$$

$$= - \frac{\pi \ln [1 - a_\lambda(0)]}{a_\lambda(0) \; 2 \int_0^{} \frac{da_\lambda}{y(1 - a_\lambda)}} \qquad (62)$$

which is also proportional to r_N in similarity flows. From Eq. (61) and (62), it is seen that the product

$$r_1 r_2 \, K_\lambda(0) = \int_0^R K_\lambda \, r \, dr \qquad (63)$$

The utility of defining these integral radii stems from the present method of measurement which is basically integral in nature. These radii are therefore easy to measure. One who was attempting to

measure the same radial profiles by an immersed probe technique would naturally prefer to deal with the easiest characteristic radius at his disposal. In that case, the half-radius, r_N, would be the obvious choice. Since the overwhelming majority of experiments of this nature have been conducted with immersed probes, r_N is the quantity which pervades the literature. The choice is solely one of convenience, however, since all quantify the same phenomenon, jet spreading. Specific example of the equivalence of r_1, r_2, and r_N is given in the next section.

Recapitulating the results of this section, the following magnitudes may be directly determined as a function of z: N(0), $\langle u \rangle$, D, r_1 and r_2. The data reduction sequence is as follows:

1. Using the ratio technique, determine K_s and D. Transverse absorptance scans at two λ's together with Eq. (57) and Fig. 26 are utilized.
2. Determine $K_\lambda(0)$ from Eq. (58) and N(0) from step 1.
3. Determine $\langle u \rangle$ from Eq. (47), the mass flux relation.
4. Determine r_1 or r_2 from Eq. (61) and (62).
5. Determine N(r) via Abel transformation.

The mass flux relation may now be written in any of the following forms:

$$\dot{m}_w = 2\pi \rho_w \int_0^R \frac{\pi}{6} \overline{D^3}\, N\, u\, r\, dr$$

$$= \frac{4}{3} \rho_w \lambda \langle u \rangle \left\langle \frac{\alpha_{32}}{\overline{\overline{K_s}}} \right\rangle \int_0^R K_\lambda\, r\, dr$$

$$= \frac{4}{3} \rho_w \lambda \langle u \rangle \left\langle \frac{\alpha_{32}}{\overline{\overline{K_s}}} \right\rangle r_1 \int_0^R K_\lambda\, dr \qquad (64)$$

$$= \frac{4}{3} \rho_w \lambda \langle u \rangle \left\langle \frac{\alpha_{32}}{\overline{\overline{K_s}}} \right\rangle \pi r_1\, r_2\, K_\lambda(0)$$

Comparing this with the familiar one-dimensional mass flux relation, $\dot{m} = \rho AV$, the following identifications may be made:

1. Effective cross-sectional area

$$A = 2\pi\, r_1\, r_2$$

2. Effective water droplet mass density

$$\rho = \frac{2}{3} \rho_w \lambda \left\langle \frac{\alpha_{32}}{\overline{\overline{K_s}}} \right\rangle K_\lambda(0)$$

$$= \rho_w \frac{\pi}{6} \overline{D^3}\, N(0)$$

3. Effective one-dimensional particle velocity

$$V = \langle u \rangle$$

These relations are useful for checking the z-variation consistency of several of the measured quantities. Moreover, in subsonic jet theory, the various magnitudes display simple power-law variation as

a function of z. It is therefore natural to inquire whether this may be the case in the present supersonic, compressible, two-phase mixing situation. Since direct probing techniques are inappropriate in two-phase flow, there is scant information available on this subject. As discussed in Section IV-D, power-law behavior is indeed evidenced in the present series of experiments.

C. 3. Gaussian Radial Distribution Approximation

The radial profile of the extinction coefficient can be closely approximated, in certain portions of the jet, by the gaussian (normal) distribution

$$\frac{K_\lambda(r)}{K_\lambda(0)} = e^{-\ln 2\left(\frac{r}{r_K}\right)^2} \tag{65}$$

where r_K is the radius at which $K_\lambda = (1/2)\, K_\lambda(0)$. Utilizing this analytic approximation to evaluate the various integrals results in further simplification in the data reduction where applicable.

From the definition of the Abel transformation, the transverse absorptance mapping is seen to obey

$$-\ln\left[1 - a_\lambda(y)\right] = 2\, K_\lambda(0) \int_y^\infty e^{-\ln 2\left(\frac{r}{r_K}\right)^2} \left(r^2 - y^2\right)^{-1/2} r\, dr$$

$$= \sqrt{\frac{\pi}{\ln 2}}\, r_K\, K_\lambda(0)\, e^{-\ln 2\left(\frac{y}{r_K}\right)^2} \tag{66}$$

It therefore follows that

$$- \ln [1 - a_\lambda(0)] = \sqrt{\frac{\pi}{\ln 2}}\, r_K\, K_\lambda(0) \tag{67}$$

and

$$y_{\ln a} = r_K \tag{68}$$

That is, the conjugate transform is also gaussian and its half-width, $y_{\ln a}$, equals the half-radius of the radial distribution. This half-width may be determined directly from the $a_\lambda(y)$ distribution via the relation

$$\frac{r_K}{y_a} = \frac{\sqrt{\ln 2}}{\sqrt{- \ln\left\{\dfrac{\ln [1 - a_\lambda(0)/2]}{\ln [1 - a_\lambda(0)]}\right\}}} \tag{69}$$

obtained by setting $a_\lambda(y_a) = (1/2)\, a_\lambda(0)$ in Eq. (66). Here, y_a is the half-width of the raw absorptance profile. This relation allows determination of r_K without actually plotting $- \ln [1 - a_\lambda(y)]$.

The integral used in the determination of K_s and D may be written for a gaussian radial variation as

$$\int_0^\infty K_\lambda(r)\, r\, dr = \frac{1}{2 \ln 2}\, r_K^{\,2}\, K_\lambda(0) \tag{70}$$

Since r_K does not change with wavelength, the ratio, Eq. (48) for two wavelengths would simply be

$$\frac{\left\langle \frac{\alpha_{32}}{\overline{\overline{K}}_S} \right\rangle_{\lambda_1}}{\left\langle \frac{\alpha_{32}}{\overline{\overline{K}}_S} \right\rangle_{\lambda_2}} = \frac{\lambda_2}{\lambda_1} \frac{K_{\lambda_2}(0)}{K_{\lambda_1}(0)} \tag{71}$$

The centerline value of the extinction coefficient may be determined from Eq. (67). Equation (71) becomes finally

$$\frac{\left\langle \frac{\alpha_{32}}{\overline{\overline{K}}_S} \right\rangle_{\lambda_1}}{\left\langle \frac{\alpha_{32}}{\overline{\overline{K}}_S} \right\rangle_{\lambda_2}} = \frac{\lambda_2}{\lambda_1} \frac{\ln \left[1 - a_\lambda(0)\right]_{\lambda_2}}{\ln \left[1 - a_\lambda(0)\right]_{\lambda_1}} \tag{72}$$

The path-integrated extinction coefficient is expressed

$$\begin{aligned} \int_0^\infty K_\lambda \, dr &= \frac{1}{2} \sqrt{\frac{\pi}{\ln 2}} \, r_K \, K_\lambda(0) \\ &= -\frac{1}{2} \ln \left[1 - a_\lambda(0)\right] \end{aligned} \tag{73}$$

With these expressions, the integral radii r_1 and r_2 may be related to $r_K = r_N$. The result is

$$r_1 = \frac{r_K}{\sqrt{\pi \ln 2}} \tag{74}$$

and

$$r_2 = \frac{1}{2}\sqrt{\frac{\pi}{\ln 2}}\, r_K \tag{75}$$

Finally, the mass flux of water may be written

$$\dot{m}_w = \frac{2}{3 \ln 2}\, \rho_w\, \lambda\, \langle u \rangle \left\langle \frac{\alpha_{32}}{\overline{\overline{K_s}}} \right\rangle r_K^{\,2}\, K_\lambda(0) \tag{76}$$

or

$$\dot{m}_w = \frac{4}{3}\sqrt{\frac{\ln 2}{\pi}}\, \rho_w\, \lambda\, \langle u \rangle \left\langle \frac{\alpha_{32}}{\overline{\overline{K_s}}} \right\rangle r_K \left| \ln\left[1 - a_\lambda(0)\right] \right| \tag{77}$$

The formulae and methods developed in this section have been applied to the supersonic coaxial mixing of water with air. The wavelengths employed were $\lambda_1 = 1.6$ and $\lambda_2 = 2.38$ chosen to lie in spectral regions devoid of water absorption and to optimize sensitivity to particle size based on the considerations of Appendix B. Results of this investigation are presented in the following section.

D. EXPERIMENTAL RESULTS

The specific scattering area coefficient, $\bar{\bar{K}}_s/\alpha_{32}$, and the mean particle size, D_{32}, have been determined by the ratio technique of Section IV-B. It was found that the monodisperse curve of Fig. 31 provided the only solution points in the entire $\bar{\bar{K}}_s/\alpha_{32}$ plane. This result leads to the conclusion that the particle size, in the jet regions measured, does not vary with radius and the particle size distribution function, $\phi(\alpha)$, is extremely narrow. Thus $\langle \bar{\bar{K}}_s/\alpha_{32} \rangle = K_s/\bar{\alpha}$ and the monodisperse relations may be used throughout the data reduction process. The particle size thus determined is $7.35 \pm 0.10\mu$. This result, obtained at an initial relative airstream velocity of 600 m/sec, compares favorably with that predicted by extrapolation from the subsonic data of Kling (Fig. 29). The oil smoke particles of Ref. 39, diffusing in a subsonic jet, also exhibit this dimensional constancy.

D.1. Axial Distributions

The axial variations of several scattering parameters are shown in Fig. 15. For these tests, the air flow rate is 500 gm/sec and the water flow rate is $7.42 \pm .2$ gm/sec. This corresponds to an initial mass flux ratio, $\rho u_w/\rho u_a = 0.44$. The path-integrated extinction coefficient is obtained from the maximum a_λ value by means of Eq. (60).

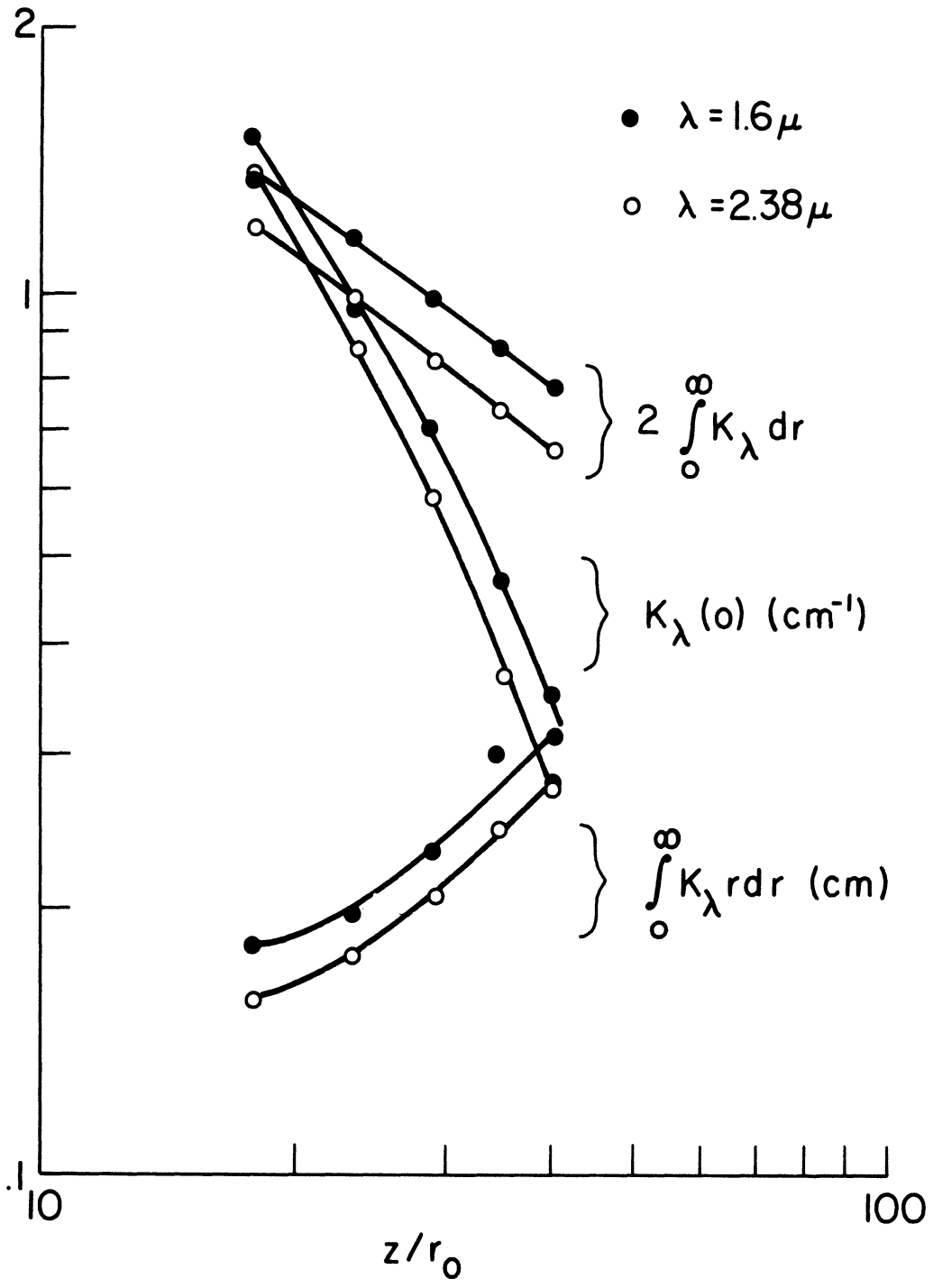

Figure 15. Axial Variation of Scattering Extinction Coefficient—Centerline Value, Path Integral, and Cross-Section Integral. ($\rho u_w/\rho u_a = 0.44$, $r_o = .893$ cm)

The cross-sectional area-integrated extinction coefficient and the centerline value of K_λ are obtained graphically via Eq. (57) and (59) respectively.

Two features are immediately apparent concerning these data: there is a quantitative difference between corresponding magnitudes measured at the two wavelengths, $\lambda_1 = 1.6\mu$ and $\lambda_2 = 2.38\mu$ and the shorter wavelength data is consistently higher in magnitude than the 2.38μ data. This behavior indicates that the wavelengths chosen are in the desired region of the K_s curve (Fig. 28). Were the wavelengths much shorter, the quantitative behavior would be reversed (Rayleigh region); were they much longer, no quantitative difference would be noticed.

The slopes of the data indicate power-law behavior over much of the measured jet length. This behavior is evidenced in two separate regions corresponding to the initial and fully-developed regions of Fig. 1. Power-law behavior is, of course, important in formulating the proper variables for similarity solutions.

Without further reduction, the integral radii, r_1 and r_2 may be obtained directly from the data of Fig. 15. In view of the constancy of D, these radii (Fig. 16) are indicative of the particle density profiles, N(r). As in subsonic flow, both radii initially increase linearly but then, due to rapid turbulent diffusion, spread as the 5/3 power of axial

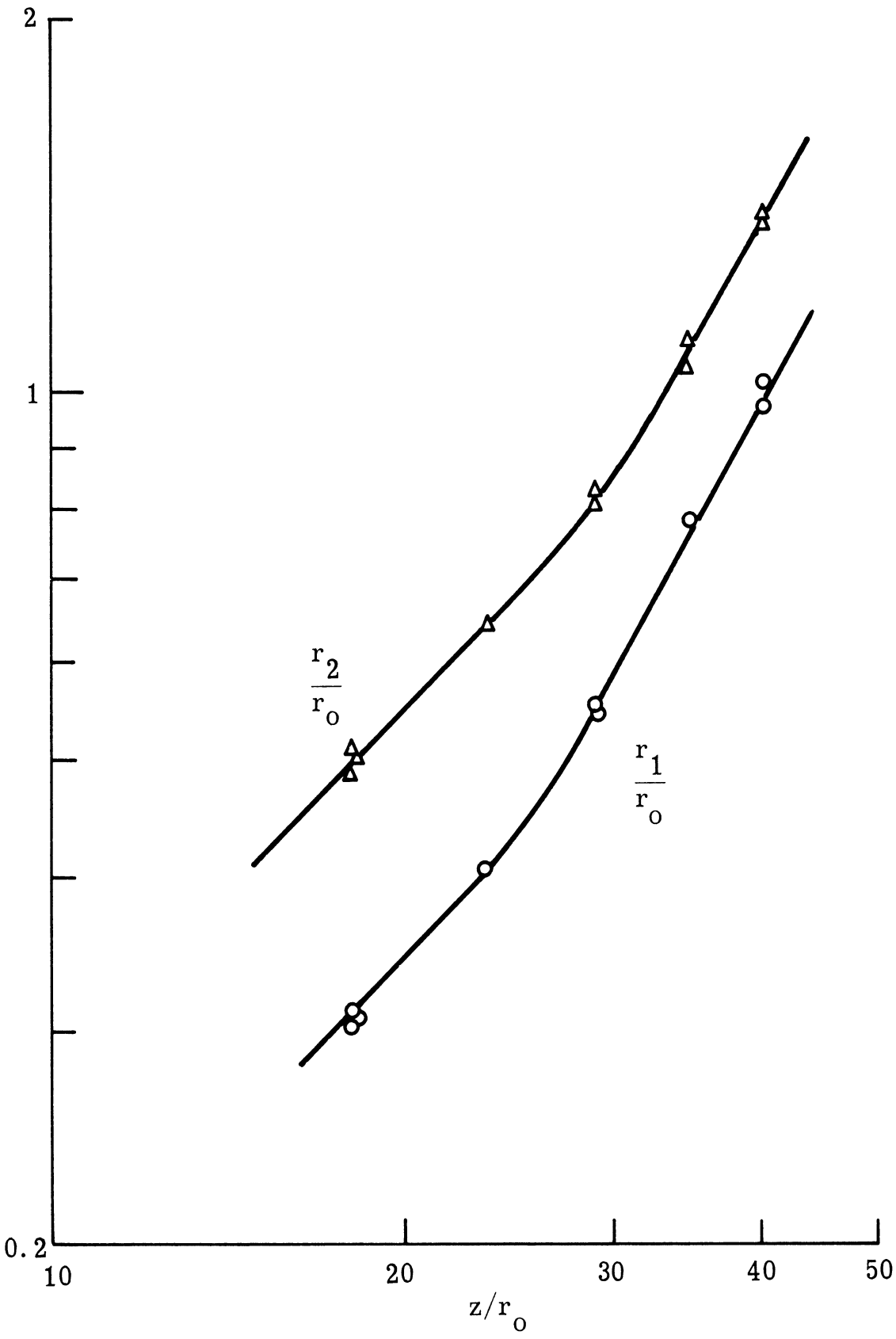

Figure 16. Axial Variation of Particle Density Integral Radii ($\rho u_w/\rho u_a = 0.44$, $r_o = 0.893$ cm)

distance. The nature of their definition requires they be proportional to each other provided the N(r) profiles exhibit similarity behavior with respect to axial distance. This proportionality is evident in the figure for $z/r_o < 20$ and again for $z/r_o > 30$. If the N(r) profile is gaussian, then $r_2 = 1.59\ r_1$. This is indeed the relation measured in the initial region and is further borne out by actual Abel inversion.

The centerline particle density is shown in Fig. 17. This is an important determination and is the subject of some controversy in the literature. As mentioned in Section I, direct probe measurements of subsonic, incompressible, mixing of two gases indicate a z^{-1} dependence for N(0). One investigator[5] has measured a z^{-2} dependence of N(0) for supersonic mixing of H_2 with air. Schetz[3] has pointed out an apparent mass flux ratio dependence for this exponent of z. For $\rho u_w/\rho u_a < 1$, the centerline concentration as measured by several investigators and reported by Schetz varies roughly as $z^{-2+0.4}$. For $\rho u_w/\rho u_a > 1$, this exponent changes abruptly to - 1. (The subscripts, w and a, here refer to any injected gas and surrounding medium respectively.) At this point, it is unclear whether this remarkable behavior is due solely to the magnitude of $\rho u_w/\rho u_a$ or if compressibility may also be influential. In either event, the present data is consistent insofar as $\rho u_w/\rho u_a$ is < 1 and the decay exponent of z is near - 2. It is possible to go further than this in discussing the present data, however.

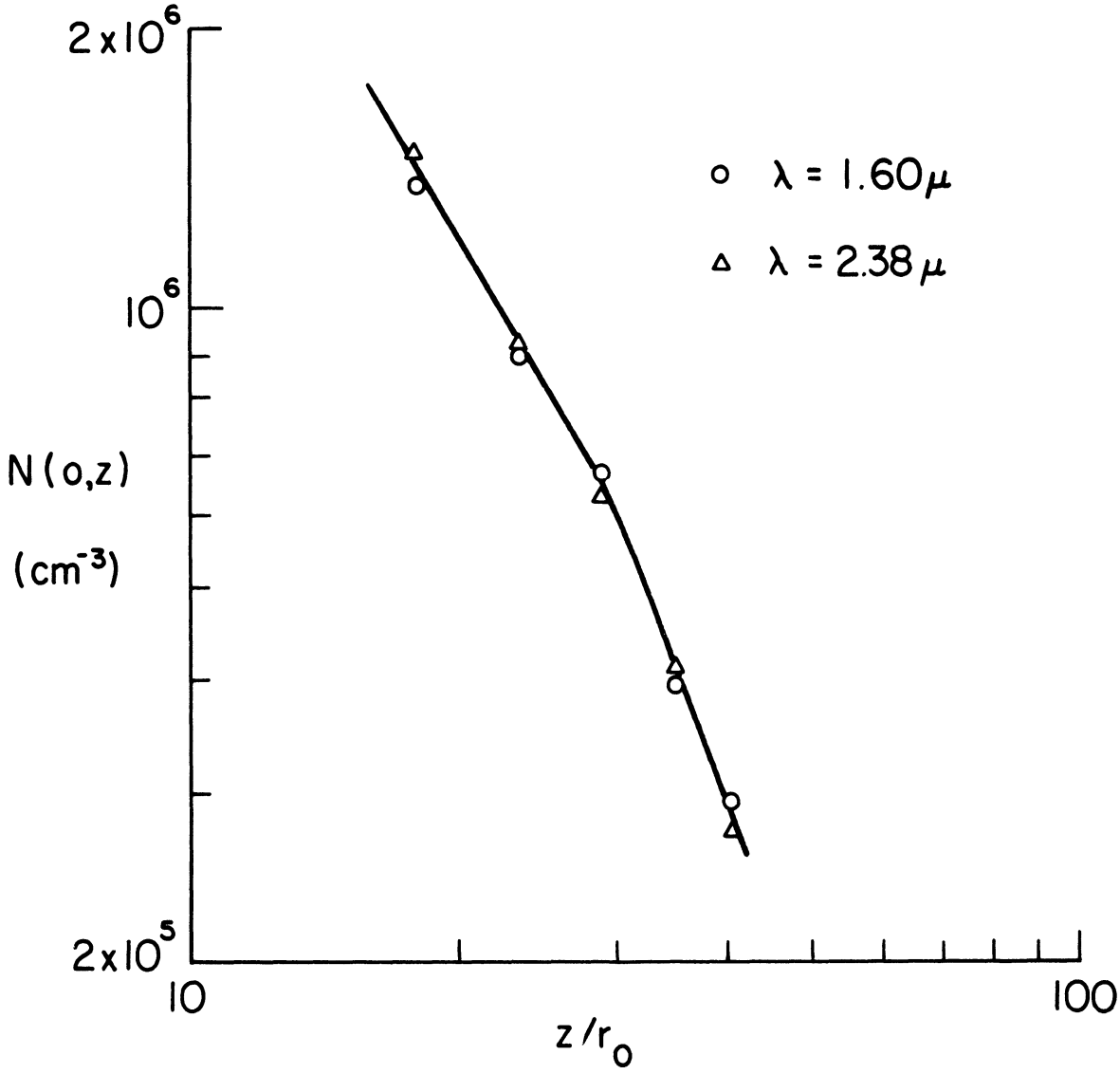

Figure 17. Centerline Variation of Particle Number Density ($\rho u_w/\rho u_a = 0.44$, $r_o = 0.893$ cm)

Since many, so-to-speak, overlapping data have been obtained by the present methods, there is ample availability of consistency checks in the data reduction process. This is evidenced by the many forms into which the injected mass flow equation may be cast (Eq. (64)). Where data concerning, say, r_2 may exhibit some scatter, there is data concerning r_1 which may not. This self-checking procedure has been employed with the result that it is certain that N(0) exhibits a change in decay exponent in the neighborhood of the air potential core's tip. The exponent in the initial region is - 5/3 and in the final region is - 7/3, values which lie slightly below and above the value 2. Recent experimental evidence[7], taken by probe at conditions corresponding to the initial region, also lend support to the value - 5/3. (The value reported by Chriss is - 1.7.)

Having determined particle size (hence K_s) and N(0, z), it is possible to equate $K_\lambda(r)/K_\lambda(0)$ with $N(r)/N(0)$. The $K_\lambda(r)$ profiles, obtained by Abel inversion, are shown for six axial stations in Fig. 18. The radial coordinate has been nondimensionalized with respect to K_λ's half-radius, r_K. It is seen that the two profiles measured in the initial region are quite closely gaussian whereas those taken further downstream depart from the gaussian curve at large radii. Advantage is taken of this gaussian behavior in Section IV-D. 2 wherein the variation of mass flux ratio is investigated.

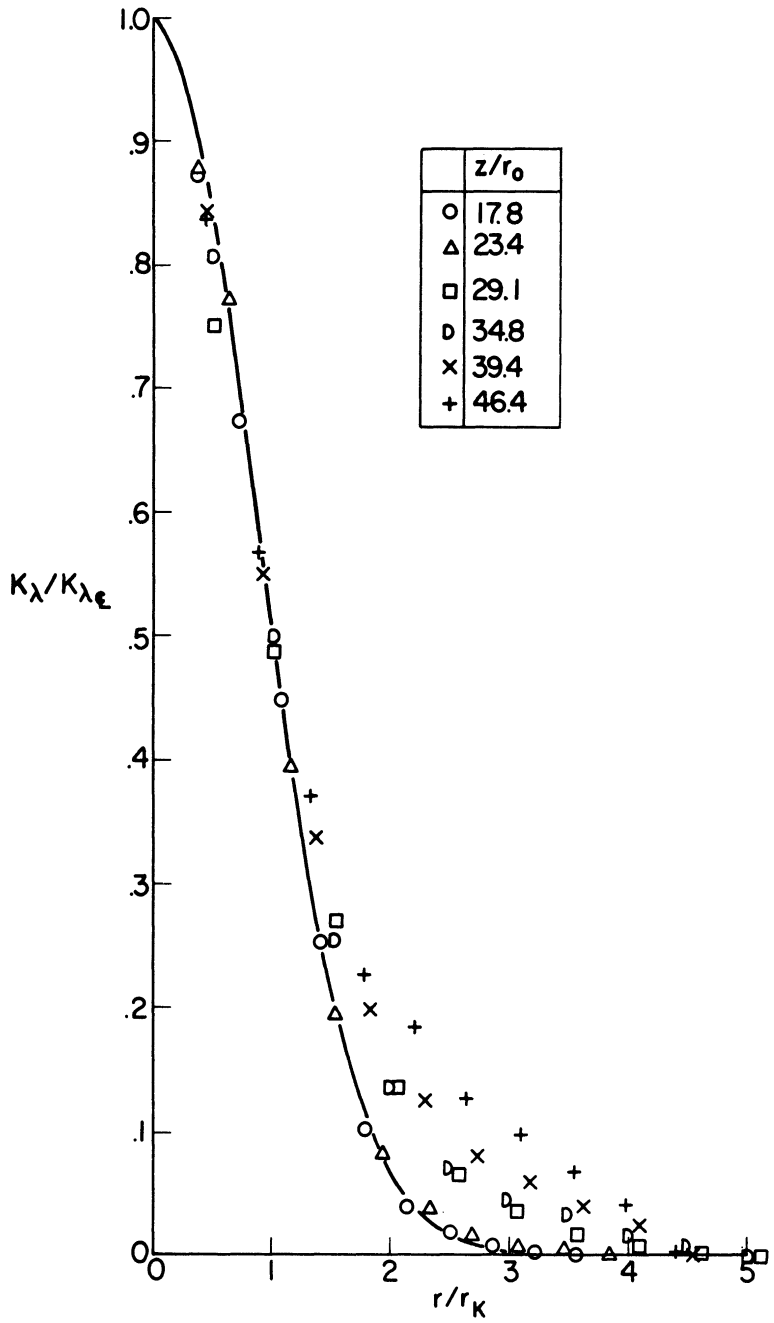

Figure 18. Radial Distribution of Scattering Extinction Coefficient at Six Axial Locations. Solid Curve —Gaussian Distribution ($\rho u_w/\rho u_a = 0.44$, $r_o = .893$ cm)

Knowing particle density as a function of r and the global mass flow rate allows the determination of the average cross-sectional particle velocity, $\langle u \rangle_w$. This quantity is shown in Fig. 19. In the final region, it is seen that $\langle u \rangle_w \sim z^{-1}$ as in the subsonic case. Although there are not sufficient points taken in the initial region to determine the slope of $\langle u \rangle_w$, consistency with r_1, r_2, and N(0) requires that $\langle u \rangle_w \sim z^{-1/3}$ in this region. This variation does not violate the concept of a potential core if it is borne in mind that $\langle u \rangle_w$ encompasses velocities both within and outside of the potential core. Also shown in the figure is the centerline air velocity obtained by a direct pitot probe measurement without water injection. For the sake of more direct comparison, the cross-sectional average air velocity was computed from probe measurements by the expression

$$\langle u \rangle_a = \frac{\int_0^\infty \rho u r \, dr}{\int_0^\infty \rho r \, dr} \tag{78}$$

in analogy with Eq. (42). It is seen that this velocity curve fairs smoothly into the $\langle u \rangle_w$ curve in the final region but lies above $\langle u \rangle_w$ in the initial region. One might be prompted to equate this difference with a slip velocity were it not for the fact that particles of this size,

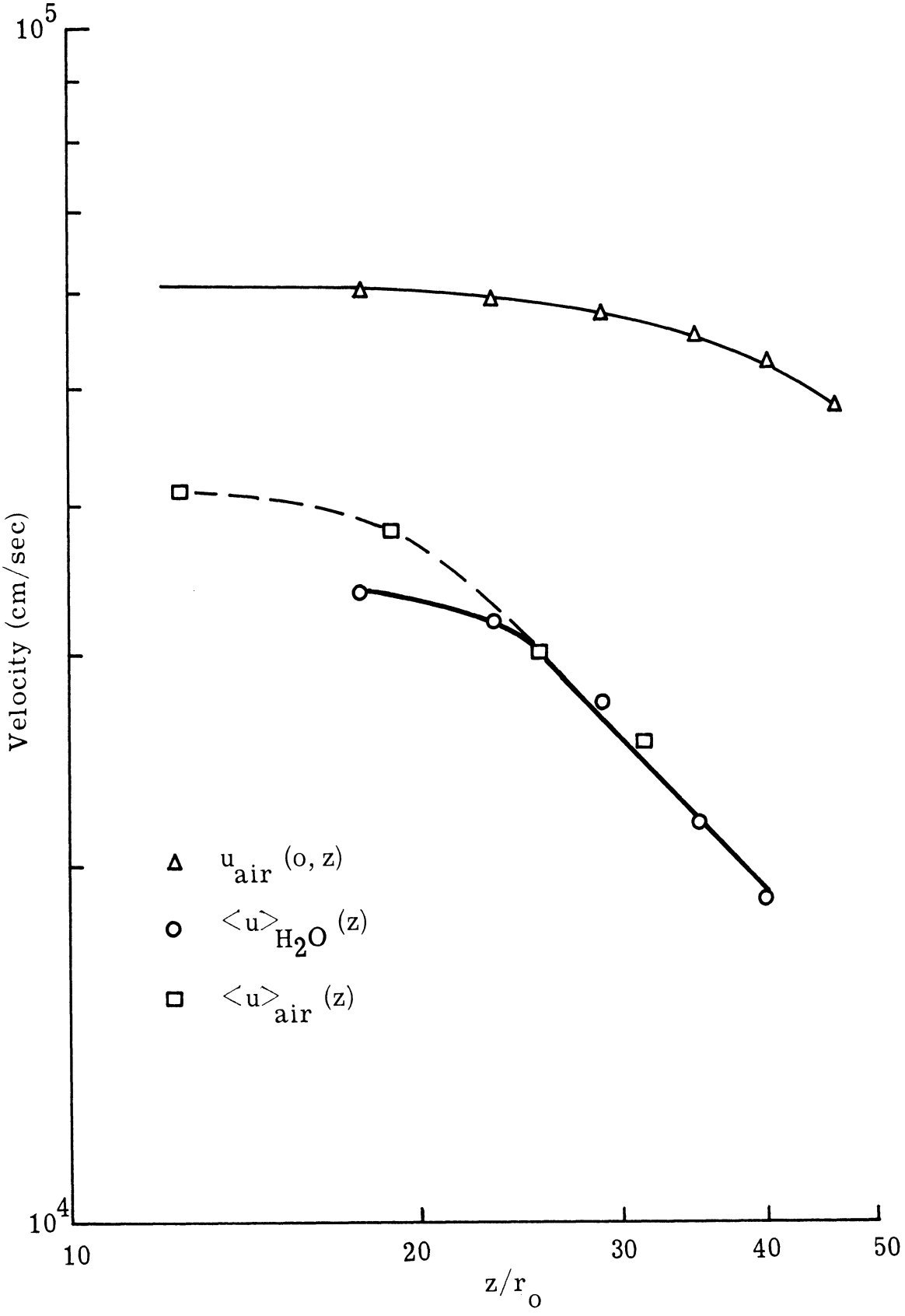

Figure 19. Centerline and Average Air Jet Velocity (without Water Injection) and Average Water Velocity versus Distance from Injection Plane ($\rho u_w / \rho u_a = 0.44$, $r_o = .893$ cm)

based on calculations using the most conservative (Stokes) drag coefficient, should be fully accommodated by the time they reach the first measurement station. A more probable explanation is that initially the water inertia exerts a local retardation on the air stream but that, as mixing progresses, the overwhelming air/fuel momentum ratio makes itself felt with the result that little difference exists in the downstream air velocity with or without injection. In this regard, the water particles might be considered as a passive contaminant.

The axial variations of several quantities measured in this test series are summarized in the table below. In considering the table, the variations ascribed to the final, fully developed, zone are to be regarded as the most reliable as more data points exist in this zone. In all cases, exponents have been estimated to the nearest fraction.

Table 1. Axial Variation of Axisymmetric Jet Mixing Parameters

	Initial Zone	Final Zone
$K_\lambda(0)$	$z^{-5/3}$	$z^{-7/3}$
$\int_0^\infty K_\lambda \, dr$	$z^{-2/3}$	$z^{-2/3}$
$\int_0^\infty K_\lambda \, r \, dr$	$z^{1/3}$	z^{1}
r_1	z^{1}	$z^{5/3}$
r_2	z^{1}	$z^{5/3}$
$N(0)$	$z^{-5/3}$	$z^{-7/3}$
$\langle u \rangle_w$	$z^{-1/3}$	z^{-1}

Inspection of the table leads to the following correspondences:

1. Variation in K_λ corresponds directly to variation in N.
2. Variation in $\int_0^\infty K_\lambda \, r \, dr$ corresponds inversely to variation in $\langle u \rangle_w$.

These correspondences are employed in the following section to infer information regarding the variations due to mass flux ratio.

D.2. Effects of Mass Flux Ratio

As mentioned earlier, the radial profile of extinction coefficient is approximately gaussian in the initial zone of the coaxial mixing jet. This approximation allows determination of many variables without Abel inversion and without integration. Since only one wavelength, 2.38μ, was employed for these measurements, the amount of information determined is less than that reported in the previous section. The behavior of the inner jet radius, $K_\lambda(0)$, and the product $\langle u \rangle_w (D/K_s)$ is described however.

Whereas $\dot{m}_w$ was a conserved quantity in the preceding section, it is essentially the independent variable in the present situation due to the fact that $\dot{m}_a$ is held constant at 500 gm/sec. Thus $\dot{m}_w \sim \dot{m}_w/\dot{m}_a \sim \rho u_w/\rho u_a$. Another variable which must be considered as such in this section is D/K_s which may be a weak function of fuel/air ratio[40, 41] The form of the water mass flow equation containing the least number of individual factors is

$$\frac{\rho u_w}{\rho u_a} \sim \frac{D}{K_s} \langle u \rangle \int_0^\infty K_\lambda \, r \, dr \tag{79}$$

obtained from Eq. (64). In the gaussian approximation, the integral is replaced by

$$\int_0^\infty K_\lambda \, r \, dr = \frac{1}{2 \ln 2} r_K^2 \, K_\lambda(0) \tag{80}$$

where r_K and $K_\lambda(0)$ are determined from Eq. (68) and (73).

The variation of $\int_0^\infty K_\lambda \, r \, dr$ with respect to mass flux ratio is shown in Fig. 20 . It is seen that this integral is not quite proportional to mass flux ratio, the exponent of $\rho u_w / \rho u_a$ being 5/6. From Eq. (79), this implies the product, $(D/K_s) \langle u \rangle$, varies as the 1/6-power of $\rho u_w / \rho u_a$.

The variation of $K_\lambda(0)$ and $\int_0^\infty K_\lambda \, dr$ provide an independent check on the behavior of r_K and $\int_0^\infty K_\lambda \, r \, dr$. From Fig. 21 , it is seen that $K_\lambda(0)$ varies as $(\rho u_w / \rho u_a)^{2/3}$ while $\int_0^\infty K_\lambda \, dr$ varies as $(\rho u_w / \rho u_a)^{3/4}$. Thus, in the gaussian approximation, $r_1 \sim r_2 \sim r_K \sim (\rho u_w / \rho u_a)^{1/12}$ is the consistent dependence obtained for the jet radii. This is shown in Fig. 22 . Also shown in the figure is the maximum absorptance measured as a function of mass flux ratio. As $\rho u_w / \rho u_a$ increases, a_λ asymptotically approaches 1.0.

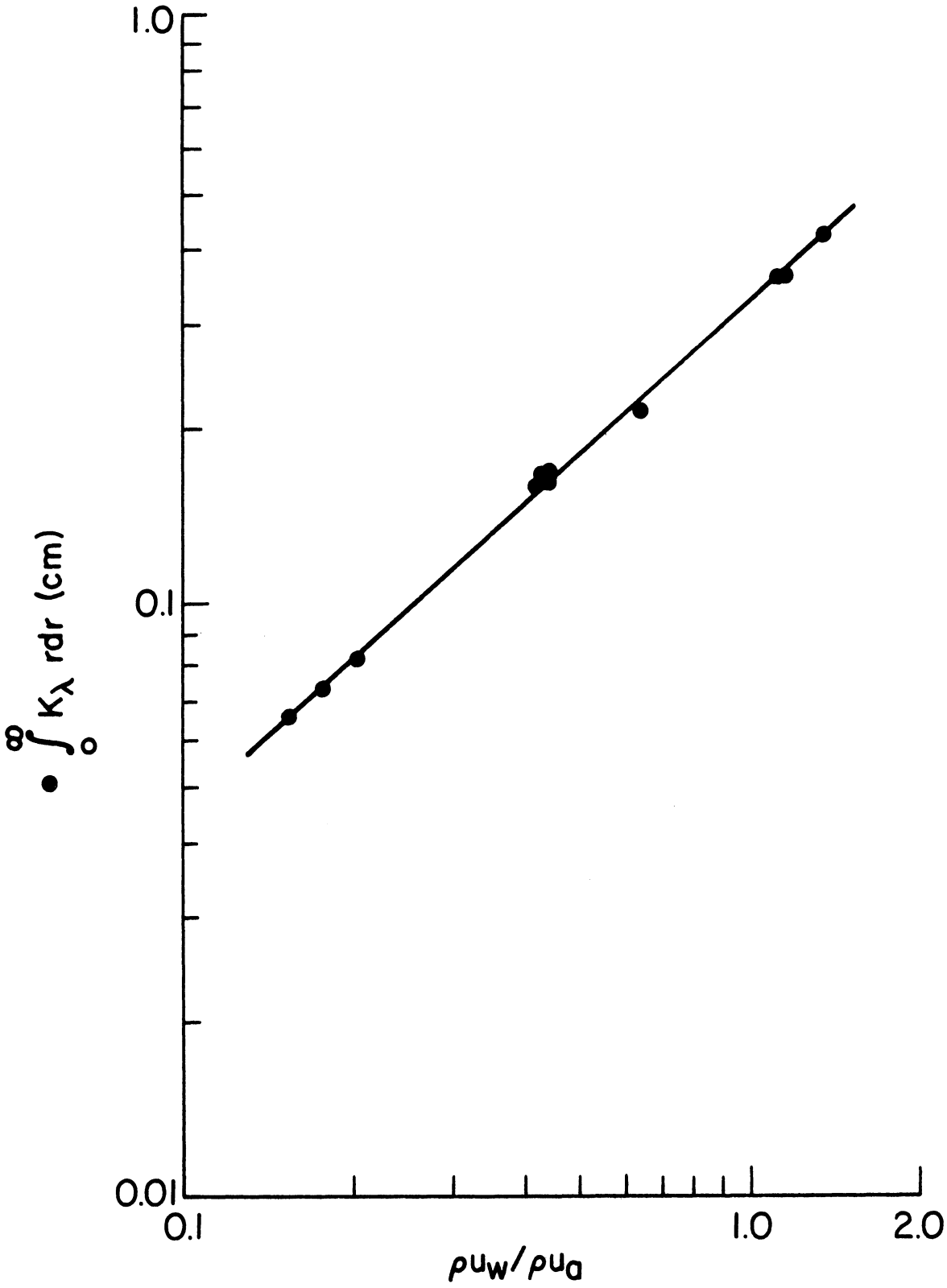

Figure 20. Variation of Area-Integrated Extinction Coefficient as a Function of Mixing Mass Flux Ratio ($z/r_o = 18$, $\lambda = 2.38\mu$)

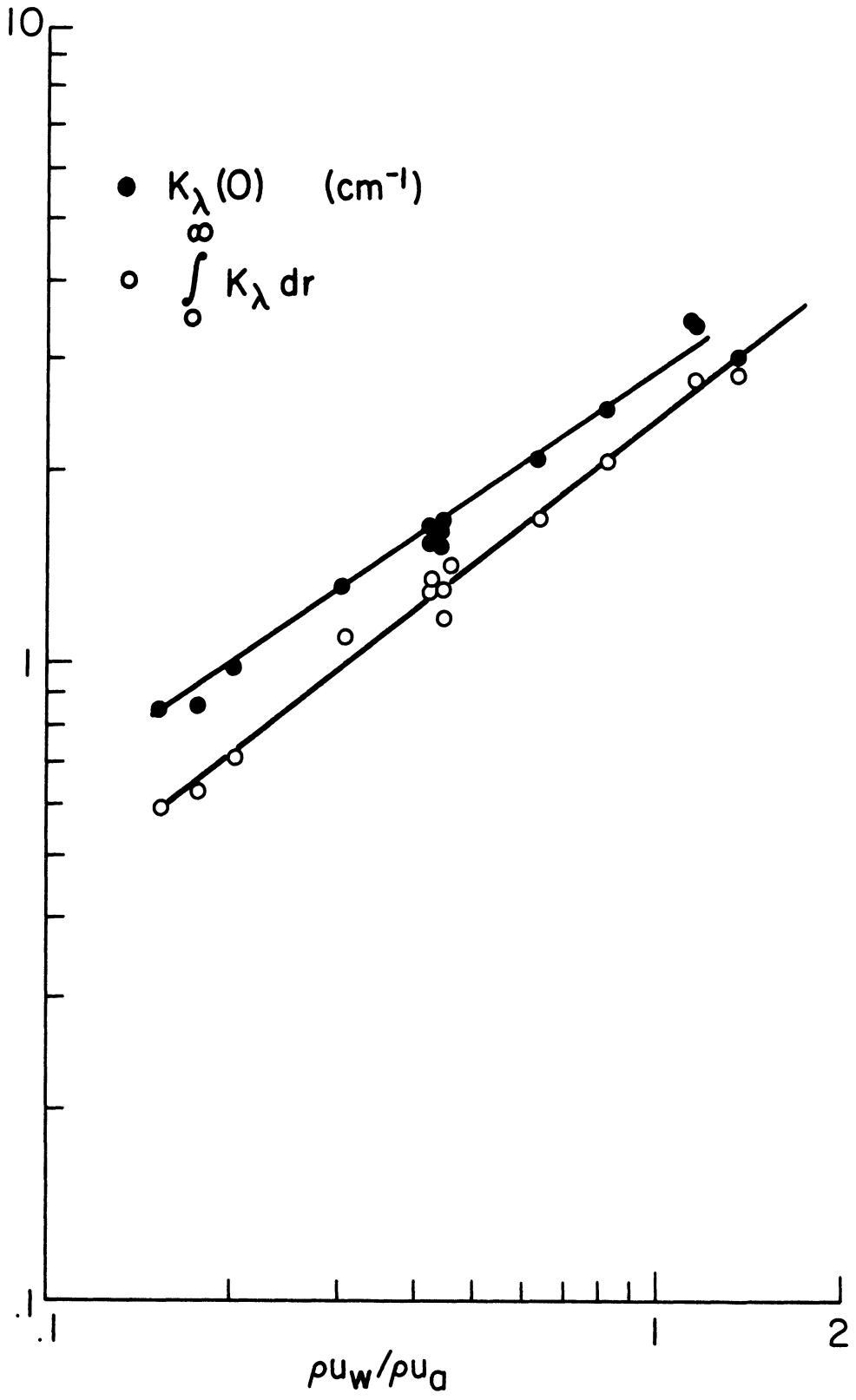

Figure 21. Variation of Extinction Coefficient (Centerline Value and Path Integral) versus Mixing Mass Flux Ratio ($z/r_o = 18$, $\lambda = 2.38\mu$)

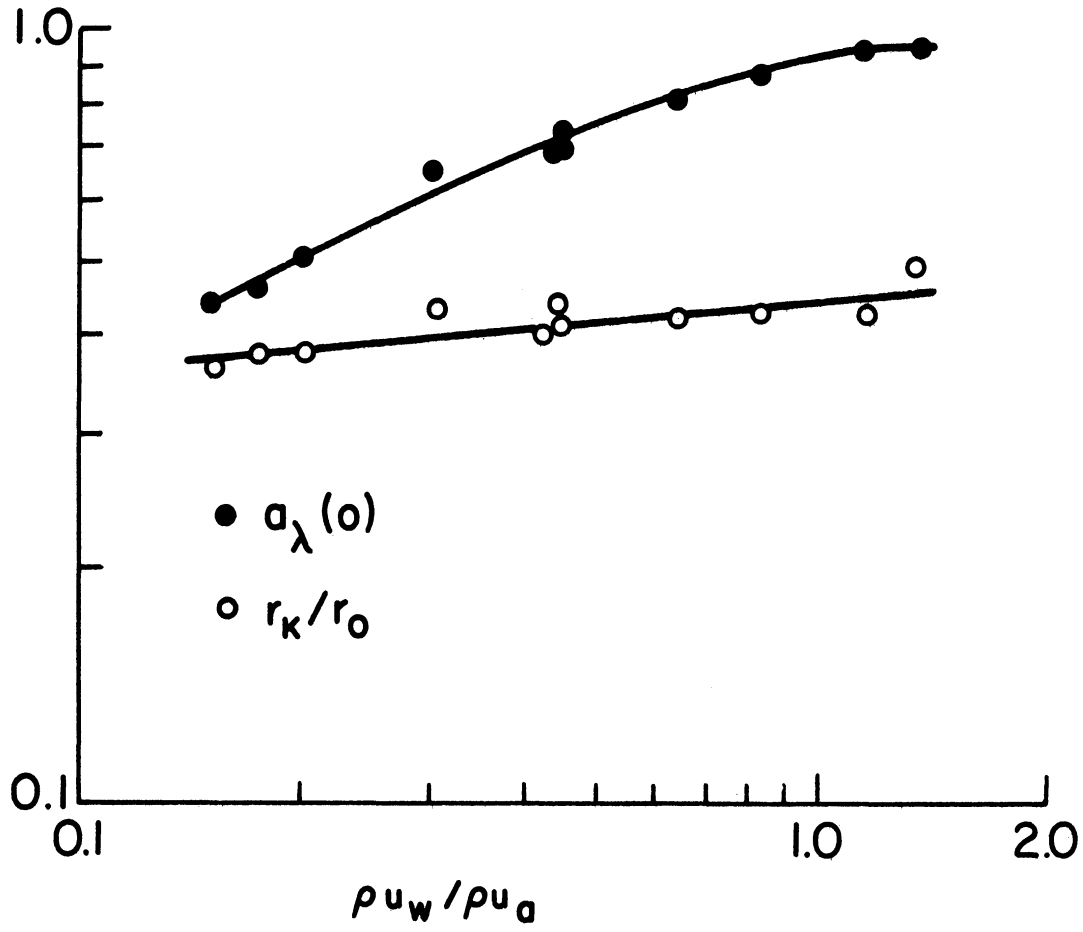

Figure 22. Variation of Maximum Absorptance and Gaussian Density Half-Radius as a Function of Mixing Mass Flux Ratio ($z/r_o = 18$, $\lambda = 2.38\mu$)

Since D was not determined explicitly as in the bi-wavelength measurements, the behavior of N(0), D, and $\langle u \rangle$ with respect to $\rho u_w / \rho u_a$ can only be speculated upon. There is of course one value, 0.44, of $\rho u_w / \rho u_a$ for which D was determined previously. This implies that K_s/D, K_s/α, and α are also known for this mass flux ratio. The α for these particular conditions is 9.65, a value which places K_s/α in a region of Fig. 26 where the local logarithmic slope is -3, i.e.

$$\frac{K_s}{D} \sim D^{-3}$$

Therefore $K_s D^2$ is locally independent of D. Thus from Eq. (52),

$$K_\lambda(0) \sim K_s D^2 N(0) \sim N(0) \sim \left(\frac{\rho u_w}{\rho u_a} \right)^{2/3}$$

The mass flux equation (79) may now be written

$$\frac{\rho u_w}{\rho u_a} \sim D^3 \langle u \rangle N(0) r_K^2 \tag{81}$$

with the result that now the reduced product $D^3 \langle u \rangle \sim \rho u_w^{1/6}$.

Two limiting cases may be considered:

$$\begin{aligned} &\text{(i)} \quad D^3 \sim \rho u_w^{1/6} \quad ; \quad \langle u \rangle \sim (\rho u_w)^0 \\ &\text{(ii)} \quad \langle u \rangle \sim \rho u_w^{1/6} \quad ; \quad D^3 \sim (\rho u_w)^0 \end{aligned} \tag{82}$$

In the first case, $D \sim (\rho u_w/\rho u_a)^{1/18}$, a result which is not inconsistent with the subsonic data of Kling (Fig. 24). In the latter case, the particle size is independent of fuel/air ratio while $<u>$ increases slightly as more fuel is injected. A possible explanation of this situation might be based on the observed fact that r_K is increased slightly with increased ρu_w and the full effect of the air momentum is felt earlier in the jet's history. There is insufficient data to resolve this question and, indeed, the truth may lie somewhere in between these limits.

Recapitulating the results of this mass flux ratio investigation, the following items are salient:

(i) Measured quantities

(a) $\int_0^\infty K_\lambda \, r \, dr \sim (\rho u_w/\rho u_a)^{5/6}$

(b) $\int_0^\infty K_\lambda \, dr \sim (\rho u_w/\rho u_a)^{3/4}$

(c) $K_\lambda(0) \sim (\rho u_w/\rho u_a)^{2/3}$

(ii) Derived quantities

(a) $r_1 \sim r_2 \sim r_K \sim (\rho u_w/\rho u_a)^{1/12}$

(b) $N(0) \sim (\rho u_w/\rho u_a)^{2/3}$

(c) $D^3 <u> \sim (\rho u_w/\rho u_a)^{1/6}$

Perhaps the most important conclusion to be reached from these considerations is that increasing fuel injection rate does not increase fuel droplet density in the same proportion. Some of the increased fuel flow results in jet spreading and in increasing the product of droplet volume times average droplet velocity.

SECTION V

ABSORPTION SPECTROSCOPY

A. INTRODUCTION

The data that are potentially measurable by spectroscopic means are number density and temperature. Knowledge of the overall mass flow rate of the spectrally active species then allows determination of its average velocity. In the present application, described in Section III, a number of the restrictions usually placed on measurements of this type must be relaxed. An example of this is the non-uniformity of the medium, a complication which is removable via the assumption of cylindrical symmetry. A greater complication is introduced by the necessity, imposed by experimental conditions, of dealing with so-called strong line absorption. In this case, an additional parameter, the line width, must be related to the thermodynamic state of the medium. Unlike the line strength, which is the only parameter necessary in the weak line approximation, the line width depends on carrier gas properties as well as those of the spectrally active gas. Fortunately, there are regimes defined by temperature and transitional quantum number for which simplifications may be made. It is the purpose of this section to explore these possibilities and to determine which assumptions are the most reasonable.

The section begins with a development of the necessary phenomenological formulae of non-homogeneous absorption. The phenomenological coefficients are then related to thermodynamic and molecular properties of the medium. Finally, the data reduction pertinent to the HF molecule is developed. An additional section, experimental results, is deferred until more data is obtained.

B. PHENOMENOLOGICAL RADIATIVE TRANSFER EQUATION

We wish to describe mathematically the net gain in energy experienced by a beam of infrared radiation as it traverses an absorbing and emitting medium. To do so, we shall characterize the medium by a phenomenological absorption and an emission coefficient which will later be related to molecular and thermodynamic properties of the medium. The notation employed will be largely that which has found acceptance by workers in the infrared portion of the spectrum. In this regard, we deal with wavenumber, ν, rather than frequency, $\nu' = c\nu$, and we express the medium's spectral characteristics on a unit partial pressure basis rather than on a volume, mass, or molar basis.

Consider the geometry of Fig. 13 wherein a beam of radiant energy is incident laterally on a cylindrically symmetric medium. The net gain in the beam's spectral radiance as it traverses a distance, dx, is given by[42]

$$\frac{dI_\nu}{dx} = pj_\nu - pk_\nu I_\nu \tag{83}$$

where I_ν = spectral radiance $\left[\text{watts/ster. cm}^{-1}\text{cm}^{2}\right]$

p = partial pressure of spectrally active species [atm]

j_ν = spectral emission coefficient per unit partial pressure $\left[\text{watts/ster. cm}^{-1}\text{cm}^{3}\text{atm}\right]$

k_ν = spectral absorption coefficient per unit partial pressure $\left[\text{atm}^{-1}\text{cm}^{-1}\right]$, defined to include stimulated emission (negative absorption)

Spectral radiance, I_ν^o, is incident on the far boundary $(-x_o, y)$ of the medium; that emerging from the near boundary is given by the integral of Eq. (83)

$$I_\nu(x_o, y) = I_\nu^o \, e^{-\int_{-x_o}^{x_o} pk_\nu dx} + \int_{-x_o}^{x_o} pj_\nu \, e^{-\int_{x}^{x_o} pk_\nu dx} \, dx \tag{84}$$

The optical path variable, ℓ, is commonly defined as beginning ($\ell = o$) at the boundary (x_o, y) nearest the observer and ending ($\ell = L$) at the far boundary $(-x_o, y)$. With this change of variable, the integral of the radiative transfer equation is written

$$I_\nu(y) = I_\nu^o e^{-\int_o^L pk_\nu d\ell} + \int_o^L pj_\nu e^{-\int_o^\ell pk_\nu d\ell} d\ell \qquad (85)$$

For gases in local thermodynamic equilibrium, Kirchhoff's law [42] relates the emission and absorption coefficients.

$$j_\nu = k_\nu I_\nu^*(T) \qquad (86)$$

I_ν^* is the spectral radiance of a black body at temperature T and is given by Planck's radiation formula[43]

$$I_\nu^* = 2c^2 h\nu^3 \left(e^{hc\nu/kT} - 1\right)^{-1} \qquad (87)$$

C. SPECTRAL ABSORPTANCE AND EQUIVALENT WIDTH OF COLLISION BROADENED LINE PROFILES

In the absence of emission, the net spectral radiance emerging from the near boundary of Fig. 13 is simply

$$I_\nu = I_\nu^o \, e^{-\int_o^L pk_\nu d\ell} \tag{88}$$

The spectral absorptance is defined

$$a_\nu(y) = \frac{I_\nu^o - I_\nu(y)}{I_\nu^o} = 1 - e^{-\int_o^L pk_\nu d\ell} \tag{89}$$

i. e., it is the fraction of incident spectral radiance lost due to molecular absorption.

At this point, it is appropriate to consider mechanisms and expressions for the broadening of the line profile, k_ν. Two mechanisms, molecular collisions and thermal velocity, are influential in the present context. The former is termed Lorentz broadening and is characterized by the contour[43],

$$k_\nu = \frac{S}{\pi} \frac{b}{b^2 + (\nu - \nu_m)^2} \tag{90}$$

where ν_m = line center wavenumber

b = line width (the half-width at half-height) $\left[cm^{-1}\right]$

S = line strength $\left[atm^{-1}cm^{-2}\right]$

$$= \int_{\text{line}} k_\nu d\nu$$

The latter mechanism, termed doppler broadening, has as its profile the normal curve[44]

$$k_\nu = \sqrt{\frac{\ln 2}{\pi}} \frac{S}{b_D} e^{-\ln 2 \left(\frac{\nu - \nu_m}{b_D}\right)^2} \tag{91}$$

The combined profile, termed the Voight profile, is given by[45]

$$k_\nu = \frac{a}{\pi}\sqrt{\frac{\ln 2}{\pi}} \frac{S}{b_D} \int_{-\infty}^{\infty} \frac{e^{-y^2}}{a^2 + (w - y)^2} dy \tag{92}$$

where $w = (\nu - \nu_m/b_D)\sqrt{\ln 2}$

$a = (b/b_D)\sqrt{\ln 2}$, Voight parameter

It is usually the case in the infrared region at moderate temperatures that $b \gg b_D$. This is borne out by the following calculation. The doppler half width is given by[44]

$$b_D = \frac{\nu_m}{2c}\sqrt{\frac{8RT}{\mathcal{M}} \ln 2} \tag{93}$$

where R is the universal gas constant. Inserting values appropriate to the fundamental rotation-vibration band of HF at 300°K, we obtain $b_D = 5.6 \times 10^{-3}\ cm^{-1}$.

A conservative estimate of the Lorentz half-width is given by the billiard ball collision approximation[42]

$$b = b_o \frac{p}{p_o} \sqrt{\frac{T_o}{T}} \tag{94}$$

where $b_o = 0.09\ cm^{-1}$

$p_o = 1$ atm

$T_o = 373°K$

At one atmosphere and 300°K, $b \simeq 0.1\ cm^{-1}$. The Voight parameter corresponding to these conditions is $a \simeq 15$, a value which enters into the determination of equivalent width discussed below.

Monochromators in the IR region rarely have sufficient resolution (Appendix D) to measure the a_ν profile exactly. The measured absorptance is distorted by the slit function of the monochromator. The distorted line profile does encompass the same area as the true line profile however (Section V-E). Thus the equivalent width

$$W_\nu = \int_{\text{line}} a_\nu d\nu \tag{95}$$

is the prime measured quantity. Yamada[45] has shown that, for values of the Voight parameter, a, greater than 0. 5, W_ν is completely specified by the Ladenburg-Reiche curve of growth which is pertinent to collision broadened profiles only. For a homogeneous path, the Ladenburg-Reiche formula is

$$W_\nu = 2\pi b x e^{-x} \left[J_0(ix) - iJ_1(ix) \right] \tag{96}$$

where $x = pSL/2\pi b$. J_0 and J_1 are Bessel functions of the first and second order. The awkwardness of this expression has resulted in a number of simplified analytic approximations to it[46]. Its generalization to include the nonhomogeneous path situation has been accomplished by Simmons[47].

There are two limiting situations wherein the equivalent width is a simple algebraic function of the path variables: the weak and the strong line approximations. In the general nonhomogeneous case, these are[19]:

$$W_\nu = \int_0^L pS d\ell \qquad \text{(weak line)} \tag{97}$$

and

$$\frac{W_\nu^2}{4} = \int_0^L bpS d\ell \qquad \text{(strong line)} \tag{98}$$

which are valid when $\int_0^L pk_\nu d\ell$ is much less than or greater than one, respectively.

Expressing ℓ in terms of y and r reveals that measurement of $W_\nu(y)$ is equivalent to measurement of pS(r) or bpS(r) through the use of the Abel transformation (Section IV). It remains to relate this measurement to the thermodynamic state of the medium.

D. LINE STRENGTH AND LORENTZ LINE WIDTH

In general, the computation of a diatomic molecule's rotation—vibration line strength in terms of molecular properties is extremely complicated. It involves the solution of the quantum mechanical wave equation employing an appropriate internuclear potential. Once the wave functions are obtained, they, along with an experimentally determined dipole moment expansion, are used to form the dipole moment matrix. The dipole moment matrix is, in turn, related to the line strength by means of the Einstein transition probabilities or, alternatively, the oscillator strength. These operations are outlined in Penner[43] for general diatomic transitions. They have been performed, for the HF molecule, by Meredith and Kent[20] who employed the HF data of Lovell and Herget[48] and two assumed molecular models: the anharmonic oscillator and the Morse oscillator. The line strengths are calculated for temperatures between 273 ^{o}K and 5000 ^{o}K for several vibrational bands including the fundamental. The prior existence of these calculations was one determining factor in the choice of HF as a tracer absorbing gas.

Whereas the line strength, in the present units, is a function of temperature only, what is measured is the product, pS. More than one independent datum is therefore required for p and T determination. The ratio of two pS's for different rotational lines within a band is independent of p and offers one alternative for temperature determination. There are also situations in which temperature is relatively uninfluential. In order to specify these situations, the behavior of line strength with respect to temperature is developed below.

We express S in terms of the non-dimensional oscillator strength, following Penner[43]. .

$$S_{\ell u} = \frac{\pi \epsilon^2}{mc^2} \frac{N_\ell}{p} f_{\ell u} (1 - e^{-hc\nu/kT}) \qquad (99)$$

where $\frac{\pi \epsilon^2}{mc^2} = 8.83 \times 10^{-13}$ cm

N_ℓ = number density in lower energy state (cm^{-3})

$f_{\ell u}$ = absorption oscillator strength

ν = frequency of transition, $\ell \rightarrow u$, in wavenumbers

The exponential factor accounts for stimulated emission which, at the wavenumbers (~ 4000 cm^{-1}) and temperatures (300 ^{o}K) of initial interest, is negligible. For systems in local thermodynamic equilibrium, the population distribution among energy states is given by[49]

$$N_\ell = N \frac{g_\ell}{Q_\ell} e^{-E_\ell/kT} \tag{100}$$

where $N = \sum_\ell N_\ell$, total density

g_ℓ = statistical weight of lower state

$Q_\ell = \sum_\ell g_\ell e^{-E_\ell/kT}$, partition function

E_ℓ = lower state energy

The transitions which characterize the fundamental vibration-rotation absorption band of HF are those in which the vibrational quantum number, J, changes by ± 1. It is the R-branch, corresponding to the transition $J \rightarrow J + 1$, which lies within the atmospheric window of Fig. 3. The energy corresponding to each non-interacting mode is given by

$$E_v = h\, c\, \omega_e \left(v + \frac{1}{2}\right) \tag{101}$$

and

$$E_J = h\, c\, B_e\, J(J + 1) \tag{102}$$

where the notation is that of Herzberg[50].

The statistical weight of each rotational state is, in the absence of strong magnetic fields, $g_J = 2J + 1$ while each vibrational state exhibits energy equipartition, $g_v = 1$. The partition function may then be computed approximately by[50]

$$Q_{vJ} \simeq Q_v Q_J \simeq \frac{e^{-\frac{1}{2}\omega_e h c/kT}}{1 - e^{-\omega_e h c/kT}} \cdot \frac{kT}{h c B_e} \tag{103}$$

In summing the oscillator strength over the degenerate magnetic rotation states[43], $f_{\ell u}$ becomes $2(J + 1) f_J$ for R-branch transitions. Moreover, at the moderate temperatures of interest, the overwhelming majority of molecules occupy the vibrational ground state, $v = 0$. With these approximations, the line strength may be expressed

$$S_J = \frac{\pi \epsilon^2}{mc^2} \frac{N_J}{p} \frac{2(J + 1)}{2J + 1} f_J \tag{104}$$

A measurement of $p S_J (r)$ therefore corresponds to $N_J(r)$. This measurement coupled with the population distribution formula (Eq. (100)) provides a well established means of determining temperature. The $\ell n (N_J/2J + 1)$, when plotted versus E_J, is a straight line of slope $- 1/kT$. For accurate temperature determination, many lines, well separated in J, should be measured. At low temperatures where higher levels are sparsely populated, this may not be practical. We seek further simplification.

Eliminating N_J from Eq. (104) and incorporating the perfect gas law, $p = N\,kT/(1.013 \times 10^6)$ results in

$$S_J = 1.013 \times 10^6 \frac{\pi\epsilon^2}{mc^2} 2(J+1) f_J \frac{hcB_e}{(kT)^2} e^{-hcB_e J(J+1)/kT} \qquad (105)$$

A form of this expression was used to solve for the oscillator strength from the published line strengths of Meredith and Kent. The resulting oscillator strengths were then employed to extend the line strength calculations to temperatures lower than 273°K; temperatures which would be encountered in a supersonic free jet whose stagnation temperature is 300°K. The results of these calculations for several rotational R-branch lines are shown in Fig. 28 of Appendix C. In these calculations, a low temperature correction to Q_J was employed[49]

$$Q_J = \frac{kT}{hcB_e}\left[1 + \frac{1}{3}\frac{hcB_e}{kT} + \ldots\right] \qquad (106)$$

The line positions[20] and oscillator strengths of the first nine R-branch lines of HF are tabulated in Table 2 below.

The Lorentz line contour formula (Eq. (90)) can be derived by considering a dipole oscillator whose oscillation is randomly interrupted by collision. This random interruption results in a Fourier spreading of the oscillation frequency power spectrum about the most probable frequency, ν_m. The half width of this dispersion contour is related to

Table 2. Line Positions and Effective Oscillator Strengths for the R-Branch of the HF Fundamental Vibration-Rotation Band

J	ν (cm^{-1})	$\lambda(\mu)$	$f_J \times 10^6$
0	4001.150	2.4993	8.13
1	4039.121	2.4758	7.78
2	4075.447	2.4537	7.50
3	4110.084	2.4330	7.23
4	4142.987	2.4137	6.97
5	4147.111	2.3957	6.79
6	4203.417	2.3790	6.63
7	4230.866	2.3635	6.52
8	4256.420	2.3494	6.43

the mean time, τ, between collisions such that[51, 38]

$$b = \frac{1}{2\pi c \tau} \tag{107}$$

Further specification of $b(\tau)$ depends on the assumed collision model. In this regard, the relative orientation of the collision partners, the form of the intermolecular force field, and the assumed quantum number changes during collision all enter into the determination which is by no means complete at this time[52, 53]. Whereas the classical billiard ball collision approximation has found wide engineering acceptance, the resonant dipole-billiard ball (RDBB) approximation of Benedict et al.[52] is far superior for low quantum number, J. The RDBB approximation has been applied to the HF molecule by Simmons[19] whose calculations have

been herein extended to lower temperature by means of the equation

$$b = b_o \frac{p_e}{p_o} \sqrt{\frac{T_o}{T}} \left\{ 1 + f_1 (J, T) \left[\frac{c_o}{b_o} \sqrt{\frac{T_o}{T}} - 1 \right] \right\} \qquad (108)$$

where

$p_e = \sum_s \alpha_s p_s$, effective broadening pressure

α_s = broadening effectiveness of species s

$f_1(J, T) = \left[\sum_{J-1}^{J+2} (2J + 1)\, e^{- h c B_e J(J + 1)/kT} \right] Q_J^{-1}$, the state population factor for R-branch transitions

$c_o = .675\ cm^{-1}\ atm^{-1}$

It is seen that b depends not only on T and p_{HF} but also on the pressure and broadening effectiveness of the collision partners. For self-broadening, the collisional half-width is shown as a function of temperature in Fig. 29. Note that for large J or T, b is fairly well approximated by the billiard ball approximation.

Having expressions for b (p_e, J, T) and S_J (p, T), we are now in a position to evaluate, thermodynamically, the strong and weak line measurements, p S_J (r) and b p S_J (r). The possible methods of data reduction and interpretation are described below.

E. DATA REDUCTION

Measured absorptance may be related to actual absorptance by means of the linear integral transform

$$\bar{a}_{\nu} \Delta\nu = \int g(\nu - \nu_m)\, a_{\nu_m}\, d\nu_m \tag{109}$$

where $g(\nu - \nu_m)$ is the monochromator slit function (Appendix D) defined such that its integral is the spectral slit width, $\Delta\nu$. If, as in the present case, $\Delta\nu \gg b$, then for an isolated line

$$\bar{a}_{\nu} \Delta\nu \simeq g(\nu - \nu_m) \int a_{\nu_m}\, d\nu_m \tag{110}$$

$$= g(\nu - \nu_m)\, W_{\nu}$$

which at $\nu = \nu_m$ (line center) shows

$$\bar{a}_{\nu_m} = \frac{W_{\nu}}{\Delta\nu} \quad ; \quad g(0) \equiv 1 \tag{111}$$

Thus, the peak measured absorptance is proportional to the equivalent width and increases with decreasing $\Delta\nu$. This, of course, is true as long as $\bar{a}_{\nu_m} < 1.0$ and it provides the rationale behind one mode of data gathering. This mode involves setting the monochromator on ν_m and spatially scanning the jet in the y direction.

From Eq. (110), the integrated absorptance is seen to be

$$\overline{W_\nu} = \int \bar{a}_\nu \, d\nu = \frac{W_\nu}{\Delta\nu} \int g(\nu - \nu_m) \, d\nu = W_\nu \qquad (112)$$

showing that actual and measured equivalent widths are indeed identical. An alternative mode of data gathering then involves spectrally scanning several lines while remaining at one y position. The former mode is to be preferred as it yields smoother, faster spatial information and it is employed whenever the line center is not fully absorbed.

E.1. Radial Variation of Number Density and Partial Pressure in the Weak Line Approximation

We inquire whether there are conditions, based on the thermodynamic behavior of $p\,S_J$, wherein temperature may be a relatively unimportant factor in the weak line approximation. To see this, we investigate the normalized temperature variation of $p\,S_J$ in the following manner. From Eq. (105), we see that a line's strength, provided $J \neq 0$, exhibits a single maximum as a function of temperature. In the neighborhood of this maximum, its variation with temperature is a minimum. If the anticipated radial variation of temperature is small compared to the "width" of this maximum, then the measurement, $p\,S_J(r)$, will heavily reflect the single variation, $p(r)$. Similarly, through the use of the perfect gas law, $p\,S_J$ may be recast in terms of N and T alone. In this case, the maximum of the temperature

dependence, for particular line, occurs at a different temperature or, for a particular temperature range, a different line's strength is maximized. Judicious choice of lines should then, within specified tolerance, reflect the radial variation of N or p alone. The respective temperature variations which correspond to these two cases are normalized with respect to their peak value, obtained by differentiation with respect to temperature. This normalization allows determination of the temperature range over which the line strength varies less than a specified percentage.

From Eq. (105), the HF number density profile may be expressed

$$N(r)\,\mathcal{F}_N\left[J, T(r)\right] = 1.54 \times 10^{12}\,\frac{J}{f_J}\,p\,S_J(r) \tag{113}$$

where

$$\mathcal{F}_N(J, T) = \frac{e\,h\,c\,B_e\,J(J+1)}{kT}\,e^{-h\,c\,B_e\,J(J+1)/kT} \tag{114}$$

is the normalized temperature dependence of $p\,S_J(N, T)$. For HF, the groupings of constants have the following values[50]: $e\,h\,c\,B_e/k = 82.36^{\circ}K$ and $h\,c\,B_e/k = 30.3^{\circ}K$. The temperature which maximizes $\mathcal{F}_N$ is given by

$$T_N = \frac{h\,c\,B_e\,J(J+1)}{k} = 30.3\,J(J+1) \tag{115}$$

In analogous fashion, the HF partial pressure profile may be written

$$p(r)\,\mathcal{F}_p\left[J, T(r)\right] = 4.31 \times 10^{-9}\,\frac{J^2(J+1)}{f_J}\,p\,S_J(r) \qquad (116)$$

where

$$\mathcal{F}_p(J, T) = \left[\frac{e\,h\,c\,B_e\,J(J+1)}{2kT}\right]^2 e^{-h\,c\,B_e\,J(J+1)/kT} \qquad (117)$$

is the normalized temperature dependence of $p\,S_J(p, T)$. The temperature at which $\mathcal{F}_p$ is maximized is half that which maximizes $\mathcal{F}_N$, i.e.

$$T_p = \frac{h\,c\,B_e\,J(J+1)}{2k} = 15.15\,J(J+1) \qquad (118)$$

In the neighborhood of $T_N(J)$, the approximation $\mathcal{F}_N \simeq 1$ is used for interpretation of the data, $p\,S_J(r)$. Another line, J', is chosen such that $T_p(J')$ allows use of the approximation $\mathcal{F}_p \simeq 1$ in the same expected temperature range. The temperature functions, for use with inverted weak line data, $p\,S_J(r)$, are shown in Fig. 30 and 31. From the figures, it is seen that for $T = O(300^{\circ}K)$, the lines $J = 3$ and $J' = 4$ would be primarily sensitive to N(r) and p(r) respectively.

E. 2. Radial Variation of Number Density and Partial Pressure in the Strong Line Approximation: Self-Broadened Line Width-Billiard Ball Collisions

When the absorption data may be interpreted according to the strong line approximation, the inverted data may be cast into the triple product, $b\ p\ S_J(r)$. In the self broadened, billiard ball collision approximation for the Lorentz line width, b, the product, $b\ p\ S_J(r)$, may be recast in terms of either N, T or p, T in the same manner as in the previous, weak line, development. From Eq. (105), (94), the radial variation of HF number density may be written

$$N^2(r)\mathcal{J}_N\left[J, T(r)\right] = 1.012 \times 10^{33} \sqrt{\frac{J}{J+1}} \frac{1}{f_J} b\ p\ S_J(r) \qquad (119)$$

where

$$\mathcal{J}_N(J, T) = \sqrt{\frac{2\ e\ h\ c\ B_e\ J(J+1)}{kT}}\ e^{-h\ c\ B_e\ J(J+1)/kT} \qquad (120)$$

is the normalized temperature dependence of $b\ p\ S_J(N, T)$, maximized at a temperature of

$$T_N = \frac{2\ h\ c\ B_e\ J(J+1)}{k} = 60.6\ J(J+1) \qquad (121)$$

The radial variation of HF partial pressure is, similarly,

$$p^2(r)\mathcal{J}_p\left[J, T(r)\right] = 8.39 \times 10^{-9} \frac{J^{5/2}\ (J+1)^{3/2}}{f_J} b\ p\ S_J(r) \qquad (122)$$

where

$$\mathcal{J}_p(J, T) = \left[\frac{2\, e\, h\, c\, B_e}{5kT} J(J+1)\right]^{5/2} e^{-h\, c\, B_e\, J(J+1)/kT} \qquad (123)$$

is the normalized temperature variation of $b\, p\, S_J(p, T)$ maximized at a temperature of

$$T_p = \frac{2}{5}\frac{h\, c\, B_e}{k} J(J+1) = 12.12\, J(J+1) \qquad (124)$$

The functions $\mathcal{J}_N(J, T)$ and $\mathcal{J}_p(J, T)$ are shown in Fig. 32 and 33.

E. 3. Temperature Determination by Means of the Ratios $S_J/S_{J'}$ and $b\, p\, S_J/b\, p\, S_{J'}$

Since the data $p\, S_J(r)$ is linear in p, the ratio, $p\, S_J(r)/p\, S_{J'}(r)$, is dependent only on temperature. The logarithm of this ratio for the two lines J and J' is

$$\ell n \frac{p\, S_J}{p\, S_{J'}} = \ell n \frac{f_J(J+1)}{f_{J'}(J'+1)} - \frac{h\, c\, B_e}{kT}\left[J(J+1) - J'(J'+1)\right] \qquad (125)$$

Plotted on semi-log paper with 1/T as abscissa, this ratio is a straight line of slope

$$-\frac{h\, c\, B_e}{k}\left[J(J+1) - J'(J'+1)\right] \qquad (126)$$

Thus, a measurement of the ratio as a function of r would allow temperature profile determination. There is no loss of generality if it is specified that $J' < J$ always. In this way, the slope of each curve is always negative and increases with the separation, $|J - J'|$. Figures

34-37 are curves of the ratio $S_J/S_{J'}$ for the first five lines of the HF fundamental vibration-rotation band's R-branch. In the self-broadened billiard-ball collision approximation, the ratio b p S_J/b p $S_{J'}$ equals $S_J/S_{J'}$ so that both strong and weak line data are interpretable in terms of temperature from these graphs.

For self broadening in the resonant dipole billiard ball approximation, corresponding curves of the now irreducible ratio, b(J) S_J/b(J') $S_{J'}$ may be formed by combining the calculations of Fig. 28 and 29. The results of this operation are shown in Fig. 38-41 for the first five lines of the HF R-branch.

Inspection of the figures illustrates the necessity of utilizing ratios of two lines widely separated in J. It is seen that small separation in J amplifies an error in the ordinate whereas the steeper-sloped curves pertaining to large J - J' lead to reduced spread along the abscissa, 1/T.

There are other temperature functions and ratios which could be formed depending on approximations to the effective broadening pressure, p_e, for the situation wherein foreign gas broadening is significant. An example of such an approximation would be, in the case of subsonic free jet mixing, $p_e \simeq \alpha_{air} p_{air} \simeq \alpha_{air}$ if the HF constituted a minor fraction of the total mixture. Which line broadening model is most accurate is best determined by experiment in any case.

E. 4. Determination of Centerline Values $pS_J(0)$ or $bpS_J(0)$

The two Abel transform pairs, $pS_J(r) \Longleftrightarrow W_\nu(y)$ and $bpS_J(r) \Longleftrightarrow W_\nu^2(y)/4$ are appropriate to weak and strong line absorption respectively. It will be shown here that either centerline value of the radial distributions may be obtained without actually performing a numerical Abel inversion. Our approach is motivated by the scattering transform pair, $K_\lambda(r) \Longleftrightarrow -\ln\left[1 - a_\lambda(y)\right]$, which is further reducible by partial integration. We will restrict the analysis to weak line absorption since its strong line counterpart is similar.

Let the transverse data be expressed

$$W_\nu(y) = -\ln\left[1 - X(y)\right] \tag{127}$$

such that $X(y)$ is a new y-dependent variable.

From the formal definition of the inverse Abel transform[32]

$$pS_J(0) = \frac{-1}{\pi} \int_0^\infty \frac{d}{dy} \ln\left[1 - X(y)\right] \frac{dy}{y} = \frac{1}{\pi} \int_0^{X(0)} \frac{dX}{y(1 - X)} \tag{128}$$

This integral may be computed graphically as shown below.

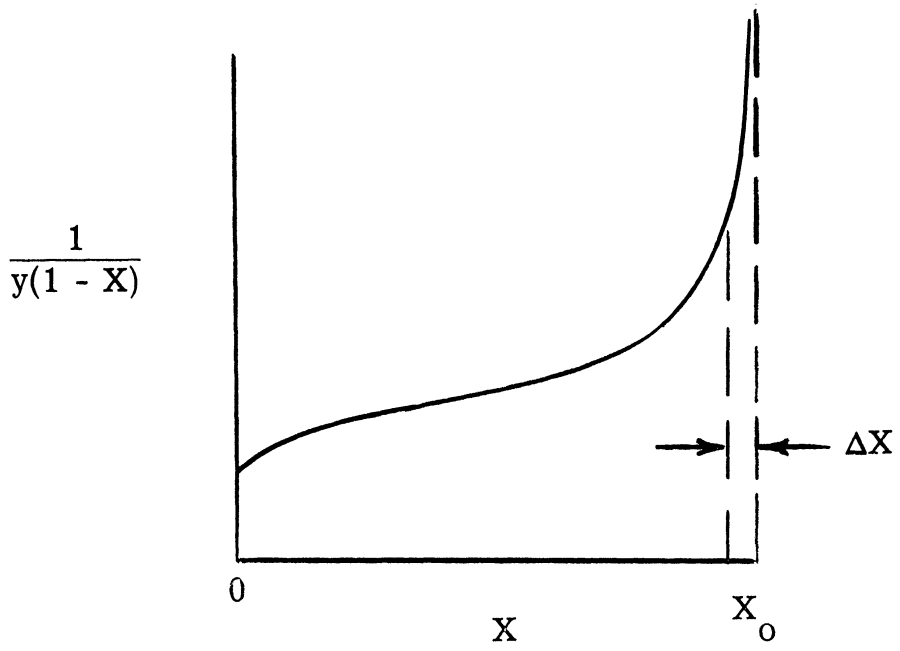

The integrand diverges due to the presence of y in the denominator but the integral can be evaluated with arbitrary accuracy since 1 - X(y) is slowly varying near y = 0.

Since the entire area under the curve $y^{-1}(1 - X)^{-1}$ can never be obtained graphically, it is important to compute the error incurred by evaluating only the incomplete integral

$$pS_J^{\dagger}(0) = \frac{1}{\pi} \int_0^{X(0)-\Delta X} \frac{dX}{y(1 - X)} \tag{129}$$

A reasonable analytic profile for W(y) is assumed to be the normal curve

$$W(y) = W_o e^{-\ln 2 \left(\frac{y}{y_W}\right)^2} \tag{130}$$

where $W_o = W(0)$ and y_W is the half-width at half-height of the equivalent width profile. The subscript ν has been omitted in this development. From the relations of Section IV-C. 3, it follows that

$$pS_J(r) = pS_J(0)\, e^{-\ln 2 \left(\frac{r}{y_W}\right)^2} \tag{131}$$

since $r_W = y_W$ and

$$pS_J(0) = \sqrt{\frac{\ln 2}{\pi}}\, \frac{W_o}{y_W} \tag{132}$$

i. e., the complete integral, $pS_J(0)$, is a simple function of the peak (centerline) equivalent width and the breadth of the transverse profile. The incomplete integral, $pS_J^{\dagger}(0)$, may be expressed in closed form by means of the incomplete gamma function. This is shown as follows:

$$pS_J^{\dagger}(0) = \frac{\sqrt{\ln 2}}{\pi y_W} \int_0^{X_o - \Delta X} \frac{dX}{(1 - X)\sqrt{-\ln\left[\frac{\ln(1 - X)}{\ln(1 - X_o)}\right]}}$$

$$= \frac{\sqrt{\ln 2}}{\pi y_W} \int_0^{-\ln\left[1-(X_o - \Delta X)\right]} \frac{dW}{\sqrt{-\ln \frac{W}{W_o}}} \tag{133}$$

$$= \frac{pS_J(0)}{\sqrt{\pi}} \int_0^{\ln\left[1-(X_o - \Delta X)\right]/\ln(1-X_o)} \frac{d\eta}{\sqrt{-\ln \eta}}$$

where $X_o = X(0)$ and $\eta = \frac{W}{W_o}$. Setting $\xi = -\ln \eta$ yields

$$\frac{pS_J^{\dagger}(0)}{pS_J(0)} = \frac{1}{\sqrt{\pi}} \int_{\xi(X_o, \Delta X)}^{\infty} \xi^{-1/2} e^{-\xi} \, d\xi = \frac{1}{\sqrt{\pi}} \Gamma\left[\frac{1}{2}, \xi(X_o, \Delta X)\right] \quad , \quad (134)$$

the incomplete gamma function where

$$\xi(X_o, \Delta X) = -\ln\left\{\frac{\ln\left[1 - (X_o - \Delta X)\right]}{\ln(1 - X_o)}\right\} \quad (135)$$

For $\Delta X = 0$, the lower limit of integration is zero and the value of the integral is $\Gamma(1/2) = \sqrt{\pi}$ such that $pS_J^{\dagger}(0) = pS_J(0)$.

What is the error incurred in truncating graphical integration when $\Delta X/X_o = .02$, an easily achieved proximity to the upper limit? As an example, we take $X_o = .0328$, a typical value which has been experimentally obtained. In this case, the lower limit of Eq. (134) is 0.00068. Expressing $\Gamma\left[\frac{1}{2}, \xi(X_o, \Delta X)\right]$ in terms of confluent hypergeometric functions, it may be shown that for small $\xi(X_o, \Delta X)$, the following asymptotic expansion is appropriate[74]

$$\frac{pS_J^{\dagger}(0)}{pS_J(0)} \simeq e^{-\xi(X_o, \Delta X)} \simeq 1 - .00068 \; ; \quad (135)$$

an error of less than 0.07% for the stated conditions.

SECTION VI

CONCLUSIONS

An experimental facility capable of non-interferring diagnosis of axisymmetric mixing phenomena has been developed. Utilizing either light scattering or absorption spectroscopy, the mixing of liquid or gaseous fuel with air may be studied. The light scattering technique has been applied to the supersonic coaxial mixing of water with air. It was determined that the droplet size distribution, formed by strong aerodynamic shear forces at the injection plane, is practically a delta function, i.e., particles of almost uniform size are created by the shearing mechanism. The density of these particles was determined as a function of spatial coordinates by means of the Abel transformation. Regions of similarity behavior of density profiles were found wherein certain integral radii exhibited power law behavior. The mixing rate in the farthest downstream region measured is faster than its subsonic counterpart. The centerline density decay also exhibited power law behavior in two regions; the exponents, - 5/3 and - 7/3, lying on either side of a commonly accepted value of two. It was shown that centerline values and radial expansion rates may be obtained without Abel transformation.

A molecular absorption technique, utilizing hydrogen fluoride as a tracer molecule, has been developed to the point where subsonic data runs have been obtained. Difficulties in efficiently handling and injecting this corrosive substance have been effectively overcome. In the process, a unique measurement of the viscosity of HF has been obtained. The difficult task of interpreting absorption data in terms of thermodynamic and molecular variables has been attacked by developing several engineering approximations to the point where the data will determine the most useful data reduction schemes.

APPENDIX A

MEASUREMENT OF HF MASS FLOW RATE

An orifice differential pressure flowmeter was chosen as the device to measure HF flow rate. Constructed of monel with interchangeable orifice disks, this meter is a compromise between the relatively expensive venturi meter and the inefficient choked orifice meter. An additional, unforeseen, benefit accrues from the orifice's Reynolds number sensitivity. Because of this sensitivity, the viscosity of HF may be inferred from measurements of mass flow rate and integrated mass flow. Although the viscosity of liquid HF and calculations of the viscosity for gaseous HF have been reported in the literature[54], there does not seem to be any reported gaseous measurement. Moreover, the calculated values reported do not take into account polar molecule behavior nor phase change.

The orifice design follows that of the British Standards Institution in that corner differential pressure tap locations are employed. These are the only taps which allow different sized orifii to be compared on a Reynolds number basis[55]. Otherwise, tap locations would have to be moved to conform to the particular orifice or pipe diameter.

The mass flow rate of fluid through a square edged orifice is given by[56]

$$\dot{m} = \frac{CY}{\sqrt{1 - \beta^4}} A \sqrt{2\rho\Delta p} \qquad (A\text{-}1)$$

which is derived from the one dimensional incompressible Bernoulli equation. It is corrected for compressibility, area change, and frictional losses by the factors Y, $\sqrt{1 - \beta^4}$ and C, respectively.

For flow of a perfect gas, the orifice flow equation may be written

$$\dot{m} = 0.204\, A \frac{CY}{\sqrt{1 - \beta^4}} \sqrt{\mathcal{M} p \Delta p / T} \qquad (A\text{-}2)$$

where

$\dot{m}$ = mass flow rate, lb/sec

A = orifice area, sq in.

C = orifice discharge coefficient

Y = compressibility factor

β = orifice dia/pipe dia

$\mathcal{M}$ = molecular weight of gas

p = static pressure upstream of orifice, psia

Δp = pressure differential across orifice, psid

T = static temperature of gas upstream of orifice, ^{o}R

It was not known, a priori, the amount of HF mass required for the absorption measurements nor was it known what steady mass flow could be maintained by the injection system. It was known that a desirable

operating Δp would be in the neighborhood of 1 psid. This value could be accurately measured and the stream would not suffer a significant ultimate pressure loss as a result. For these reasons, three orifii were constructed and calibrated using a rotameter of known calibration and nitrogen as the working fluid.

As a result of this procedure, the orifice discharge coefficient, for all orifii, was determined to have a power law Reynolds number dependence given by,

$$C = 3.8\ Re^{-1/6} \tag{A-3}$$

valid in the range $6000 < Re < 25000$.

In pipe flow, the Reynolds number may be expressed in terms of the mass flow rate, pipe diameter, D, and viscosity coefficient, μ.

$$Re = 4\dot{m}/\pi D \mu \tag{A-4}$$

When the Reynolds number dependence of C is introduced into the orifice equation, the square root dependence is replaced by

$$\dot{m} \sim Y^{6/7}\ \mu^{1/7}\ (p\Delta p)^{3/7} \tag{A-5}$$

Here, it has been assumed that temperature does not vary significantly during a flow period. A $\pm 10^{\circ}R$ variation about an assumed value of $550^{\circ}R$ produces, at most, an error of 1.5% in $\dot{m}$. The maximum temperature variation recorded during a run was always less than $10^{\circ}R$. A temperature of $550^{\circ}R$ is therefore assumed.

An orifice with A = .013 sq in., β = .426, produced the required pressure differential. Introducing $\mathcal{M}$ = 20.01 and setting the compressibility factor, $Y^{6/7} \sim 1$, the HF mass flow becomes

$$\dot{m} = 4.38 \times 10^{-3} \mu^{1/7} (p\Delta p)^{3/7} \tag{A-6}$$

Since viscosity is a weak function of temperature and since temperature does not vary by more than 4% during a run, the ratio of instantaneous mass flow rate to initial flow rate may be written

$$\frac{\dot{m}}{\dot{m}_o} = \frac{(p\Delta p)^{3/7}}{(p\Delta p)_o^{3/7}} \tag{A-7}$$

Integrating over the duration of flow, the total mass, m, evaporated is obtained.

$$m = \dot{m}_o \int_0^t \frac{(p\Delta p)^{3/7}}{(p\Delta p)_o^{3/7}} \, dt \tag{A-8}$$

The ratio in the integrand may be measured and the integral evaluated graphically. The total mass used is obtained by weighing the HF cylinder before and after the run. Thus the initial flow rate $\dot{m}_o$ may be determined. Knowing $\dot{m}_o$, $\dot{m}(t)$ and $\mu_{HF}^{1/7}$ may also be obtained.

This procedure has been applied to two runs in which $\dot{m}$ varied significantly during a run. In addition to plotting $(p\Delta p)^{3/7}$ versus t, the square root (constant C) dependence was also plotted and the average mass flow rate, m/t, compared to the average for each curve. In this way, it was determined that the 3/7-power ratio is indeed the correctly shaped curve. Had $\dot{m}$ not varied with t, this comparison would not have been determinate. This comparison indicates that the Reynolds number for the HF flow lies within the range of the N_2 calibration.

The two values of $\mu^{1/7}$, thus far determined, vary by 2.4%. The absolute values of μ therefore vary by 18% due to the power amplification. We have

$$7.8 \times 10^{-7} \leq \mu_{HF} (550^{\circ}R) \leq 9.5 \times 10^{-7} \text{ lb sec/ft}^2$$

which compares favorably with μ calculated assuming rigid non polar sphere molecules. The value reported in Ref. 54, using the Leonard Jones potential but again not corrected for polar behavior, is 2.6×10^{-7} lb sec/ft^2 at this temperature.

APPENDIX B

SCATTERING-AREA COEFFICIENT, K_s

Crucial to the analysis of light scattering by aerosols is the specification of the scattering area coefficient. This coefficient is essentially a measure of the efficiency with which a single particle scatters radiation in a given direction. It is dependent upon: the refractive index of both the particle and the surrounding medium, particle shape, illuminating wavelength, the scattering angle with respect to the direction of the incident light wave, and the polarization of the incident wave. Additional dependences arise when one deals with an agglomeration of particles. In this case, the particle size distribution and the mean particle separation require specification. Fortunately, many of these dependences are ignorable in many situations. This appendix deals with the mathematical formulation of the scattering area coefficient and its simplification in the present experimental configuration.

In what follows, attention will be focussed solely on the attenuation due to scattering of a plane-parallel beam of monochromatic unpolarized radiation traversing an ensemble of spherical water particles suspended in air. The weakening of the beam will be due to the scattering of incident energy into all directions except the forward direction. It has been shown[29] that forwardly scattered energy will be insignificant provided the detection optics subtend a sufficiently narrow solid angle. This

criterion is adequately met in the present situation (f/12 optics). Furthermore, it is assumed that energy, once scattered, does not suffer another collision within the scattering medium. This single-scattering restriction is obeyed if the mean particle separation distance is at least several wavelengths large[31] . To compute this, one notes that the distance of the nearest neighbor is approximately $N^{-1/3}$ where N is the particle density. For the number density presently measured, this distance is at least 20 wavelengths for all wavelengths employed. Under these relatively mild restrictions, the scattering area coefficient becomes mainly a function of the particle size distribution function, $\phi(D)$, and the scattering parameter, $\alpha = \pi D/\lambda$. The scattering area coefficient for a single particle or agglomeration of uniformly-sized particles (monodisperse) will be discussed first. Then the modification required to describe an agglomeration of many-sized particles (polydisperse) will complete the present discussion.

In general, the mathematical formulation of $K_s(\alpha)$ is extremely complex. There are two limiting cases, however, for which $K_s(\alpha)$ may be expressed in a simple closed analytical form. They apply whenever $\alpha \lesssim .5$ (Rayleigh limit) or whenever $\alpha \gtrsim 50$ (geometrical optics limit). The K_s expression for Rayleigh scattering by particles with refractive index n in air is given by[33]

$$K_s = \frac{8}{3}\left(\frac{n^2 - 1}{n^2 + 2}\right)^2 \alpha^4 \qquad (\lambda \gg D) \qquad \text{(B-1)}$$

The refractive index for water is 1.33 whereas that for ice is 1.30.

On the other hand, K_s in the geometrical optics limit is given by

$$K_s = 2 \qquad (\lambda \ll D) \qquad \text{(B-2)}$$

At first it may appear strange that the optical cross-section is twice the geometric cross section. The reason, as explained by Van de Hulst, is that light diffracted around the edge of a particle is equal to that which is scattered by reflection and refraction. Thus it is seen that, in the geometrical optics limit, K_s is independent of particle size and hence the overall scattering coefficient, K_λ, depends only on two quantities: the number density, N, and the average particle area, D^2. In theory, therefore, only two independent measurements are required for complete determination of N and D for a monodisperse medium.

The scattering in the intermediate range is termed Mie scattering and is characterized by successive major maxima and minima. Analytically specifying K_s in this region involves infinite series of Legendre polynomials and spherical Bessel functions[31]. Fortunately, extensive tables[57] are available for the determination of $K_s(\alpha;n)$. The curve for water in air, taken from Ref. 31, is shown in Fig. 23. Minor fluctuations in this curve have been smoothed by the author

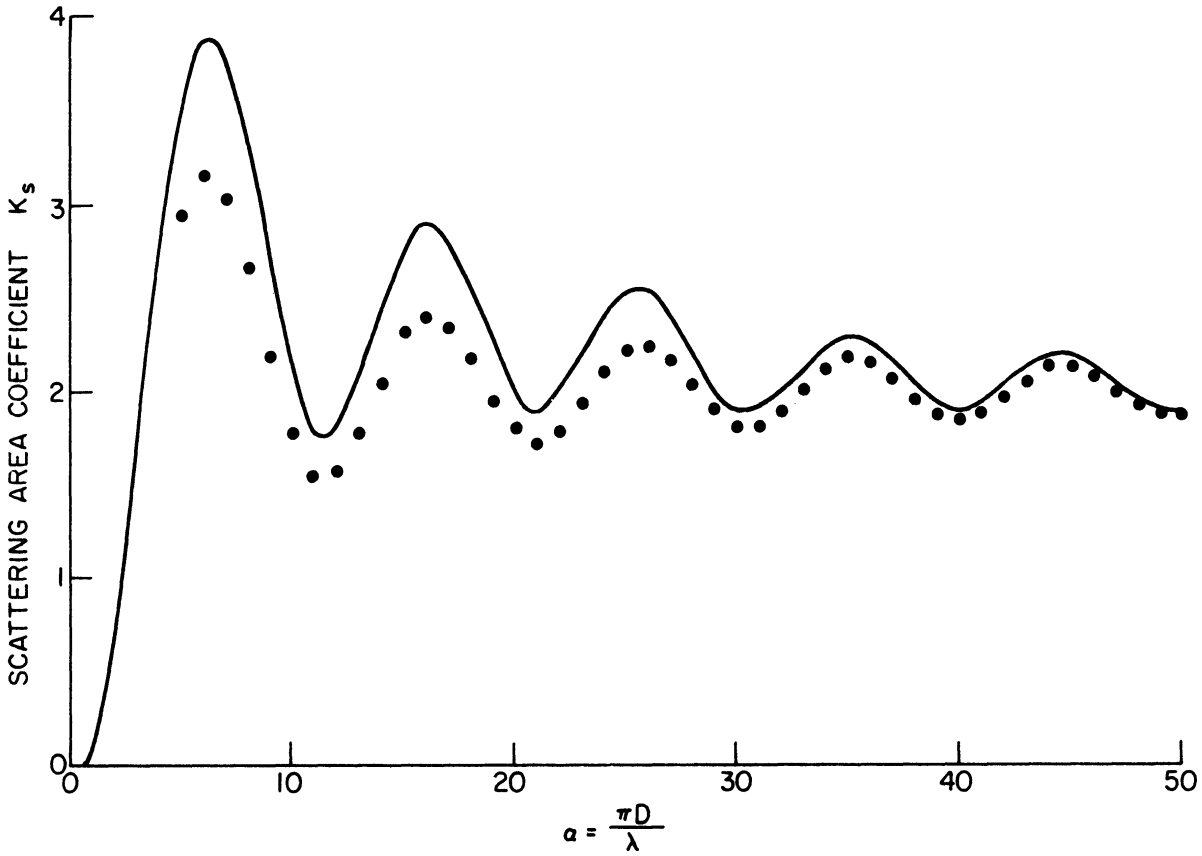

Figure 23. Scattering Area Coefficient versus Scattering Parameter for Water Droplets in Air. Points Indicate Approximation, Eq. (B-3).

because there will always be sufficient spread in particle size to completely mask them. The points also shown in the figure correspond to an approximate form[33] good for small n - 1 and large α. The period is adequately represented for all α, however. This approximation is given by

$$K_s \simeq 2 - \frac{6}{\alpha} \sin \frac{2}{3}\alpha + \frac{9}{\alpha^2}(1 - \cos \frac{2}{3}\alpha) \qquad \text{(B-3)}$$

for water in air.

In a polydisperse situation, the K_s for each particle must be appropriately summed over all particles to yield an agglomerate average value. This is accomplished via the introduction of a particle distribution function, $\phi(D)$, which specifies the fraction of particles with sizes between D and D + dD, i.e.,

$$\phi(D)\, dD \equiv \frac{N(D)}{N}\, dD \qquad \text{(B-4)}$$

and

$$\int_0^\infty \phi(D)\, dD = 1 \qquad \text{(B-5)}$$

The first moment of the particle distribution function is the particle-average diameter;

$$\overline{D} \equiv \int_0^\infty D\phi(D)\, dD \tag{B-6}$$

Similarly, the second and third moments are the particle-average area and volume respectively;

$$\overline{D^2} \equiv \int_0^\infty D^2\, \phi(D)\, dD \tag{B-7}$$

$$\overline{D^3} \equiv \int_0^\infty D^3\, \phi(D)\, dD \tag{B-8}$$

The scattering depends on $\overline{D^2}$ whereas the particle mass flow, one of the easily measured experimental quantities, depends on $\overline{D^3}$. A quantity which will therefore arise naturally during data reduction is the ratio

$$D_{32} \equiv \frac{\overline{D^3}}{\overline{D^2}} \tag{B-9}$$

Depending on the shape, and particularly on the width, of $\phi(D)$, D_{32} can range in size from $\overline{D}$ to many times $\overline{D}$. It will become apparent that D_{32} is the natural variable to plot the averaged scattering area coefficient against. Each curve will, of course, depend on $\phi(D)$.

In what follows, it is convenient to express D in terms of $\alpha = \pi D/\lambda$ such that, e.g.,

$$\alpha_{32} = \frac{\pi}{\lambda} D_{32} = \frac{\overline{\alpha^3}}{\overline{\alpha^2}} \tag{B-10}$$

and

$$\phi(\alpha)\, d\alpha \equiv \phi(D)\, dD \tag{B-11}$$

The overall scattering coefficient (extinction coefficient), K_λ, for a polydisperse medium is written [58]

$$K_\lambda (r, z) = \frac{\lambda^2}{4\pi} N(r, z) \int_0^\infty K_s(\alpha)\, \alpha^2\, \phi(\alpha)\, d\alpha \tag{B-12}$$

where, in general, $\phi(\alpha) = \phi[\alpha(r, z)]$. In terms of a particle average, this becomes

$$K_\lambda = \frac{\lambda^2}{4\pi} N \overline{K_s \alpha^2} \tag{B-13}$$

A particle-area weighted average, denoted by a double bar, may also be defined such that

$$K_\lambda = \frac{\lambda^2}{4\pi} N \overline{\overline{K_s}}\, \overline{\alpha^2} \tag{B-14}$$

where

$$\overline{\overline{K}}_S \equiv \frac{\int_0^\infty K_S \alpha^2 \phi(\alpha)\, d\alpha}{\int_0^\infty \alpha^2 \phi(\alpha)\, d\alpha} = \frac{\overline{K_S \alpha^2}}{\overline{\alpha^2}} \qquad \text{(B-15)}$$

The reason to distinguish between these two types of averages is apparent from Eq. (B-15). Use of a single bar average sign throughout would seem to imply K_S and α were statistically independent quantities which they are not.

Once $\phi(\alpha)$ is specified, $\overline{\overline{K}}_S$ may be computed numerically from Eq. (B-15) and plotted against any moment of α since they are all uniquely related to each other by Eq. (B-6) through (B-9). The method of data taking, however, dictates the use of α_{32} as the independent variable. For a monodisperse medium, $\phi(\alpha)$ is a delta function, $\delta(\alpha - \overline{\alpha})$, and all moments are simply powers of $\overline{\alpha}$, e.g., $\alpha_{32} = \overline{\alpha}^3/\overline{\alpha}^2 = \overline{\alpha}$. In this case $\overline{\overline{K}}_S(\alpha_{32})$ reduces to $K_S(\alpha)$. Widening the $\phi(\alpha)$ has the effect of smoothing the humps of Fig. 23 .

At this point, $\phi(\alpha)$ must be considered in more detail. Of particular interest is the prediction of the shape of $\phi(\alpha)$ based upon the mechanism of droplet formation. One would also like to determine the sensitivity of $\overline{\overline{K}}_S$ and α_{32} to the various parameters which describe physically probable distributions. The mechanism of droplet formation

in supersonic coaxial mixing of liquid water and air is the strong aerodynamic shear created at the nozzle exit. Here the outer air velocity is 600 meters/sec while the water core velocity is only 1 meter/sec. Particle size distribution measurements under these conditions have not, as yet, been made. Perhaps the measurements which most closely approximate the present situation are those of Nicholls et al [59,60] wherein the disintegration of large fuel droplets struck by a shock wave were studied photographically. In these experiments, the droplet initially elongated in the direction perpendicular to the flow. Small droplets, were then stripped from the edge of greatest curvature. The particle size distribution function could not be measured, however.

Particle size distributions have been measured for droplets formed by condensation [61,62] , . Here the process is the reverse of the present one. An initially vaporized substance condenses and may eventually solidify. The solid particles may then be collected and actually counted as a function of size. The resulting distribution function is characterized by a slightly skewed bell-shaped curve with half-width at half height, $\Delta\alpha$, a constant multiple of $\bar{\alpha}$ [61,62] . This constant, averaged over six experiments with varying $\bar{\alpha}$, is very nearly 0.33. In other words, the particle size distribution function for condensation processes, appears to be a two-parameter single-humped curve with similarity characteristics ($\Delta\alpha/\bar{\alpha} \simeq 1/3$).

Ingebo[63] has photographically measured the particle-size distribution of boom-injected sprays in low speed air (42 - 55 m/sec). Again a slightly-skewed single-humped curve ($\Delta\alpha/\bar{\alpha} \simeq .37$) was the result. Average particle sizes of the order of 40μ were measured.

Efforts to analytically specify the drop-size distribution have varied with the author. Ingebo states that the Nukiyama-Tamasawa distribution,

$$\phi(\alpha) \sim \frac{\alpha^5}{\left(\overline{\alpha^3}\right)^2} \exp\left[- \text{const} \frac{\alpha}{\left(\overline{\alpha^3}\right)^{1/3}} \right] \tag{B-16}$$

fits his data well except for the largest α. He also measures a maximum particle size which is a constant multiple of the mass-mean diameter, i.e.,

$$\alpha_{max} = 2.9 \left(\overline{\alpha^3}\right)^{1/3} \tag{B-17}$$

Mugele and Evans[34] have also perceived the necessity for an analytical form which admits of a maximum particle size. They propose a three-parameter distribution function which they call the Upper Limit Distribution Function (ULDF) given by

$$\phi(D) \sim \frac{\exp - \left\{ \delta \ln\left[aD/(D_\infty - D) \right] \right\}^2}{D^4 (D_\infty - D)} \tag{B-18}$$

where D_∞ is the maximum permitted particle diameter. Unfortunately, the parameters, δ and a, are not clearly related to a physically descriptive parameter such as ΔD or $\overline{D}$. In fact, this function is so complicated that a paper has been written on its behavior as a function of its parameters[64]. It is a single-humped (monomodal) curve which, with proper choice of a and δ, is biased toward larger sizes however.

Using the ULDF and the approximate expression (Eq. (B-3)) for K_s, Dobbins[33] has computed $\bar{\bar{K}}_s(\alpha_{32})$ and also the specific scattering coefficient, $\bar{\bar{K}}_s/\alpha_{32}$. He then compares the resulting curves with those generated by rectangular (top hat) and parabolic particle-size distribution functions of varying widths. From this study he concludes that $\bar{\bar{K}}_s$ and $\bar{\bar{K}}_s/\alpha_{32}$ are quite insensitive to the shape of $\phi(\alpha)$ and that the most significant parameter is the width, $\Delta\alpha$. He then computed $\bar{\bar{K}}_s$ for more accurate values of K_s using the ULDF with various width to mean diameter ratios. When $\Delta\alpha/\bar{\alpha}$ exceeds approximately 0.5 (his $w > 1$), all peaks except the first are effectively smoothed in $\bar{\bar{K}}_s$ or $\bar{\bar{K}}_s/\alpha_{32}$. The other parameter, $\bar{\alpha}/\alpha_\infty$, was held constant at 0.281. These calculations are valuable in establishing parametric trends insofar as sensitivity is concerned but their application to experimental particle size determination is not without ambiguity. At this point, more information is needed relating actual distributions to the three adjustable constants.

Dobbins [30, 65, 66] has applied light transmission techniques to the determination of $A\ell_2O_3$ particle size in solid propellant rocket nozzles. Whereas he measured no appreciable variation in D_{32} while the chamber pressure varied by an order of magnitude, Crowe and Willoughby [67, 68], using a tank collection technique measured a significant increase in D_{32} with increased chamber pressure. In Dobbins' initial light scattering tests, the path-integrated transmission loss was measured at two wavelengths and an assumed ULDF with large width was used in the data reduction. With such a large assumed width, it is reasonable to speculate that the determination of D_{32} would be insensitive to changes in position of the peak (the peak has relatively large radius of curvature).

In an effort to resolve this discrepancy, Dobbins and Strand [66], conducted further tests utilizing three wavelengths and tank collection techniques as well. It became apparent that the ULDF would have to be narrowed and, moreover, an additional hump added to account for large particles arising from nozzle erosion. The particle distribution function is now bimodal and requires a fourth and fifth parameter (the strength and position of a delta function) for its specification.

It is clear that, unless the particle distribution function is better known a priori, the application of scattering techniques to systems which have more than one particle generation mechanism (bimodal)

involves an uncomfortable number of parameters. Theoretically, however, sufficient independent data (e.g. n wavelengths) should completely specify $\phi(\alpha)$ regardless of its number of degrees of freedom.

For a number of reasons, the particle-size distribution function appropriate to the present series of experiments should be much simpler than the ones just mentioned. It is highly probable that it is monomodal because there is only one significant generation mechanism, the strong turbulent shear acting between the outer air and the initial liquid core. Kling[40] has also photographically measured particle-size distributions of sprays injected into moving air and concludes the following:

1. The particle-size distribution is monomodal.
2. The mean particle size is an inverse function of the air speed.
3. The particle-size distribution function becomes rapidly narrower with increasing air speed.
4. The influence of fuel/air ratio on mean particle size is diminished as air speed increases.
5. Once formed, the mean particle size remains essentially constant with respect to downstream distance in a non-combusting flow.

These conclusions were obtained for kerosene sprayed into air at subsonic velocities up to 200 msec. Figure 24, replotted on log-log paper from Ref. [40] shows the variation of surface-mean diameter, $\sqrt{\overline{D^2}}$, with respect to air velocity. These data have been extrapolated to encompass the present experimental conditions (u_a = 600 msec,

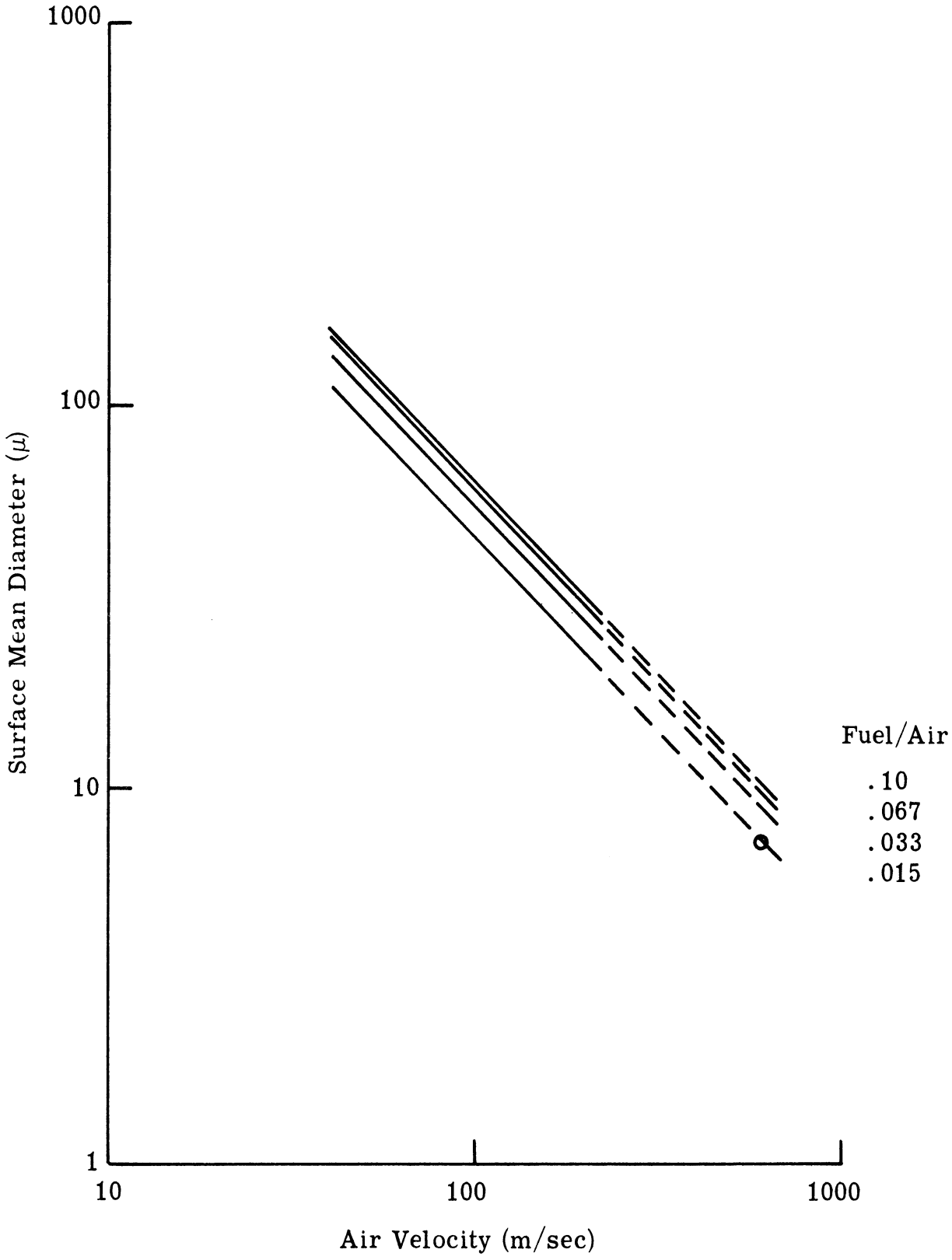

Figure 24. Surface Mean Diameter of Fuel Spray versus Relative Airstream Velocity with Fuel/Air Ratio as a Parameter

F/A = 1/66) by assuming $\sqrt{\overline{D^2}} \sim u_a^{-1}$ as suggested by the emperical correlation of Nukiyama and Tanasawa[41]. The mean diameter measured in the present experiment is seen to be in good agreement with this prediction. The increasing narrowness of $\phi(D)$ as air velocity is increased is evident in Fig. 25, replotted on probability paper from Ref. 40 The cumulative distribution, estimated for the present experiments, has been included for comparison. The reason for these trends is apparently the existence of a maximum stable particle diameter which depends on the relative air velocity.

It is apparent from the above considerations that K_s for a monodisperse medium would be a good approximation to employ for high speed scattering measurements. That these subsonically gathered data would apply in supersonic flow was not known a priori, and another qualitative criterion (Section IV-D) was used to determine the selection of the appropriate K_s.

Since computations of $\bar{\bar{K}}_s$ and $\bar{\bar{K}}_s/\alpha_{32}$ were not available for water in air with small $\Delta\alpha$, these were computed assuming an equivalent top hat distribution for $\phi(\alpha)$. By equivalent top hat distribution is meant that rectangular distribution which encompasses the same area as the distribution measured in condensation experiments. Instead of $\Delta\alpha/\bar{\alpha} = 0.33$, the equivalent rectangular distribution has $\Delta\alpha/\bar{\alpha} = 0.375$. From Eq. (B-6) through (B-9)

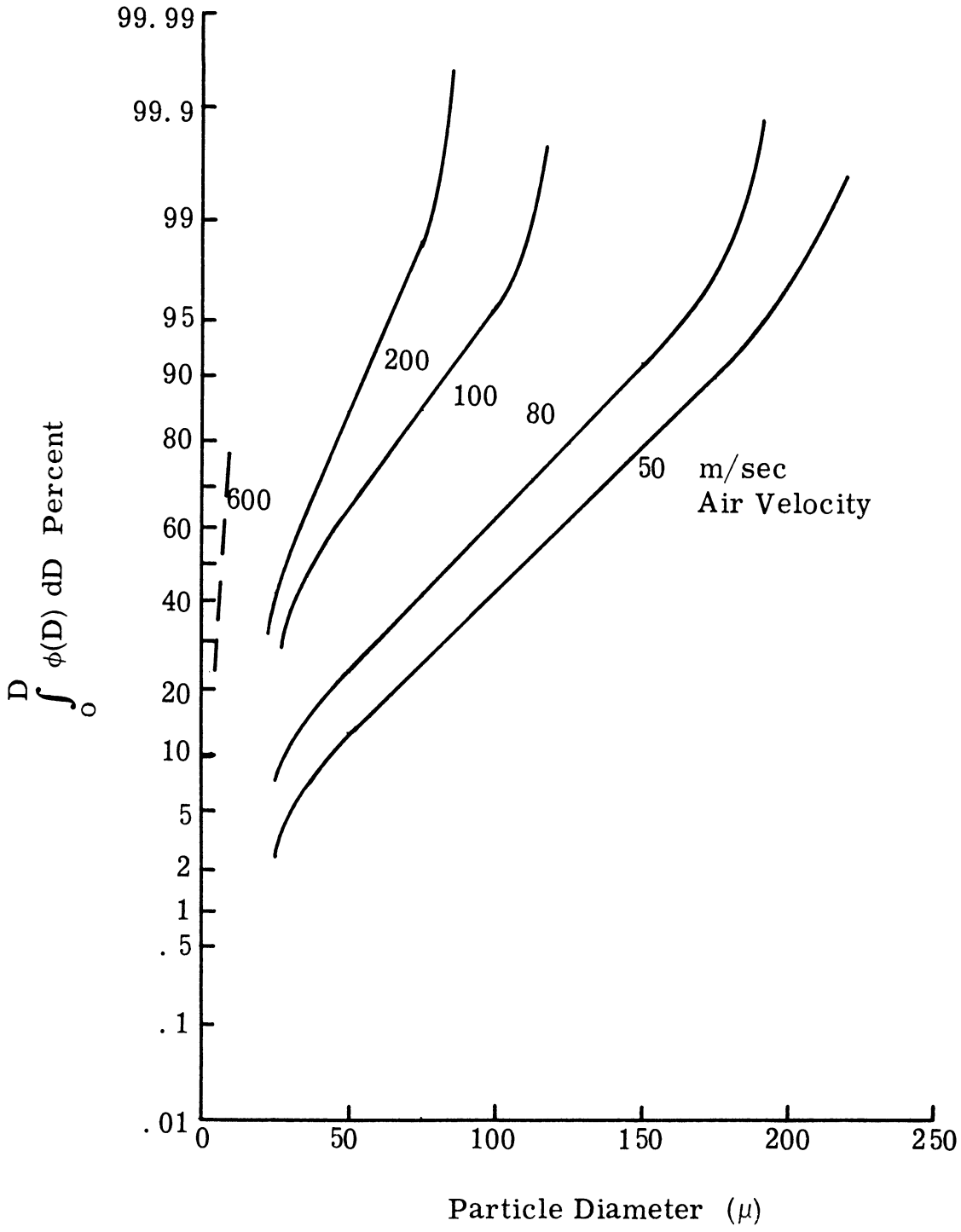

Figure 25. Cumulative Droplet Size Distributions as a Function of Relative Airstream Velocity

$$\overline{\alpha^2} = \bar{\alpha}^2 + \frac{(\Delta\alpha)^2}{3} \tag{B-19}$$

$$\overline{\alpha^3} = \bar{\alpha}^3 + \bar{\alpha}(\Delta\alpha)^2 \tag{B-20}$$

$$\alpha_{32} = \bar{\alpha}\,\frac{1 + \left(\frac{\Delta\alpha}{\bar{\alpha}}\right)^2}{1 + \frac{1}{3}\left(\frac{\Delta\alpha}{\bar{\alpha}}\right)^2} \tag{B-21}$$

for a top hat distribution. This distribution, in view of the aforementioned insensitivity of $\bar{\bar{K}}_s$ to shape, was chosen for its mathematical simplicity. The width was chosen as being one reasonable initial estimate that could be employed based on available information. Using the published values of K_s [31], the quantities $\bar{\bar{K}}_s$, $\bar{\bar{K}}_s/\alpha_{32}$ and $\overline{K_s\alpha^2}$ were computed numerically. The results are shown in Fig. 26 and 27 along with their monodisperse ($\Delta\alpha \to 0$) counterparts. From the figures, it may be concluded that the width criterion, $\Delta\alpha/\bar{\alpha} = 0.375$, provides a smoothing which is roughly mid-way between $\Delta\alpha \to 0$ and $\Delta\alpha \to \infty$. As discussed in Section IV-D, this width actually proved to be too large to be consistent with the measured data. The scattering functions actually employed were those appropriate to an effectively monodisperse medium. The semi-quantitative criteria used to arrive at this choice are discussed in the text. The calculations presented here provide the rationale behind this choice and are, of course, necessary considerations in more general scattering media.

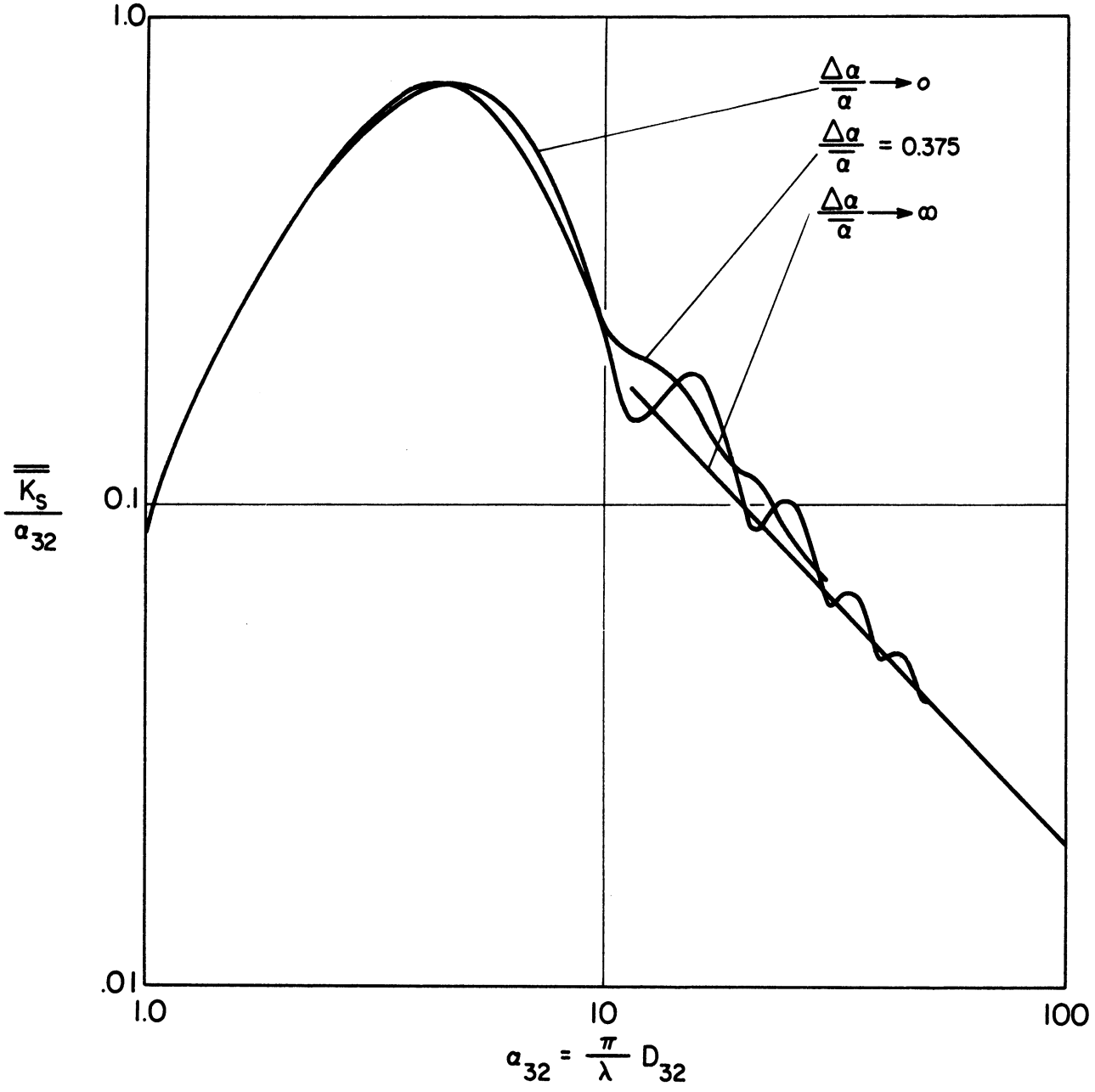

Figure 26. Specific Scattering Area Coefficient versus Volume/ Surface Mean Scattering Parameter; Top-hat Particle Size Distribution Width a Parameter

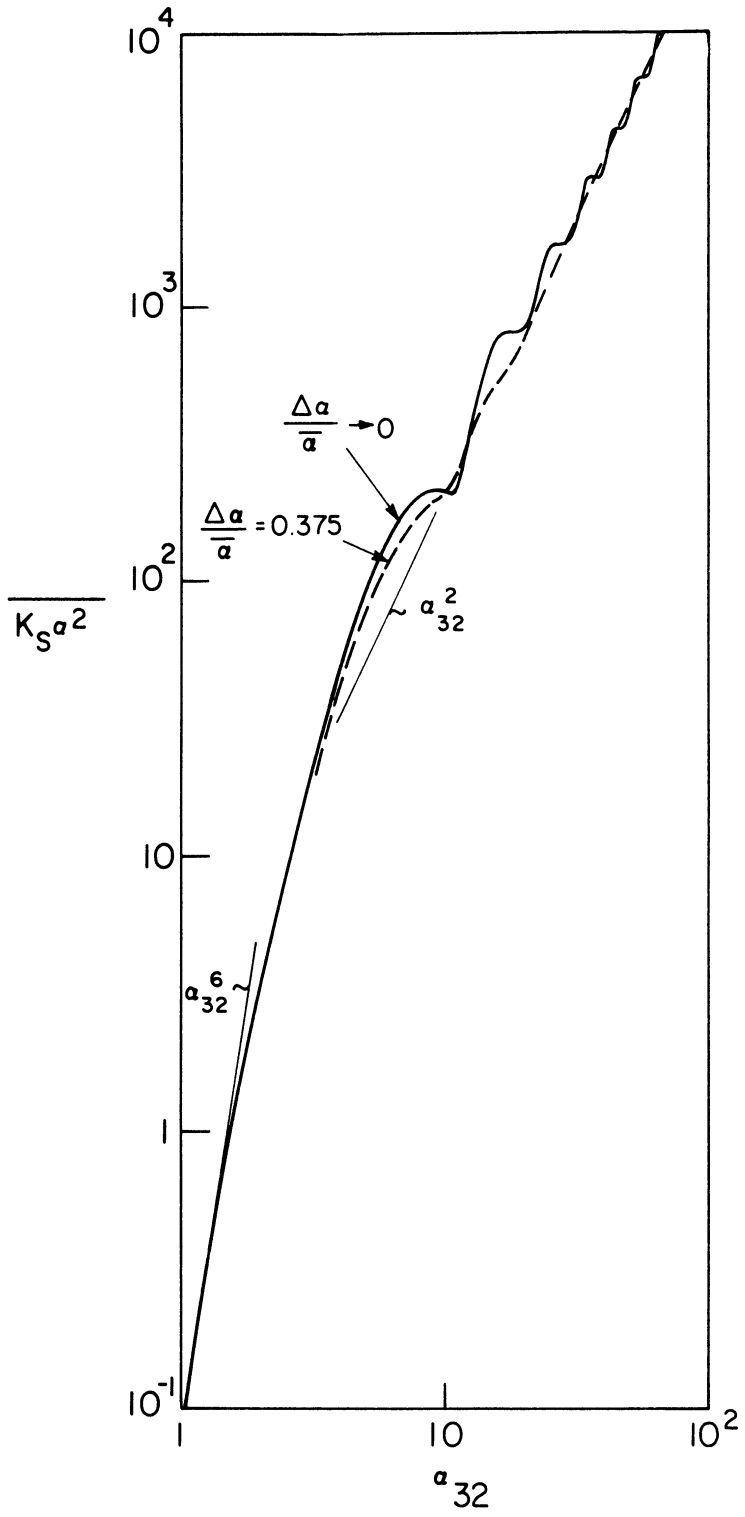

Figure 27. Particle Mean Scattering Area Coefficient versus Volume/Surface Mean Scattering Parameter; Top-hat Particle Size Distribution Width a Parameter

APPENDIX C

HF DATA REDUCTION FUNCTIONS

The line strengths, collision widths and various combined spectroscopic parameters pertinent to absorption measurements of the hydrogen fluoride molecule are compiled for R-branch fundamental vibration-rotation band absorption. They are to be used in connection with the data reduction procedures of Section V.

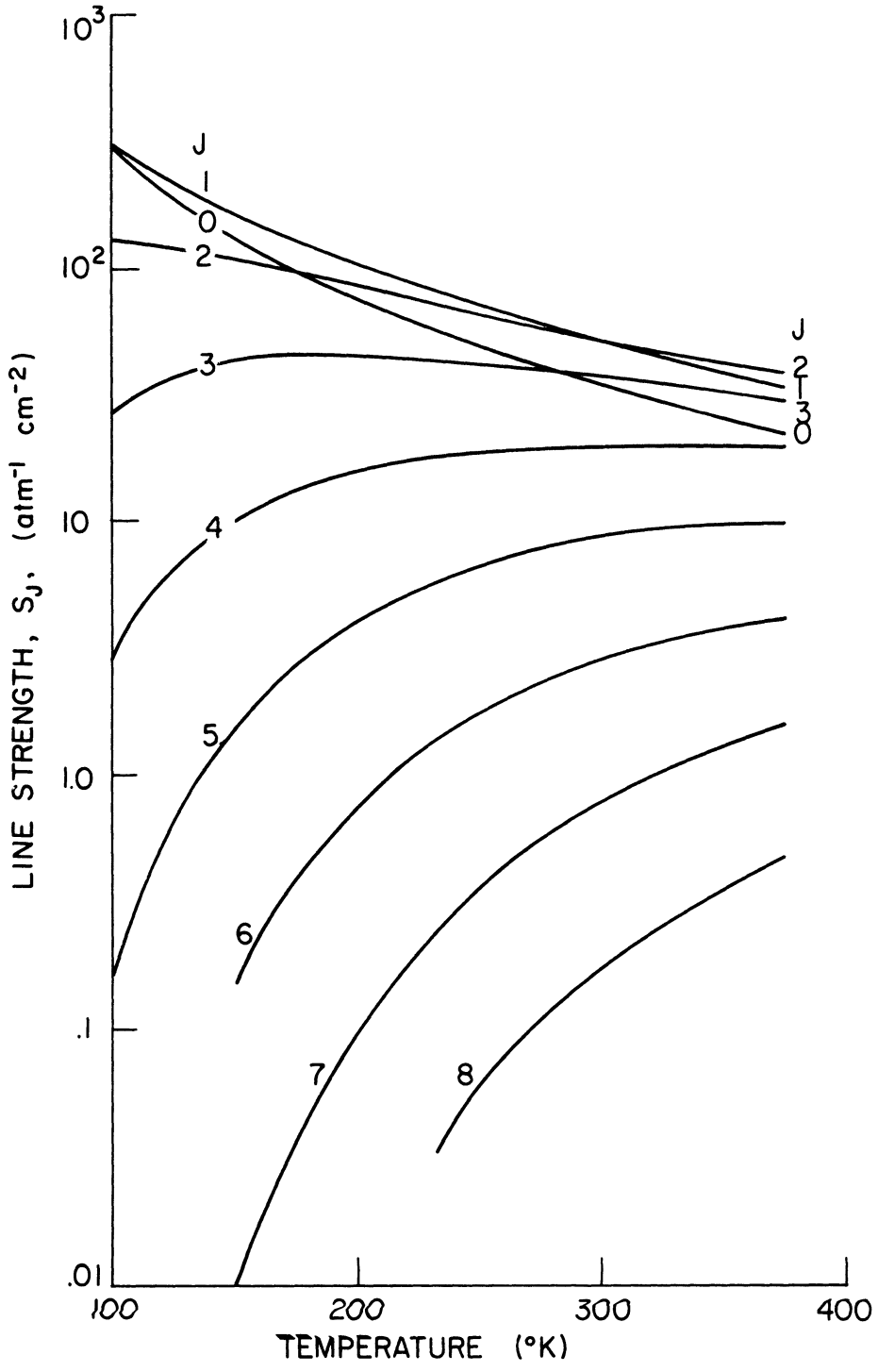

Figure 28. Hydrogen Fluoride Line Strength versus Temperature; Fundamental Vibration-Rotation Band, R-Branch Rotational Quantum Number a Parameter

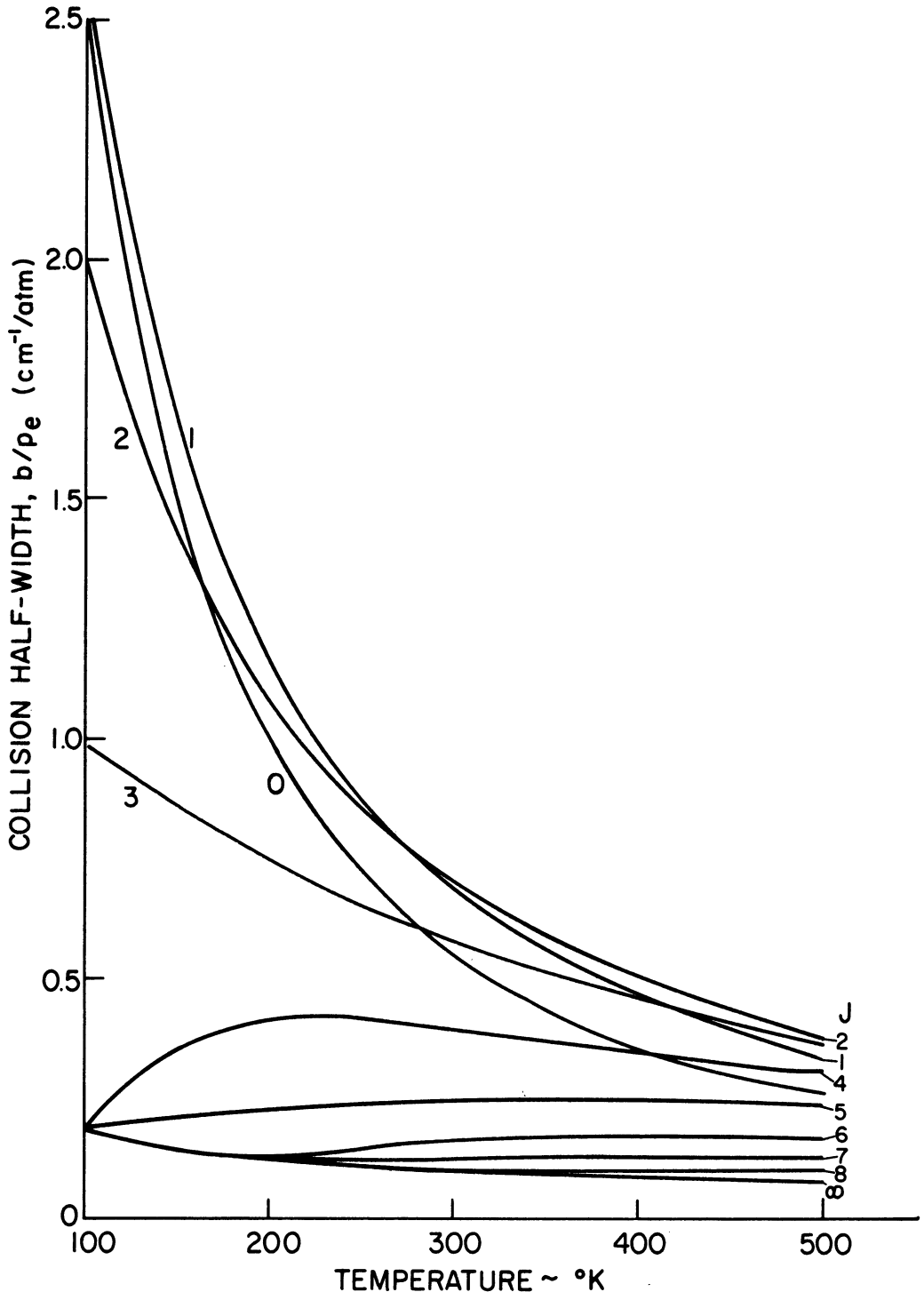

Figure 29. Collision Broadened Spectral Line Half-Width for HF Molecules in the RDBB Approximation; Rotational Quantum Number (R-Branch) a Parameter

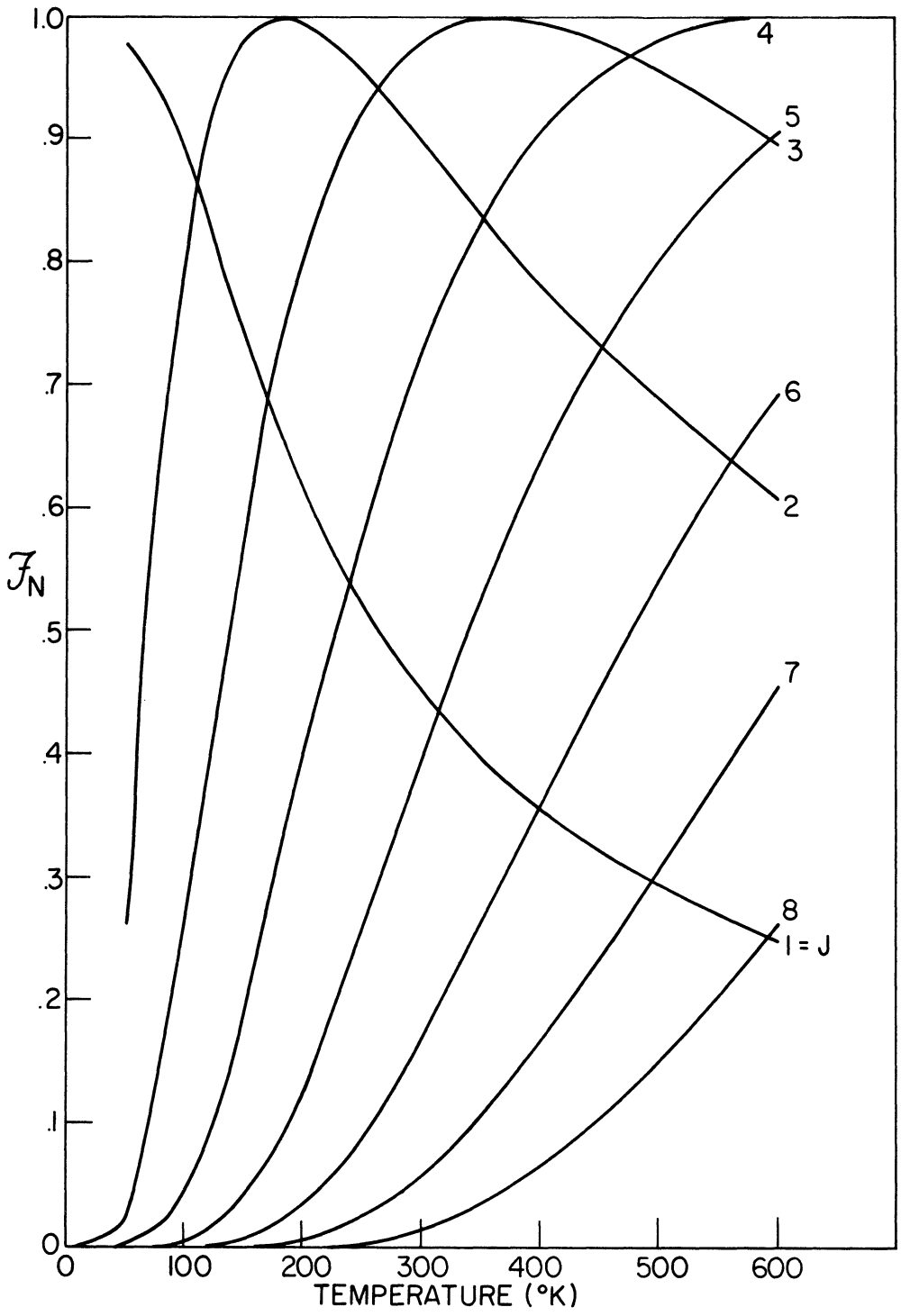

Figure 30. Normalized Temperature Dependence of HF Line Strength Linearized w/r Number Density. Weak Line Approximation, R-Branch Rotational Quantum Number a Parameter

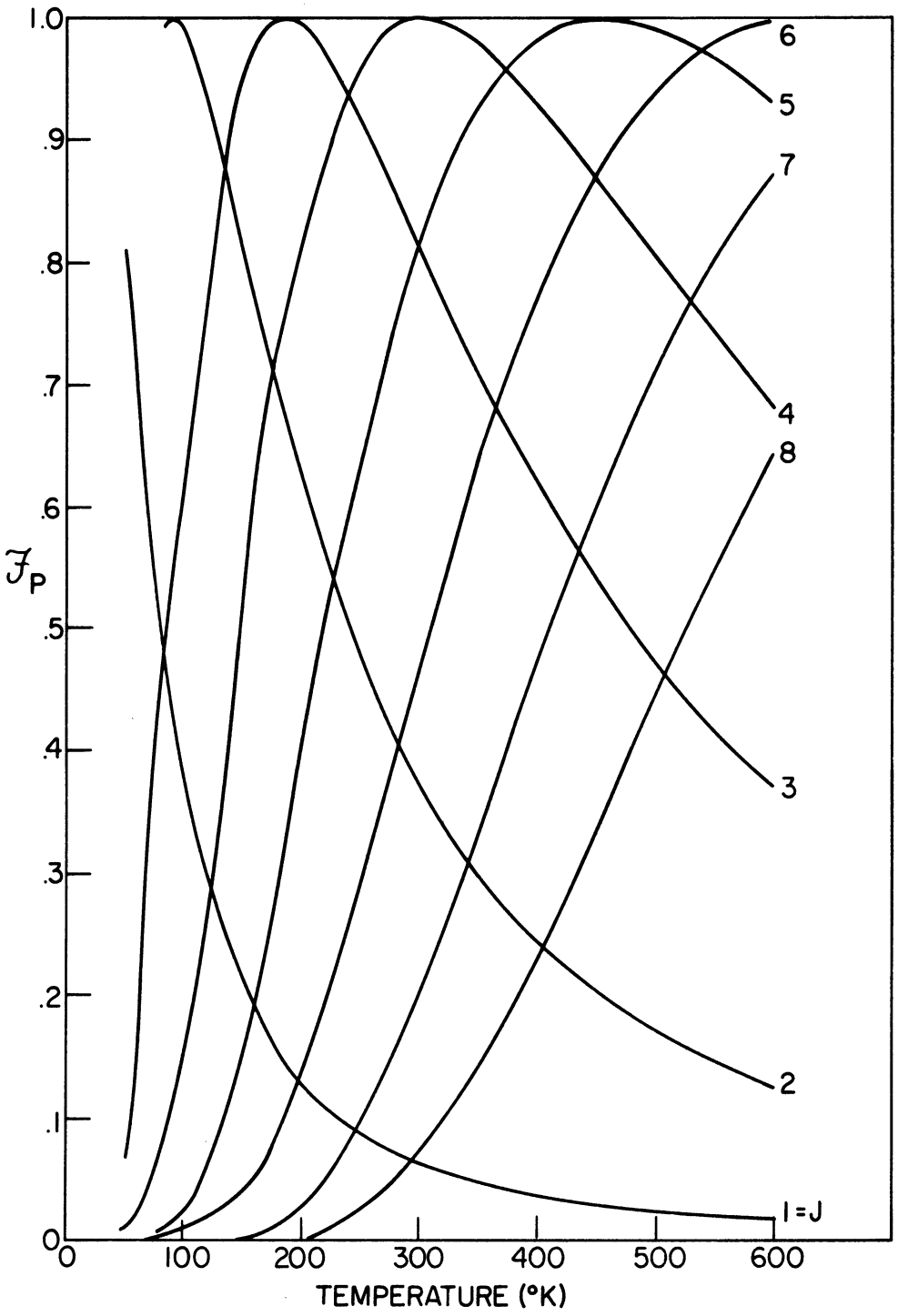

Figure 31. Normalized Temperature Dependence of HF Line Strength Linearized w/r Partial Pressure. Weak Line Approximation, R-Branch Rotational Quantum Number a Parameter

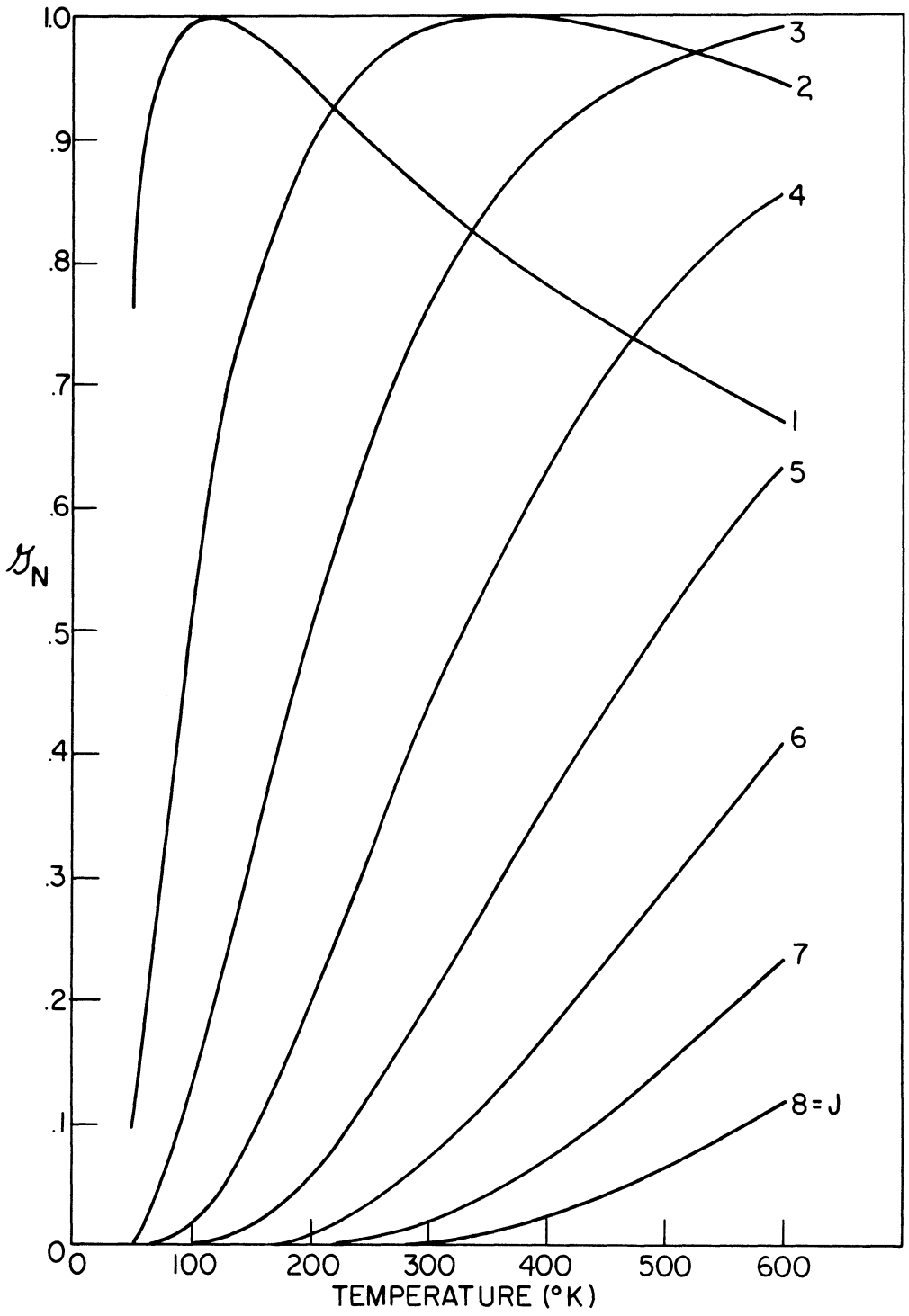

Figure 32. Normalized Temperature Dependence of HF Line Strength-Width Product Linearized w/r Number Density. Strong Line Approximation, R-Branch Rotational Quantum Number a Parameter

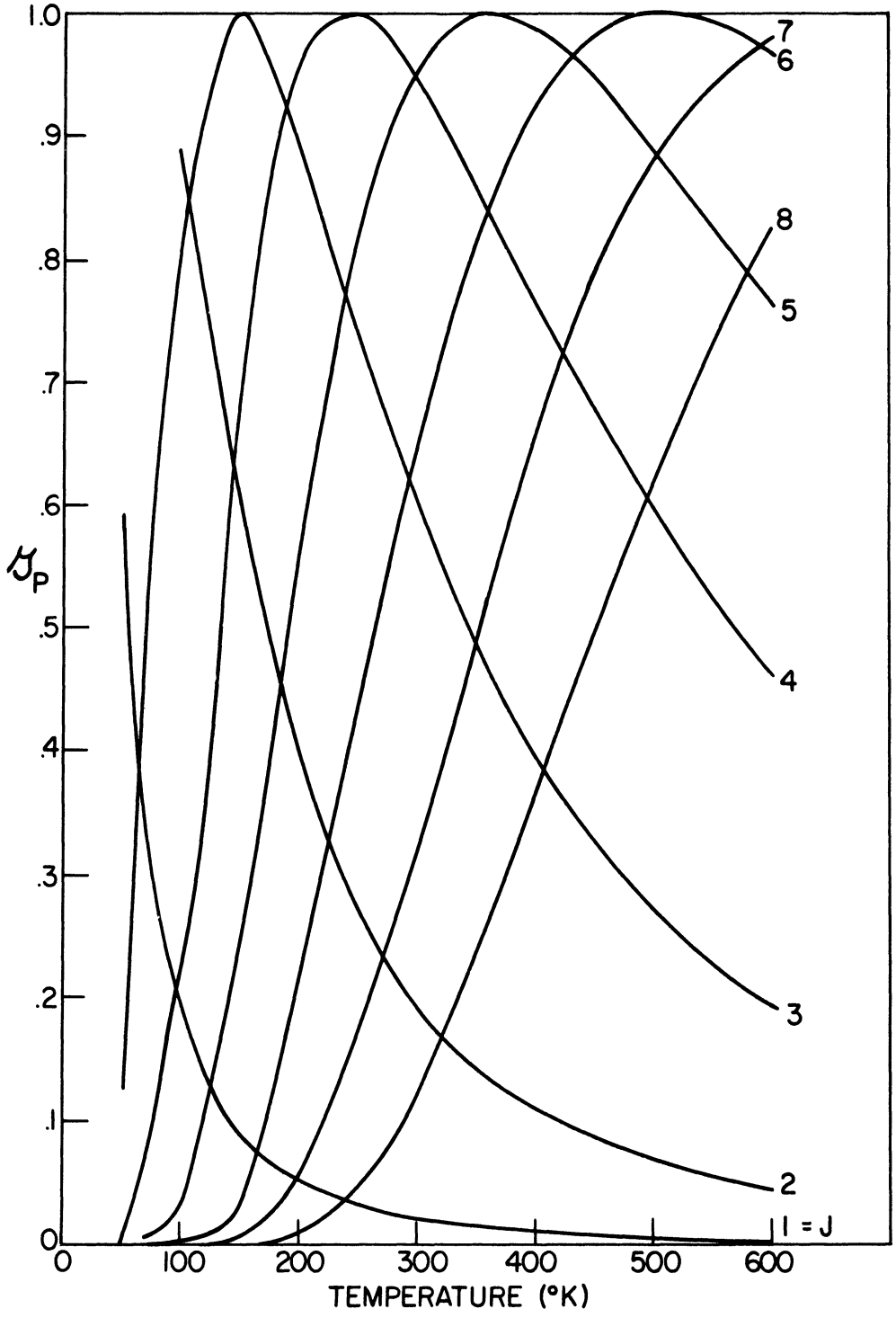

Figure 33. Normalized Temperature Dependence of HF Line Strength-Width Product Linearized w/r Partial Pressure. Strong Line Approximation, R-Branch Rotational Quantum Number a Parameter

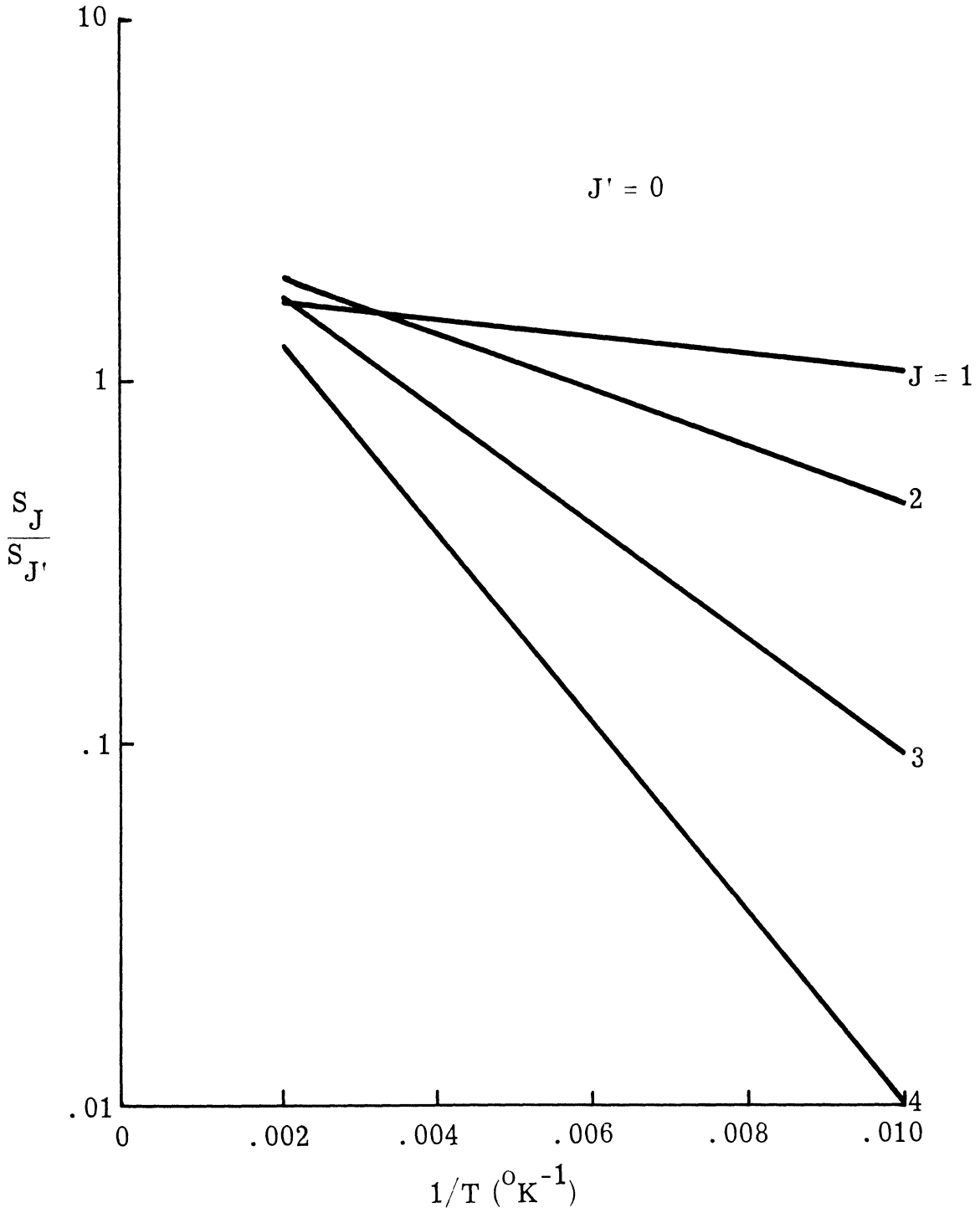

Figure 34. HF Line Strength Ratios, R-Branch Rotational Quantum Number a Parameter

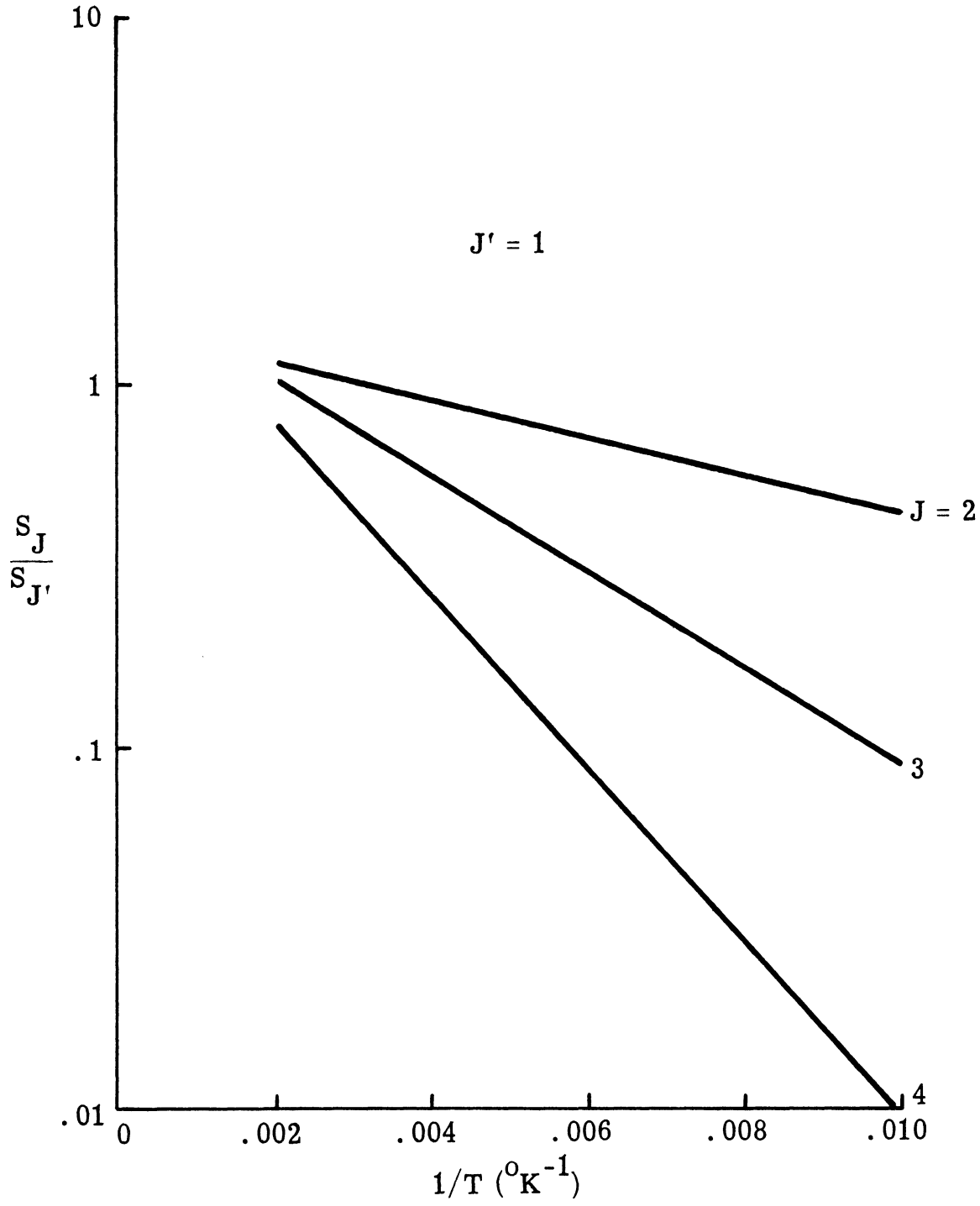

Figure 35. HF Line Strength Ratios, R-Branch Rotational Quantum Number a Parameter

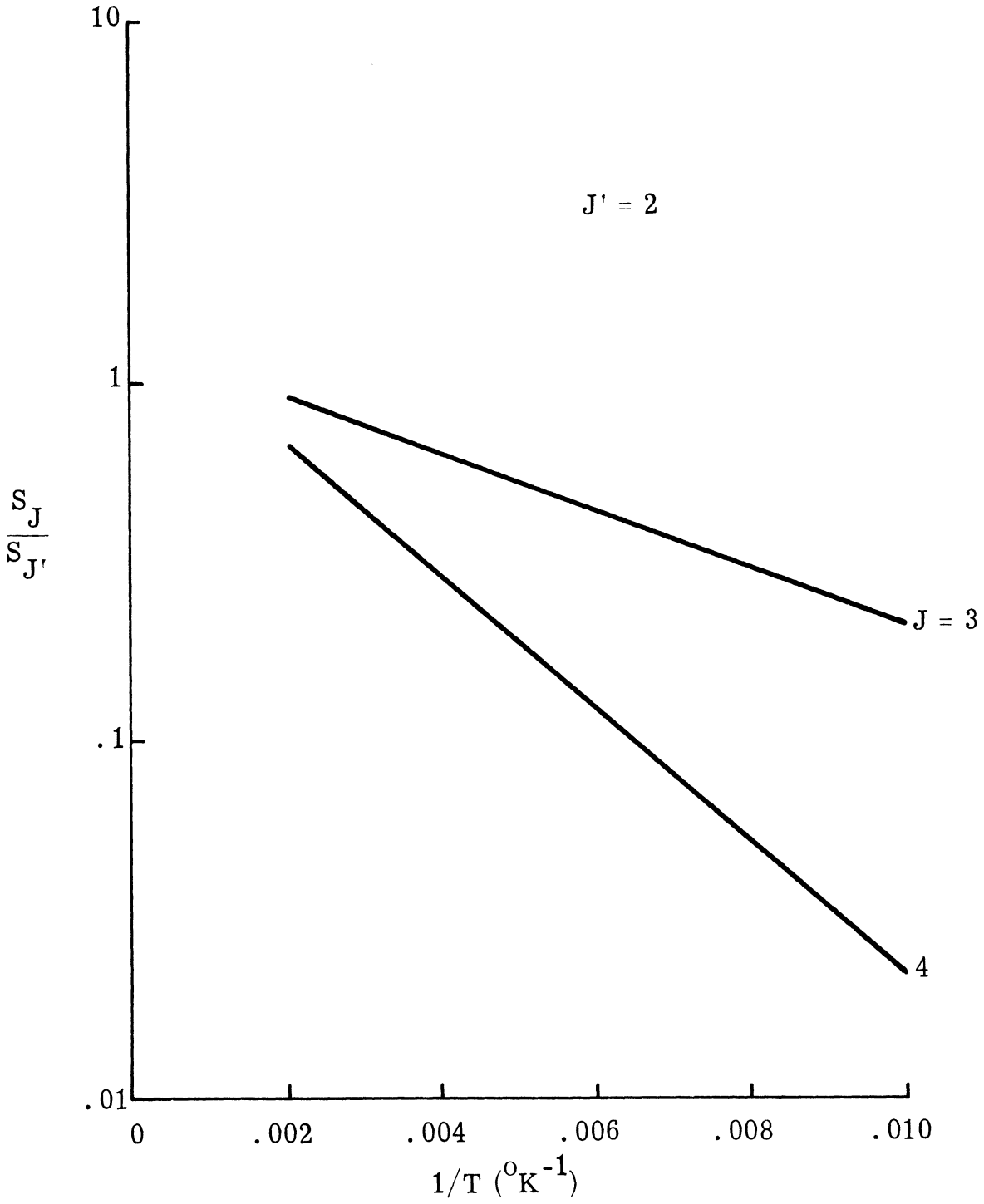

Figure 36. HF Line Strength Ratios, R-Branch Rotational Quantum Number a Parameter

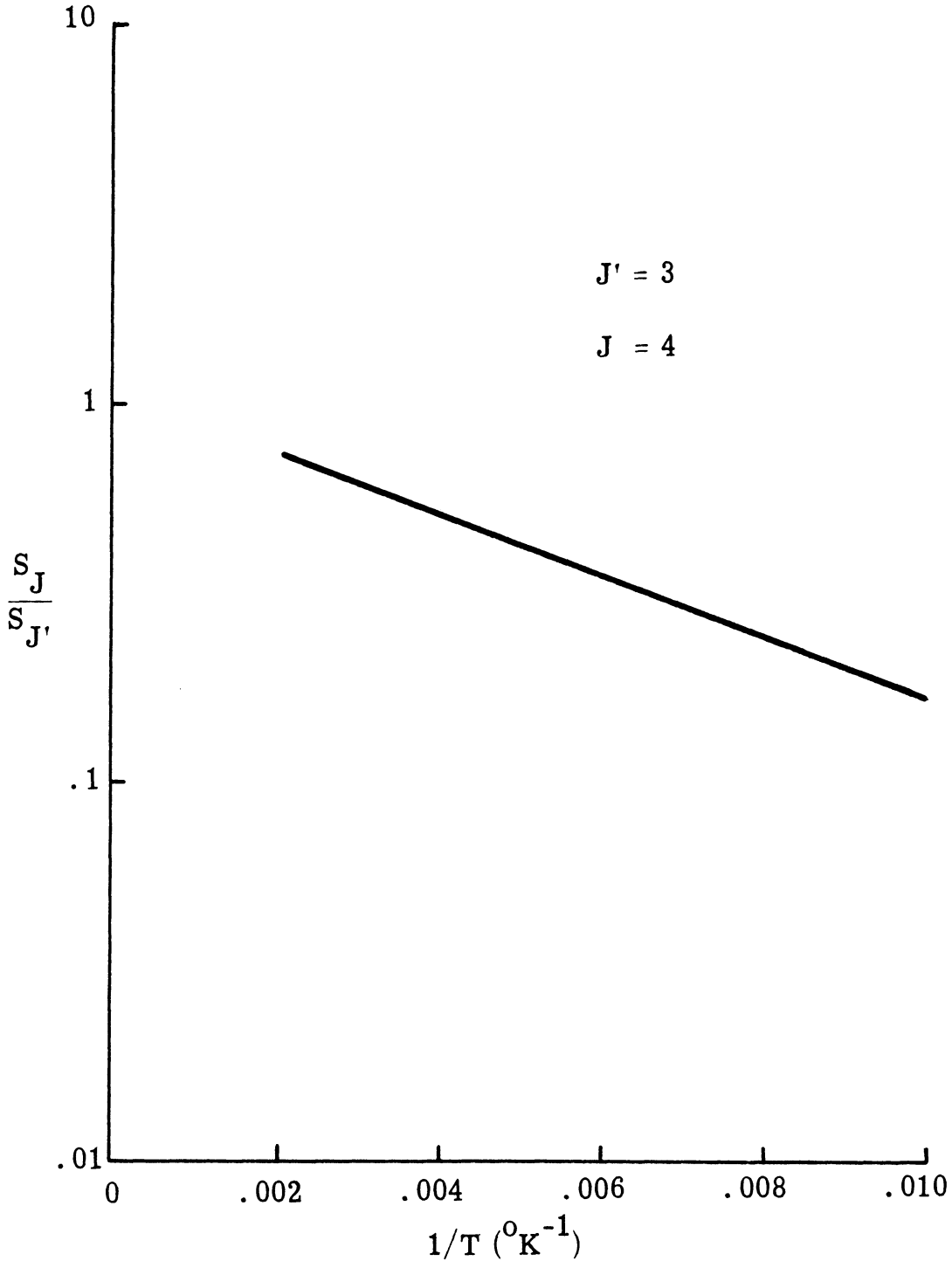

Figure 37. HF Line Strength Ratio, R-Branch Rotational Quantum Number a Parameter

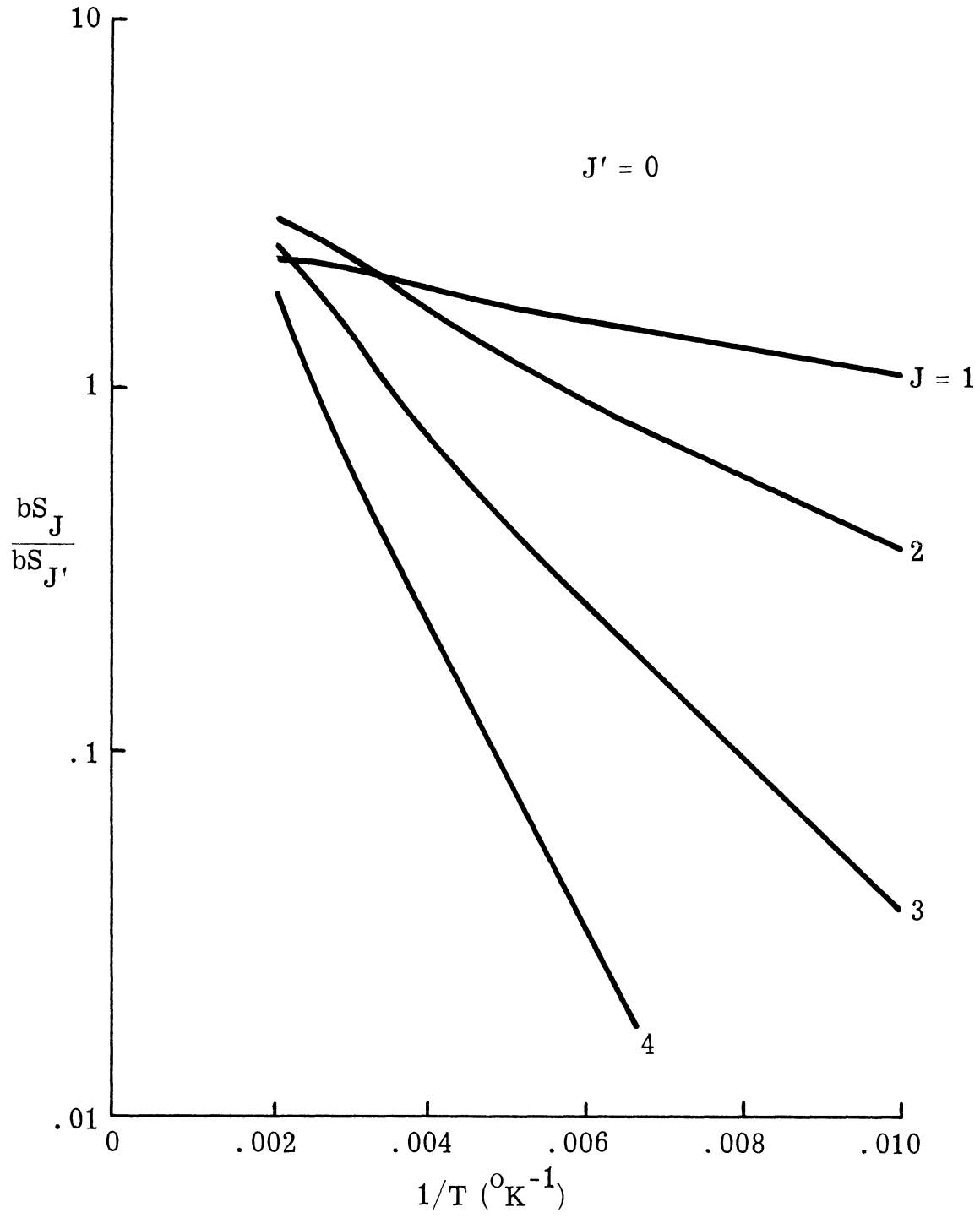

Figure 38. HF Line Width-Strength Ratios, R-Branch Rotational Quantum Number a Parameter

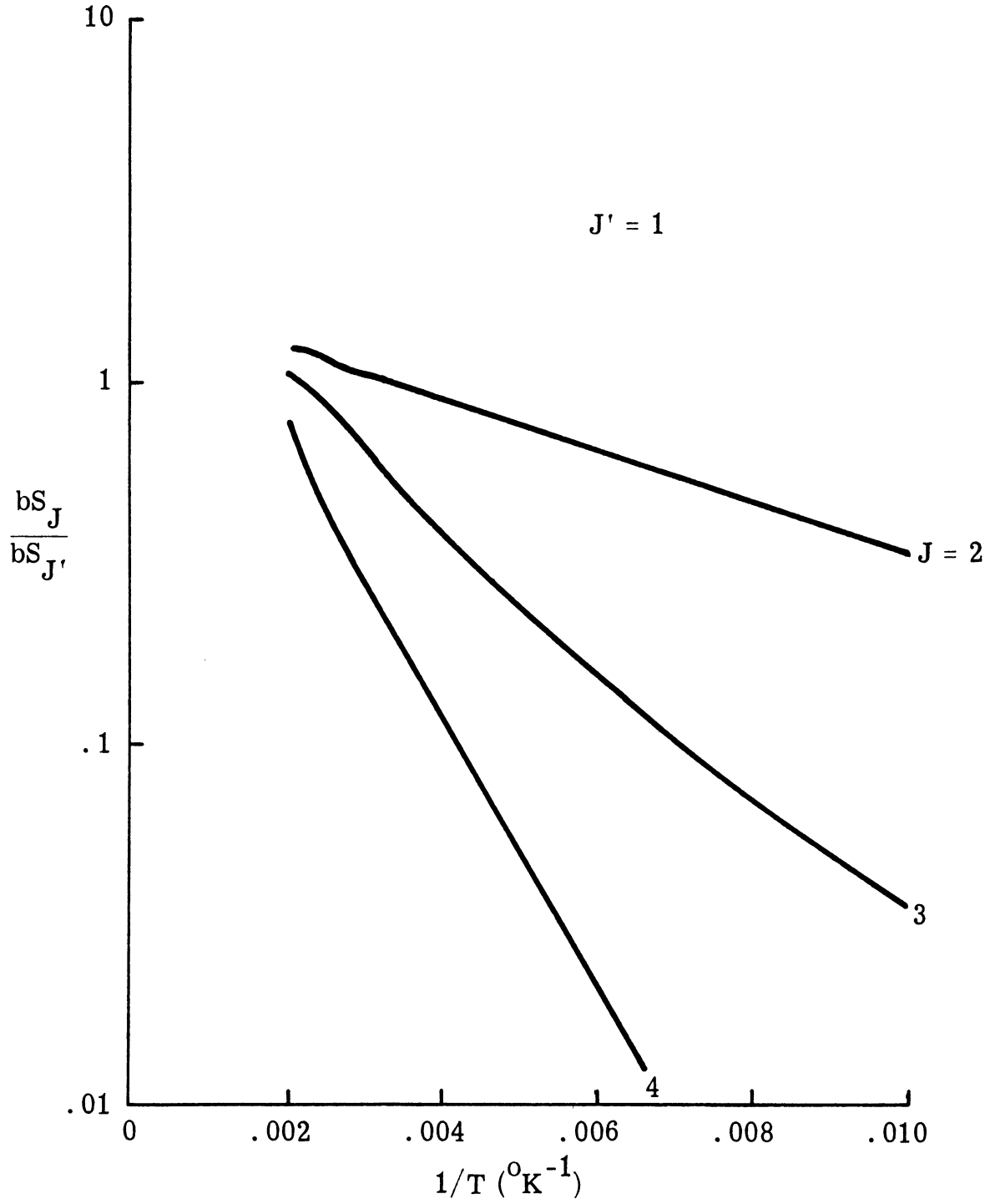

Figure 39. HF Line Width-Strength Ratios, R-Branch Rotational Quantum Number a Parameter

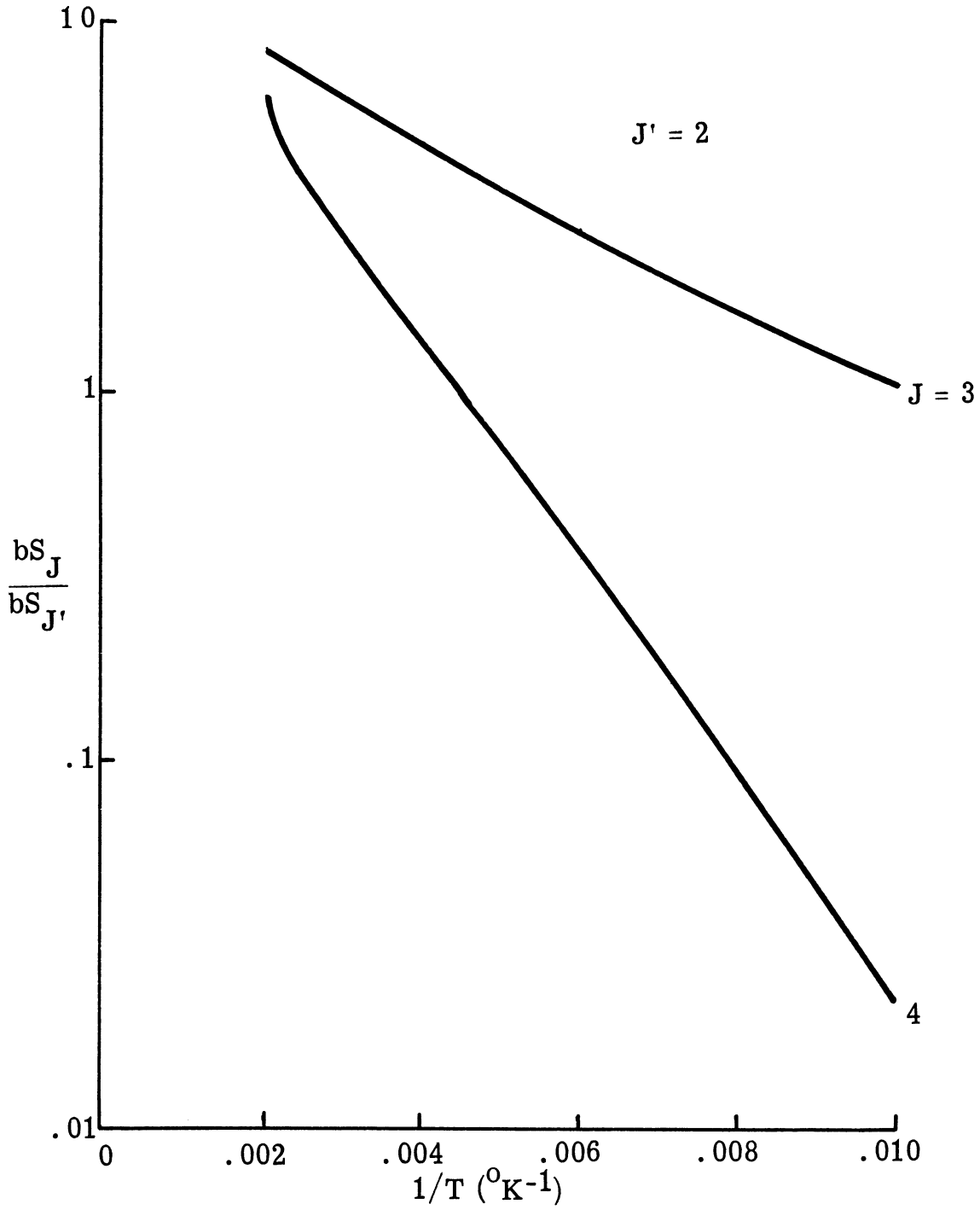

Figure 40. HF Line Width-Strength Ratios, R-Branch Rotational Quantum Number a Parameter

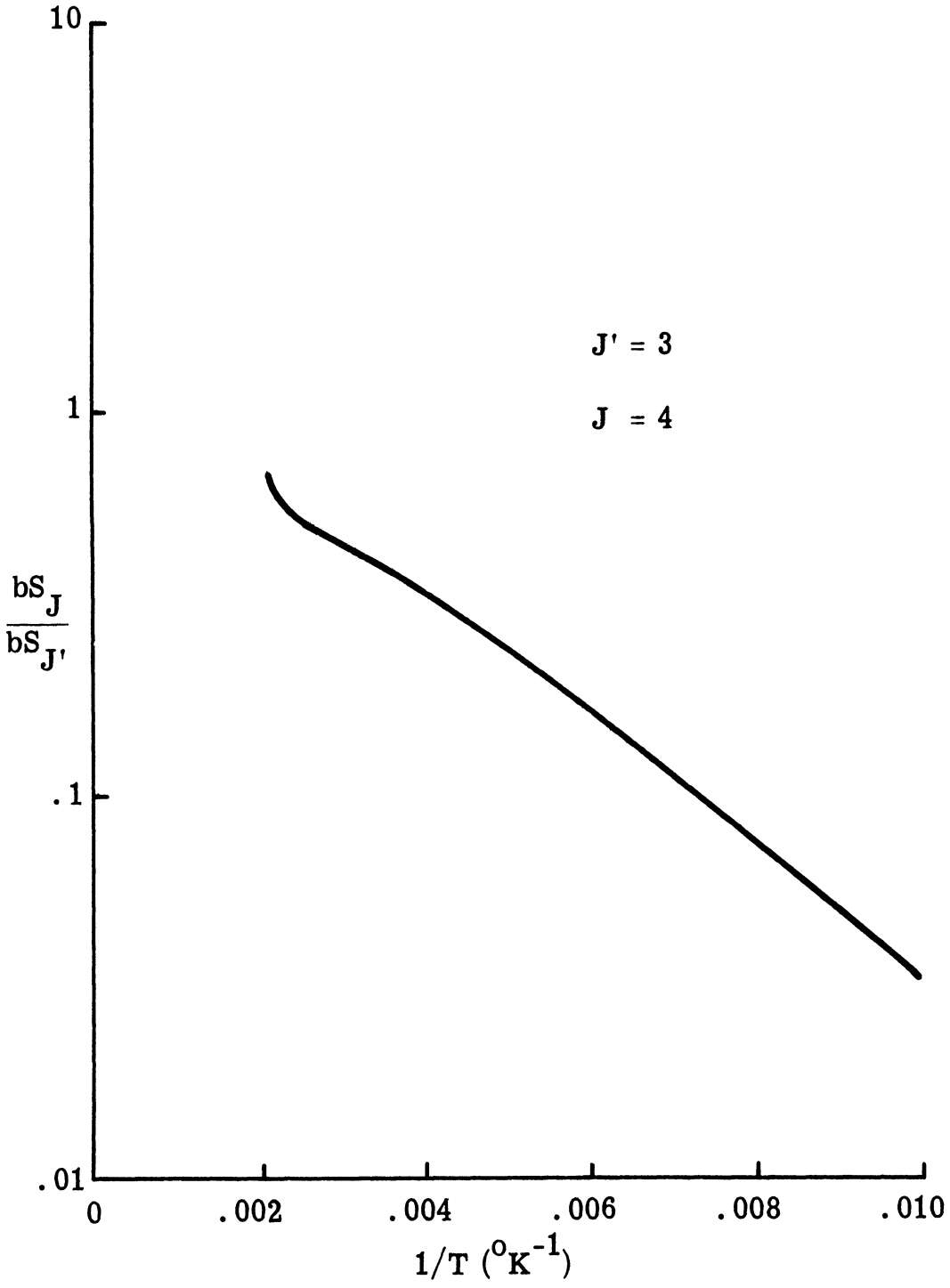

Figure 41. HF Line Width-Strength Ratio, R-Branch Rotational Quantum Number a Parameter

APPENDIX D

MONOCHROMATOR CALIBRATION AND PERFORMANCE

1. Photoconductive Detector Response Characteristics

The IR detector employed in the monochromator is a quantum (as opposed to thermal) detector of the photoconductive type. It consists of a thin semi-conductive film of PbS vacuum deposited on a glass substrate. Incident photons transfer their energy to film electrons which, as a result, suffer a change of state. By observing the number of electrons changing energy state, it is possible to measure the incident photon flux. If one knows the energy of each photon, one can then deduce the power of the incident radiation[69, 70].

The energy transition giving rise to the photoconductive effect is that of an electron being freed from the highest energy state of electrons without transitional motion (valence band) and inserted into the conduction band immediately above it. In this process, two charge carriers are created: an electron of charge, -e, and a hole of charge, e, in the valence band. These charge carriers are then free to move within their respective bands under the action of electric and magnetic fields. The net effect of this increased mobility is a decrease in the electrical resistance of the film.

The transitions between the valence band and the conduction band are termed intrinsic transitions and require photons whose energy is

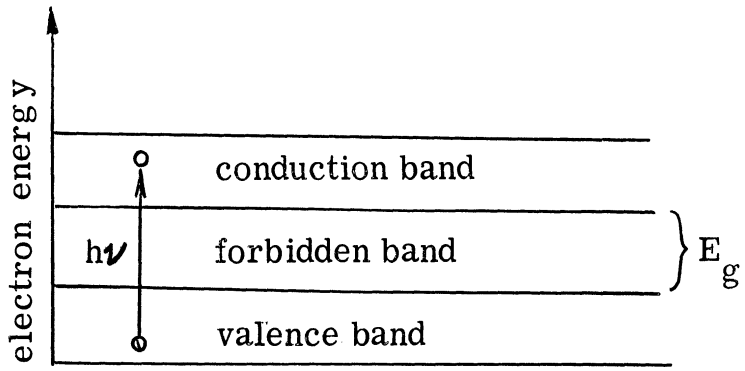

at least equal to that of the forbidden gap, E_g. This energy is a material and thermal property. Uncooled PbS is most sensitive to photons whose energy lies between 0.8×10^{-12} and 2×10^{-12} ergs ($1 < \lambda < 2.5\mu$).

It is this forbidden band of electron energy values which characterizes semiconductors. Pure conductors do not possess such a band while pure insulators have $E_g \gtrsim 2$ ev $= 3.2 \times 10^{-12}$ ergs. Semiconductors containing impurities in their crystal lattice structure may permit electronic transitions within the forbidden gap. Such transitions are termed extrinsic transitions. These extrinsic semiconductors are further classified as being n- or p-type according to whether the transition takes place from the forbidden band to the conduction band or from the valence band to the forbidden band, respectively. Extrinsic, or impurity, semiconductors are generally employed where long wavelength energy must be detected.

In practice, the photoconductor is biased by a voltage E and the change in voltage drop, V_L, across a series load resistor R_L is measured as a function of photon power incident on the detector of variable resistance, R_C.

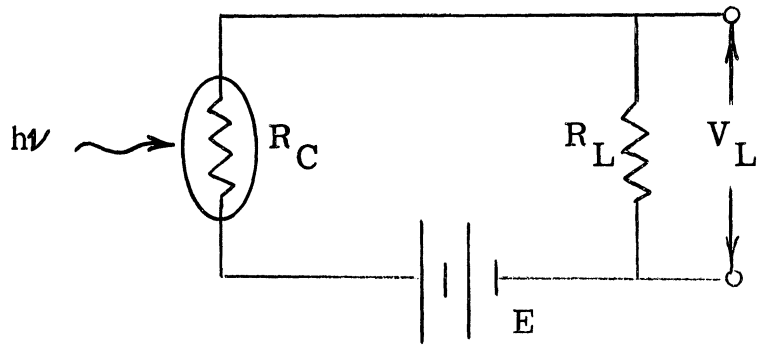

The voltage drop across the load resistor is given by

$$V_L = R_L I = \frac{ER_L}{R_C + R_L} \tag{D-1}$$

and a change in this voltage, as a result of a decrease in the PbS cell's resistance, is obtained by differentiation

$$\Delta V_L = - \frac{ER_L}{(R_L + R_C)^2} \Delta R_C \tag{D-2}$$

Maximum signal power is transferred if the load resistance is matched to the cell resistance. For this reason, R_L is set equal to the "cold" cell

resistance, R_C = 4. 2 Megohm. The bias voltage, E, is supplied by a 22. 5 V battery. Equation (D-2) then indicates that the signal level will be

$$\Delta V_L \text{ (volts)} = - 1.34 \times 10^{-6} \Delta R_C \text{ (ohms)} \qquad \text{(D-3)}$$

a. Specific Responsivity

The relation between ΔR_C and the incident radiant energy flux density, J (watts/cm^2), is expressed in terms of the specific responsivity, S_1,[71]

$$\frac{\Delta R_C}{R_C} = - 4 S_1 J \qquad \text{(D-4)}$$

Using this as the definition of S_1 and Eq. (D-2), leads to

$$S_1 = - \frac{\Delta V_L}{JE} \frac{(R_C + R_L)^2}{4 R_C R_L} \approx - \frac{\Delta V_L}{JE} \qquad \text{if } R_C \approx R_L \qquad \text{(D-5)}$$

S_1 is a function of wavelength, cell temperature, light beam modulation frequency, f_o, and bias voltage if the latter is sufficiently great to cause cell temperature rise due to Joule heating. The latter effect is negligible in the present case.

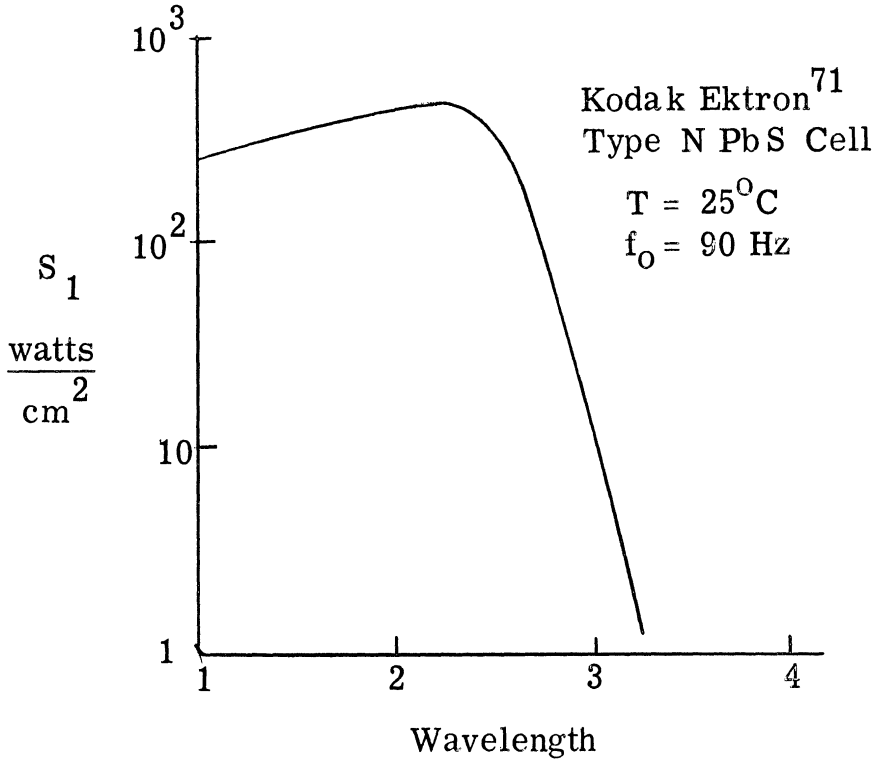

b. Detectivity and Noise

The smallest detectable signal is determined by the entire system's noise level. Nosie may be defined as any signal variation which does not convey information about the particular physical phenomenon being investigated. Noise originates within the detector itself, in the associated detection electronics and circuitry, and from the environment.

All noise may be characterized by its power spectral density (PSD). That is, all physical time variations may be Fourier transformed into the frequency domain. The Fourier transform of a voltage, V(t), yields an amplitude density in the frequency domain[72]

$$A(f) = \int_{-\infty}^{\infty} V(t)\, e^{-i2\pi ft} dt \qquad \text{(D-6)}$$

and the inverse

$$V(t) = \int_{-\infty}^{\infty} A(f)\, e^{i2\pi ft}\, df \qquad \text{(D-7)}$$

V(t) does not completely describe a voltage, however. Phase as well as amplitude is necessary. Power is independent of phase and is therefore used to characterize noise. The noise PSD is defined

$$P_N(f) = \int_{-\infty}^{\infty} |V_N(t)|^2\, e^{-i2\pi ft}\, dt \qquad \text{(D-8)}$$

and the inverse

$$|V_N(t)|^2 = \int_{-\infty}^{\infty} P_N(f)\, e^{i2\pi ft}\, df \qquad \text{(D-9)}$$

It is understood that only the real part of the above integrals are to be considered. Since all physical signals are measured relative to some beginning, the above integrals may be taken from 0 to ∞. When performing mathematical operations, such as convolution, it is more convenient to use the doubly infinite definitions however.

When $P_N(f)$ is discreet (a line spectrum), the instantaneous power is periodic. Thus the PSD of a 60 Hz line voltage would be approximated by a delta function of area $|V|^2$ located at f = 60 Hz.

$$P_N(f) = |V|^2 \, \delta(f - 60)$$

No physical waveform is ever truly monochromatic (of a single frequency) so that some of the power is distributed among higher harmonics of the fundamental frequency. Thus the PSD of a real 60 Hz power line would be represented by

$$P_N(f) = \sum_{n=0} |V|^2 \, a_n \, \delta(f - 60n) \quad ; \quad n = 0, 1, \ldots$$

where a_n is the fraction of power possessed by the nth harmonic. If no D. C. power is present $a_o = 0$. The PSD represented by the above equation is known as a Dirac comb[72].

When $P_N(f)$ is a continuous spectrum, $V_n(t)$ is a random function. Continuous noise spectra arise from any random fluctuation which influences the measured signal, e. g. temperature, photon arrival rate, charge carrier density, density of absorbers. Noise pertinent to IR detectors is discussed below.

(1) Johnson Noise[70]

Johnson noise is present in all resistive circuit elements, including the PbS detector. It arises from the random thermal motions of electrons and has as its PSD

$$P_{JN}(f) = 4kTR \qquad \text{(D-10)}$$

where k = Boltzmann's constant

T = resistor temperature

R = resistance

This PSD is, for all practical purposes, "white", i. e., constant with respect to frequency. The integral pf $P_{JN}(f)$ is the total thermal noise power and would seem to diverge. This paradox is explained by taking into account the quantum nature of energy as higher frequencies are encountered. The exact expression for $P_{JN}(f)$ is[70]

$$P_{JN}(f) = 4kTR \frac{hf/kT}{e^{hf/kT} - 1}$$

which reduces to the former expression when $f \ll kT/h = 2.1 \times 10^{10} T$ where h is Planck's constant, $[f]$ = Hz and $[T]$ = ^{o}K.

(2) Generation-Recombination Noise

Generation-recombination noise arises from fluctuations in the recombination rate of electrons and holes relative to their photoionization rate. The net result is a fluctuation in the total number of charge carriers present in the detector, a situation which leads to a fluctuation in the conductivity of the detector.

The power spectral density of G-R noise is non-white and is proportional to

$$P_{GR}(f) \sim \frac{1}{1 + (2\pi f \tau)^2} \qquad \text{(D-11)}$$

where τ is the mean lifetime of an electron in the excited state. A rigorous derivation of P_{GR} involves the consideration of transition probabilities, electron andhole mobilities and vibrations of the lattice structure and will not be reproduced here[69]. It is sufficient for present purposes to say that G-R noise is greater than Johnson noise below the roll-off frequency, $f = (1/2\pi\tau)$, for a typical photoconductive detector.

(3) 1/f Noise

The third important type of noise in a photoconductive detector is 1/f noise, so-called because its PSD varies inversely as f^n where n is of the order of one. Its origin is not precisely known but it is related to circuit imperfections, e.g. contacts.

The three preceding types of noise are the most significant in the determination of the detector's signal to noise ratio, S/N. The sum of their PSD's are shown below for a typical PbS detector at room temperature.

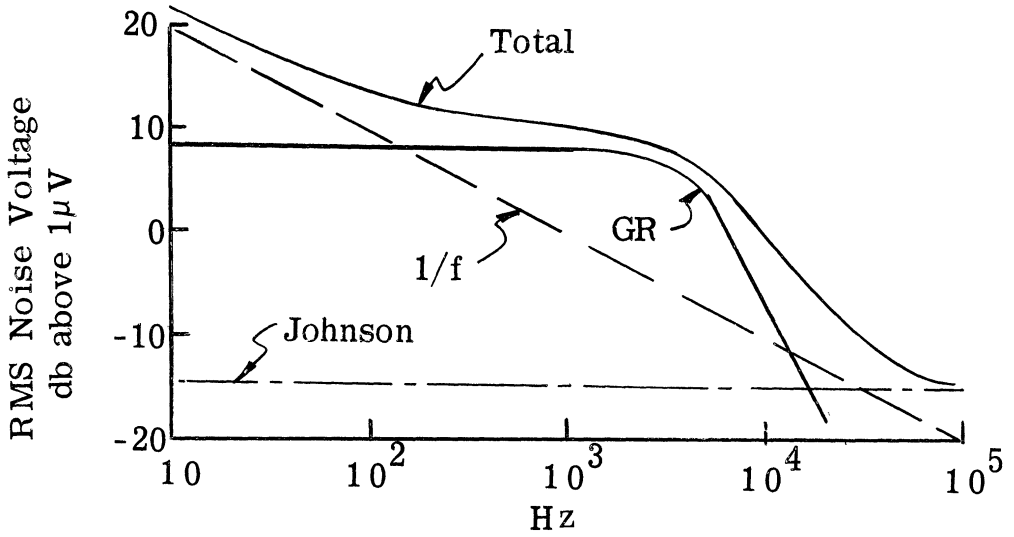

It is this low frequency increase in the noise power which makes it desirable to move the signal information to a higher frequency by carrier beam modulation-chopping. The frequency chosen, 100 Hz, lies between 60 Hz power line harmonics. A higher frequency would appear desirable on the basis of the noise PSD distribution alone but other factors tend to limit the chopping frequency. The detector response falls off above 1000 Hz and the tuned amplifier bandwidth, Δf, is proportional to frequency. Thus a 10 Hz bandwidth at 100 Hz is a 100 Hz bandwidth at 1000 Hz.

Clearly, a signal voltage must be greater than the noise voltage contained within the detection bandwidth to have an unambiguous reading. This criterion leads to the definition of a Noise Effective Power (NEP); the radiant power input required to yield an output signal voltage equal to the noise voltage.

The relation between the incident radiant power density and its output voltage has been given by Eq. (D-5) in terms of the specific responsivity, S_1, a quantity based on unit bias voltage. In order to obtain the responsivity, $\mathcal{R}$ (volts out per watt input), for a biased detector of illuminated area, A_d, we must calculate

$$\mathcal{R} = \frac{\Delta V}{JA_d} = \frac{S_1 E}{A_d} \qquad \text{(D-12)}$$

In the present case, the detector area is 2.5 x 0.25 mm = 6.25 x 10^{-3} cm^2, E = 22.5 volts, and , $S_1 \simeq 300$ cm^2/watt. Thus the responsivity for a fully illuminated detector is

$$\mathcal{R} = 1.08 \times 10^6 \frac{\mu V}{\mu W} \tag{D-13}$$

The noise power contained in the bandwidth, Δf, is

$$\int_{-\infty}^{\infty} \Lambda (f)\, P_N(f)\, df = P_N(f)\, \Delta f \tag{D-14}$$

where $\Lambda(f)$ is the filter response (see below). Thus the noise voltage is

$$V_N = \sqrt{P_N(f)\, \Delta f} \tag{D-15}$$

The noise effective power is then, from Eq. (D-12)

$$NEP = (JA_d)_{NEP} = \frac{V_N}{\mathcal{R}} = \frac{P_N(f)\, \Delta f}{\mathcal{R}}, (\mu W) \tag{D-16}$$

Viewed reciprocally, NEP defines the Detectivity, i.e.,

$$\mathcal{D} = \frac{1}{NEP} \quad , \quad \left(\frac{1}{\mu W}\right) \tag{D-17}$$

a figure of merit so defined to increase in magnitude with detector quality.

Finally, a figure of merit normalized so as to be relatively independent of detector area and bandwidth has been defined and is the second characteristic (besides S_1) usually listed by manufacturers. It is

$$\mathcal{D}^* = \sqrt{A_d\,\Delta f}\,\mathcal{D} = \frac{\Delta V}{V_N}\,\frac{\sqrt{A_d\,\Delta f}}{JA_d}\,\frac{\text{cm}\sqrt{\text{Hz}}}{\text{watt}} \qquad \text{(D-18)}$$

It can be seen that $\mathcal{D}^*$ is characteristic of the S/N per unit input power. $\mathcal{D}^*$ for a PbS detector is shown below.

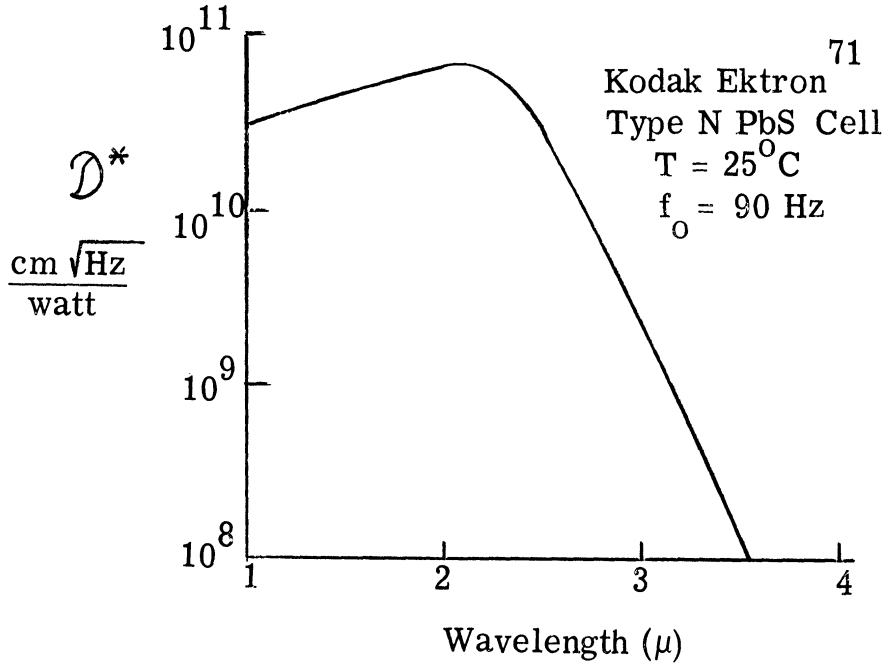

From the figure, we choose $\mathcal{D}^*\,(\lambda = 2.5\mu) = 3 \times 10^{10}$ cm Hz/watt. The noise effective power can now be computed as

$$\text{NEP} = \frac{\sqrt{A_i\,\Delta f}}{\mathcal{D}^*} = 8.33 \times 10^{-6}\ \mu\text{watts} \qquad \text{(D-19)}$$

for a 10 Hz bandwidth. This is the minimum radiant power that may be detected with a 10 Hz bandwidth.

The noise voltage may also be calculated from Eq. (D-16)

$$V_N = (NEP)\mathcal{R} = 9\ \mu V \qquad (D\text{-}20)$$

2. Monochromator Performance

In order to calculate the detector signal voltage, ΔV_L, the entire optical system, including source, focusing optics, filters, and monochromator must be considered. The specific responsivity, as defined above, presumes a perfect monochromator with the ability to pass radiation of only one wavelength to the detector. All monochromators, in fact, isolate radiation in a finite wavelength interval about the indicated scanning wavelength. The response to a continuous source spectral radiance takes the form of a convolution integral, the generalization of Eq. (D-5).

$$\Delta V_L(\lambda) = -\,E \int d\Omega \int_{-\infty}^{\infty} S_1(\lambda')\Lambda(\lambda')\, I_{\lambda'}\, g(\lambda - \lambda')\, d\lambda' \qquad (D\text{-}21)$$

where $\Lambda(\lambda)$ = optical filter transmission

I_λ = spectral radiance of source

Ω = solid angle subtended by optics as viewed by detector

$g(\lambda - \lambda')$ = monochromator slit function

This is characteristic of linear systems whose response at wavelength λ depends on events occurring at other wavelengths, λ', as well as those occurring at λ. Were no scanning involved (no variation of λ), the slit function would simply act like another filter centered about some constant wavelength.

The slit function may be either calculated approximately or measured accurately. If one were to employ a source whose spectral radiance could be represented by a delta function, then at each wavelength, λ, the voltage output would be proportional to the slit function. This is due to the fact that $S_1(\lambda)$ and $\Lambda(\lambda)$ vary slowly compared with $g(\lambda, \lambda')$ which, in turn, varies slowly compared with I_λ. This is easily seen by putting

$$I_{\lambda'} = I\delta(\lambda' - \lambda_m) \tag{D-22}$$

where I is the line radiance and $\delta(\lambda)$ is the Dirac delta function. Equation (D 21) becomes

$$\Delta V_L(\lambda) = -E\, S_1(\lambda_m)\Lambda(\lambda_m)\, I\, g(\lambda - \lambda_m) \int d\Omega \tag{D-23}$$

For narrow beamed optical systems, it is a reasonable approximation to consider I constant over the solid angle Ω subtended by the detector. The latter may be expressed in terms of the "eff" number, f/ , of the optics.

$$f/ = \frac{\text{image distance}}{\text{aperture}} = \frac{F}{d} \tag{D-24}$$

Therefore

$$\Omega F^2 = \text{Area} = \frac{\pi}{4} d^2$$

$$\Omega = \frac{\pi}{4}\frac{d^2}{F^2} = \frac{\pi}{4(f/)^2} \tag{D-25}$$

Thus,

$$\Delta V(\lambda) = -E \frac{\pi}{4(f/)^2} S_1(\lambda_m) \Lambda(\lambda_m) \, I \, g(\lambda - \lambda_m) \qquad \text{(D-26)}$$

A gaseous discharge tube filled with neon has been used to measure the slit function by the above method. Neon has a strong narrow emission line at $\lambda_m = 1.08\mu$. The resulting slit function is shown below.

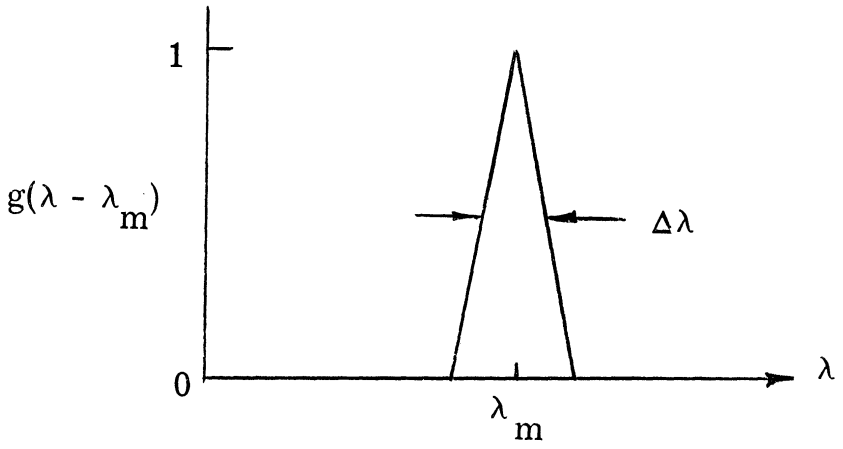

Triangular slit functions are characteristic of monochromators whose entrance and exit slits are of equal width. The slit function half-width at half-height, $\Delta\lambda$, is a measure of the spectral resolution of the monochromator. It depends on the Rayleigh diffraction limit as a lower bound, the grating dispersion, the physical width of the slits, and optical imperfections.

The Rayleigh diffraction limit prescribes a minimum $\Delta\lambda$ given by[73]

$$\frac{\lambda}{\Delta\lambda} = nN \qquad \text{(D-27)}$$

where n = diffraction order

N = number of grating grooves intercepted by the beam.

N is determined by the beam width at the grating and the number of grooves per mm of the grating. Referring to Fig. 42, the beam width is determined by the f/ ratio of the entrance optics and the focal length of the parabolic mirror in the monochromator.

$$f/ = \frac{36}{3} = 12 \tag{D-28}$$

Thus the beam width at the grating is 267 mm/12 = 22.2 mm.

The grating has 303 grooves per mm for a total illuminated number of grooves,

$$N = 22.2(303) = 6720 \tag{D-29}$$

Thus, for first order diffraction

$$\frac{\lambda}{\Delta\lambda} = 6720 \tag{D-30}$$

which implies a maximum attainable resolution at 2.3μ of

$$\Delta\lambda = \frac{2.3}{6720} = 3.42 \times 10^{-4}\mu \tag{D-31}$$

The parabolic mirror collimates the incoming radiation and directs it toward the reflection grating. The radiation reflected and dispersed by the grating through an angle θ with respect to the normal is characteristic of a wavelength

$$n\lambda = 2d \sin \theta \qquad n = 1, 2, 3, \ldots$$

where d is the groove width = 1/(303 grooves/mm) = 3.3μ/groove. From this equation, it is seen that the dispersed radiation collected by the parabola is characteristic of the spectral positions, λ, $(\lambda/2)$, $(\lambda/3)$, . . . In order to measure radiation of only one wavelength, a long-wavepass filter has been placed in the light path. This filter is composed of a germanium film evaporated on a sapphire substrate. It begins transmitting at $\lambda = 1.6\mu$ and passes radiation with approximately 90% transmission for $1.6 < \lambda < 3\mu$. Thus, if $\lambda = 2.5\mu$ is chosen by rotating the grating until $\theta = 22.2^{o}$, the second order radiation at $\lambda = 1.25\mu$ is prevented from reaching the grating. The wavelength calibration of the monochromator, obtained by Hg and H_2 discharge tubes, is shown in Fig. 43.

From the sketch below, it is seen that a rotation, $\Delta\theta$, of the grating corresponds to a rotation $2\Delta\theta$ of the reflected beam with respect to the incident beam. Thus

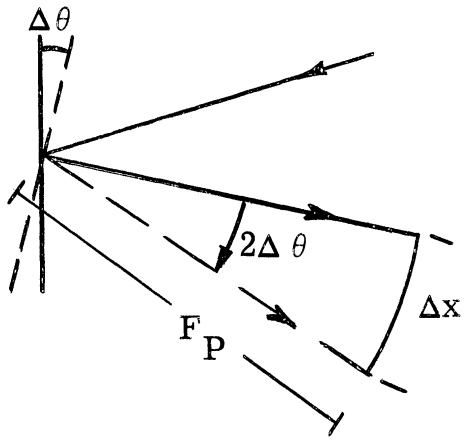

$$\Delta x = 2F_P \, \Delta\theta \tag{D-32}$$

where F_P = 267 mm, the focal length of the parabola. The wavelength interval corresponding to this rotation is given by

$$\Delta\lambda = \frac{d\lambda}{d\theta} \Delta\theta \tag{D-33}$$

The dispersion of the grating is defined as the angular separation of a unit wavelength interval. The higher the dispersion, the easier it is to pick off a small wavelength interval with a finite exit aperture—exit slit width. The reciprocal of the dispersion is obtained from the grating equation[73]

$$\frac{d\lambda}{d\theta} = 2d \cos\theta \qquad (n = 1) \tag{D-34}$$

which at $\lambda = 2.5\mu$ ($\theta = 22.2^{o}$) is

$$\frac{d\lambda}{d\theta} = 6.1\mu/\text{radian} \tag{D-35}$$

The minimum practical exit slit width, Δx, may now be calculated from the system geometry and $\Delta\lambda_{min}$ dictated by the Rayleigh criterion.

The minimum practical slit width is therefore

$$\Delta x_{min} = 2F_P \frac{\Delta\lambda_{min}}{d\lambda/d\theta} \simeq 32\mu \tag{D-36}$$

Setting the slit width below 32μ does nothing to increase resolution but merely diminishes the amount of energy reaching the detector.

Removing the subscripts from Δx and $\Delta\lambda$ in the foregoing equations allows the calculation of $\Delta\lambda$ as a function of Δx. For a slit width setting of 200μ, $\Delta\lambda$ at $\lambda = 2.16\mu$ (second order of the 1.08μ H_e line) is calculated as 0.00233μ. The measured slit function half width for these conditions has been found to be $\Delta\lambda = 0.00234\mu$, a result which indicates the magnitude of the optical imperfections which were neglected in the calculation, (Fig. 44).

Having determined the monochromator response to a delta function, we are in a position to calculate the signal voltage due to a continuous source. If the source spectral radiance is slowly varying compared to $g(\lambda - \lambda')$, the signal voltage is given by (Eq. 21)

$$\Delta V_L(\lambda) = -E\Omega S_1(\lambda)\Lambda(\lambda)\,\bar{I}_\lambda\,\Delta\lambda = -ES_1J \qquad \text{(D-37)}$$

where

$$\Delta\lambda \equiv \int_{-\infty}^{\infty} g(\lambda - \lambda')\,d\lambda' \qquad \text{(D-38)}$$

the spectral slit width.

The source spectral radiance is that of a tungsten filament at 1800^{o}K; $\bar{I}_\lambda = .9$ watts/ster-cm^2-μ. Neglecting the loss on reflection from each mirror, the transmission loss will be due to the Pyrex lamp (72% transmission)

envelope and the germanium filter (90% transmission). Thus

$$\Lambda\ (2.5\mu) = .648 \qquad \text{(D-39)}$$

Thus, for $\Delta x = 200\mu$, f/12 optics

$$J = \overline{I}_\lambda\ \Delta\lambda\Lambda\Omega = 0.9(0.00234)(0.648)\ \frac{\pi}{4(12)^2} \cong 7.4 \times 10^{-6}\ \frac{\text{watts}}{\text{cm}^2} \qquad \text{(D-40)}$$

This is the power density entering the exit slit. Before reaching the detector, however, the system f/ratio is decreased by a factor of 6 by the elliptical mirror. The image on the detector is reduced by a factor of 6 and thus the image area is reduced by 36X. A corresponding 36X increase in power density results. The final power density incident on the detector is therefore

$$J' = 36\ (7.4) \times 10^{-6} = 265\mu\ \text{watts/cm}^2 \qquad \text{(D-41)}$$

The signal voltage due to this radiant power density may now be calculated from Eq. (D-26) or (D-5)

$$\Delta V_L = -S_1\ JE = -(300)\ 2.65 \times 10^{-6}\ (22.5) = -17.8\ \text{mV} \qquad \text{(D-42)}$$

Note: No account need be taken of the duty factor of the chopper since this is taken care of in the determination of S_1. The signal to noise ratio for this operating condition,from Eq. (D-20), is of the order of 2000.

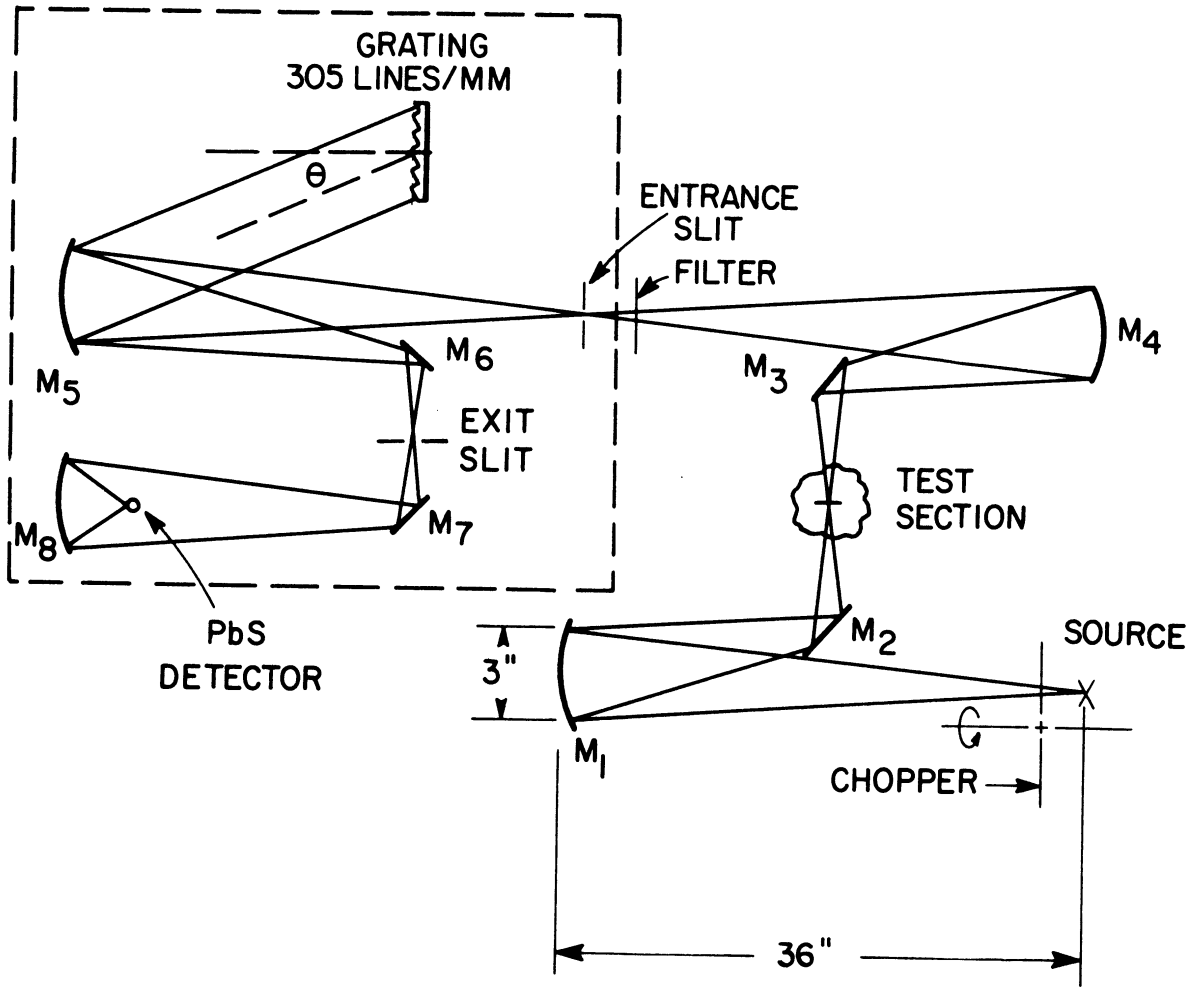

Figure 42. Monochromator and Entrance Optics Physical Schematic

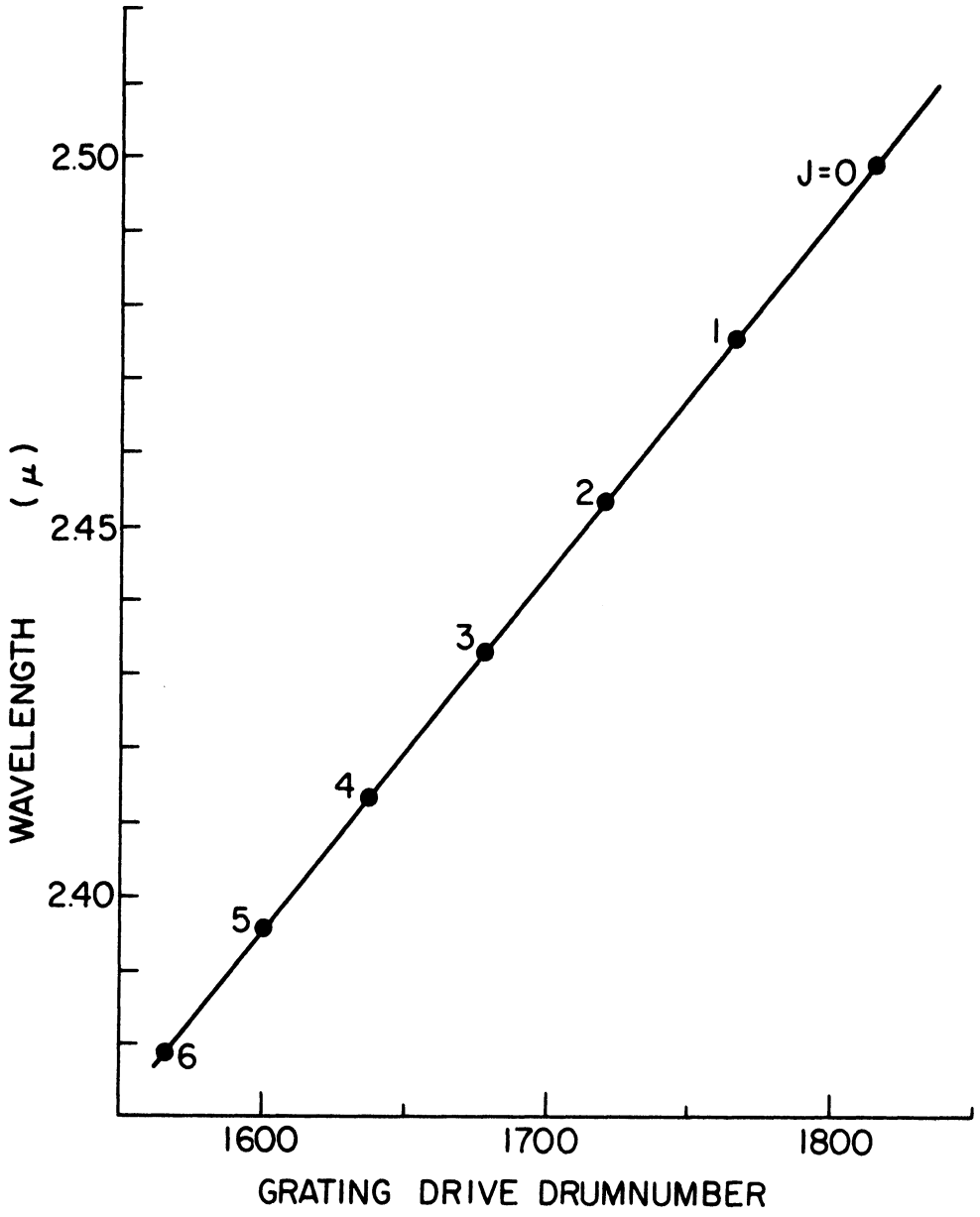

Figure 43. Monochromator Wavelength Calibration Showing Positions of HF R-Branch Rotational Lines

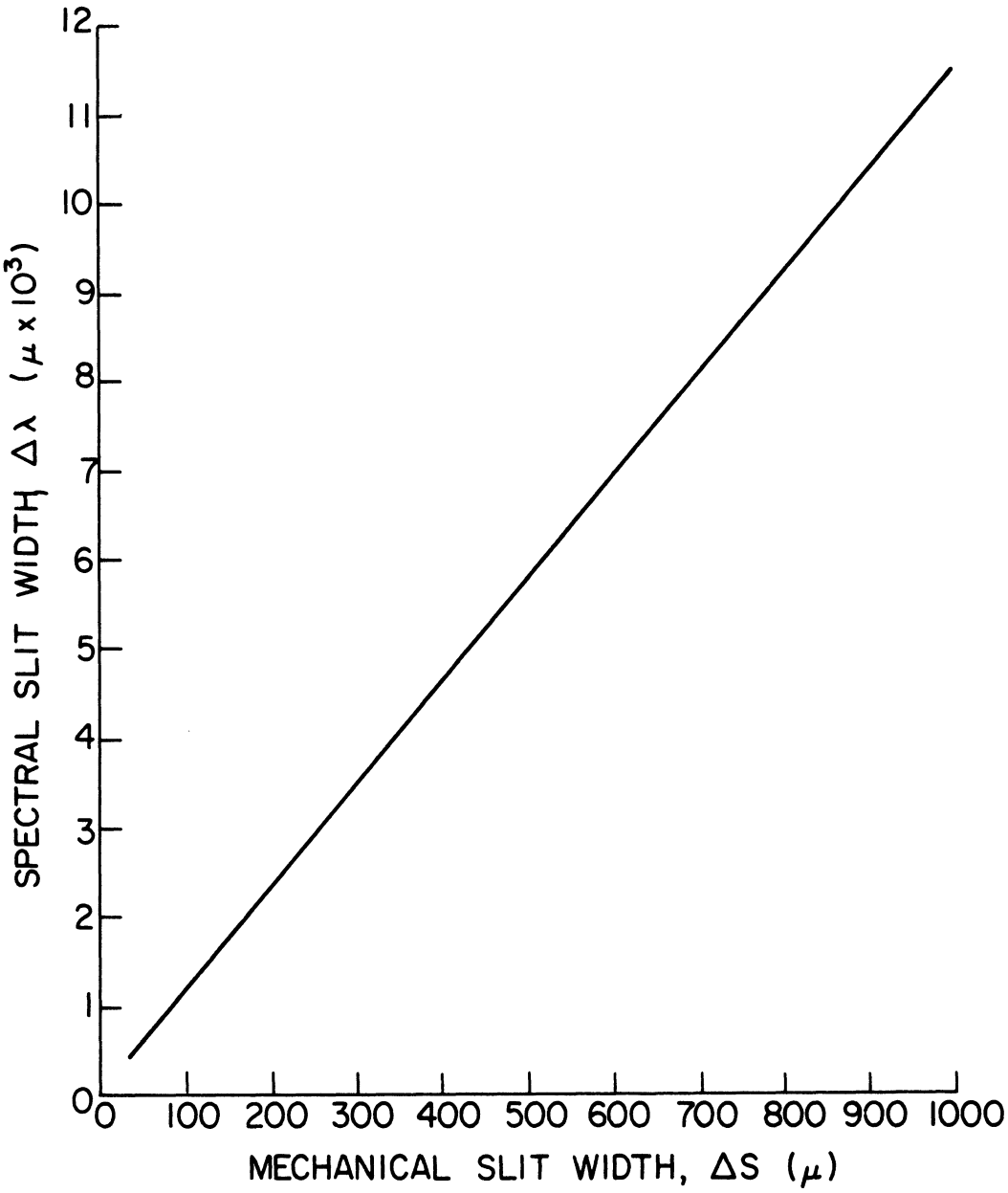

Figure 44. Spectral Slit Width (Resolution) Calibration Using 1.08μ Neon Emission Line

REFERENCES

1. Schlichting, H., Boundary Layer Theory, McGraw-Hill, New York, 1955.

2. Abramovich, G. N., The Theory of Turbulent Jets, M. I. T. Press, 1963.

3. Schetz, J. A., "Analysis of the Mixing and Combustion of Gaseous and Particle-Laden Jets in an Air Stream," AIAA 7th Aerospace Sciences Meeting, New York, January 20-22, 1969.

4. Kline, S. J., "Some Remarks on Turbulent Shear Flows," Proc. Instn. Mech. Engrs., 180, Part 3J, 1965-1966 (AD 663773).

5. Zakkay, V., Krause, E., and Woo, S. D. L., "Turbulent Transport Properties for Axisymmetric Heterogeneous Mixing," AIAA J., 2, 11, November 1964.

6. Boehman, L. I., "An Investigation of Momentum and Mass Transport Properties in Isoenergetic Coaxial Flows," Ph. D. Thesis, Illinois Institute of Technology, 1967.

7. Chriss, D. E., "Experimental Study of the Turbulent Mixing of Subsonic Axisymmetric Gas Streams," AEDC TR 133, Arnold Air Force Station, Tennessee, August 1966, (AD 672975).

8. Ferri, A., "Axially Symmetric Heterogeneous Mixing," PIBAL Rep. 787, Polytechnic Institute of Brooklyn, 1963, (AD 422973).

9. Reichardt, H., Gesetmassigkeiten der freien Turbulenz, VDI-Forschungsheft, 414, 1st ed., Berlin, 1942.

10. Taylor, G. I., "The Transport of Vorticity and Heat through Fluids in Turbulent Motion," Proc. Roy. Soc. London, A135, 1932.

11. Forstall, W. Jr., and Shapiro, A. H., "Momentum and Mass Transfer in Coaxial Jets," J. App. Mech., 17, 12, 1950.

12. Schubauer, G. B., and Tchen, C. M., Turbulent Flow, Princeton Aeronautical Paperbacks, No. 9, Princeton University Press, 1961, p. 99.

13. Morgenthaler, J. H., "Supersonic Mixing of Hydrogen and Air," Ph. D. Thesis, University of Maryland, 1965.

14. Hirschfelder, J. O., Curtiss, C. F., and Bird, R. B., Molecular Theory of Gases and Liquids, Wiley, New York, 1954.

15. Zakkay, V., Sinha, R., and Fox, H., "Some Remarks on Diffusion Processes in Turbulent Mixing," AIAA J., 6, 7, July 1968.

16. Libby, P. A., "Theoretical Analysis of Turbulent Mixing of Reactive Gases with Application to Supersonic Combustion of Hydrogen," ARS J., 32, 3, March 1962.

17. Bhatnagar, P. L., Gross, E. P., and Krook, M., Phys. Rev., 94, 511, 1954.

18. Harlow, F. H., and Nakayama, P. I., "Turbulence Transport Equations," Physics of Fluids, 10, 11, November 1967.

19. Simmons, F. S., "Infrared Spectroscopic Study of Hydrogen Fluorine Flames," Ph. D. Thesis, The University of Michigan, 1966.

20. Meredith, R. E., and Kent, N. F., "Line Strength Calculations for the 0→1, 0→2, 0→3, and 1→2 Vibration-Rotation Bands of Hydrogen Fluoride," Willow Run Laboratories, Report 4613-125-T, The University of Michigan, April 1966.

21. Geister, D. E., "Analysis and Design of a High Pressure A. C. Arc Heater," Aerospace Research Laboratories Report ARL 67-0276, Wright-Patterson Air Force Base, December 1967.

22. LaPointe, C. W., "Supersonic Mixing and Combustion," Air Force Aero Propulsion Laboratory Report AFAPL-TR-68-12, Wright-Patterson Air Force Base, March 1968.

23. Leighton, L. G., "Characteristics of Ribbon Filament Lamps," Illuminating Engineering, LVII, 3, March 1962.

24. Hulburt, E. O., and Granath, L. P., "The Absorption of Light by Fog," Phys. Rev., 34, 140, 1929.

25. Wolff, M., "Die Lichttechnischen Eigenschaften des Nebels," Das Licht, 8, 105-128, 1938.

26. Loehle, F., "Ueber die Lichtzerstreuung im Nebel," Phys. Zeits., 45, 199, 1944.

27. Bulrich, K., "Die Streuung des Lichter in Truber Luft," Optik, 2, 301, 1947.

28. Lambiris, S., and Combs, L. P., "Steady State Combustion Measurements in a LOX/RP-1 Rocket Chamber and Related Spray Burning Analysis," in Detonation and Two-Phase Flow, Ed. S. S. Penner and F. A. Williams, Academic Press, New York, 1962.

29. Dobbins, R. A., "Applications of Light Scattering in Research and Technology," 6th AIAA Aerospace Sci. Meeting, New York., January 1968.

30. Dobbins, R. A., "Remote Size Measurements of Particulate Products of Heterogeneous Combustion," Eleventh Symposium (International) on Combustion, The Combustion Institute, p. 921, 1967.

31. Houghton, H. G. and Chalker, W. R., "The Scattering Cross-section of Water Drops in Air for Visible Light," J. O. S. A., 39, 11, 955-957, 1949.

32. Bracewell, R., The Fourier Transform and its Applications, McGraw-Hill, New York, 1965.

33. Dobbins, R. A. and Jizmagian, S. G., "Optical Scattering Cross Sections for Polydispersions of Dielectric Spheres," J. O. S. A., 56, 10, 1345-1350, 1966.

34. Mugele, R. A., and Evans, H. D., "Droplet Size Distribution in Sprays," Ind. and Eng. Chem., 43, 1317-1324, 1951.

35. Oss, J. P., "Absorption and Emission Coefficient Determination by a Zonal Ring Technique in a Circular Plasma Column," Aerospace Research Laboratories Rep. ARL 66-0110, Wright Patterson Air Force Base, June 1966.

36. Nestor, O. H. and Olsen, N. H., "Numerical Methods for Reducing Line and Surface Probe Data," SIAM Rev., 2, 3, July 1960

37. Bockasten, K., "Transformation of Observed Radiances into Radial Distribution of the Emission of a Plasma," J. O. S. A., 51, 9, September 1961.

38. Bowen, S. W., "A Spectroscopic Study of an Underexpanded Argon Plasma Jet," Ph. D. Thesis, The University of Michigan, 1966.

39a. Becker, H. A., Hottel, H. D., and Williams, G. C., "On the Light-scatter Technique for the Study of Turbulence and Mixing," J. Fluid Mech., 30, 2, 259-284, 1967.

39b. Becker, H. A., Hottel, H. C., and Williams G. C., "The Nozzle-fluid Concentration Field of the Round, Turbulent, Free Jet," J. Fluid Mech., 30, 2, 285-303, 1967.

40. Kling, R., "La Formation et L'Evolution des Brouillards Combustibles," Agardograph 9, Combustion Researches and Reviews, Butterworths Publications, London, 1955.

41. Fraser, R. P., "Liquid Fuel Atomization," Sixth Symposium (International) on Combustion, The Combustion Institution, Reinhold Publishing Corporation, N. Y., 1957.

42. Simmons, F. S., "Spectroscopic Pyrometry of Gases, Flames, and Plasmas," ISA Transactions, 2, 2, 168-189, 1963.

43. Penner, S. S., Quantitative Molecular Spectroscopy and Gas Emissivities, Addison-Wesley, New York, 1959.

44. Mitchell, A. C. G., and Zemansky, M. W., Resonance Radiation and Excited Atoms, Cambridge, 1961.

45. Yamada, H. Y., "Total Radiances and Equivalent Wdiths of Isolated Spectral Lines with Combined Doppler and Collision-Broadened Profiles," Willow Run Research Laboratories Rep. 8416-17-T, The University of Michigan, October 1967.

46. Goldman, A., "On Simple Approximations to the Equivalent Width of a Lorentz Line," J. Q. S. R. T., 8, 829-831, 1968.

47. Simmons, F. S., "Radiances and Equivalent Widths of Lorentz Lines for Nonisothermal Paths," J. Q. S. R. T., 7, 111-121, 1967.

48. Lovell, R. J., and Herget, W. F., "Lorentz Parameters and Vibration-Rotation Interaction Constants for the Fundamental Band of HF," J. O. S. A., 52, 1374-1376, 1962.

49. Sonntag, R. and Van Wylen, G., Fundamentals of Statistical Thermodynamics, Wiley, 1966.

50. Hertzberg, G., Spectra of Diatomic Molecules, Van Nostrand, 1950.

51. Aller, L. H., Astrophysics: The Atmospheres of the Sun and Stars, second ed., The Ronald Press Company, New York, 1963.

52. Benedict, W. S., Herman, R., Moore, G. E., and Silverman, S., "The Strengths, Widths, and Shapes of Infrared Lines, parts I and II," Can. J. Phys., 34, 830-875, 1956.

53. Anderson, A., Chai, An-Ti, and Williams, D., "Self-Broadening Effects in the Infrared Bands of Gases," J. O. S. A., 57, 2, 240-246, 1967.

54. Svehla, R. A., "Estimated Viscosities and Therma Conductivities of Gases at High Temperatures," NASA TR R-132, 1962.

55. Ower, E., and Pankhurst, R. C., The Measurement of Air Flow, Pergamon, Oxford, 1966.

56. ASME Power Test Codes, Supplement on Instruments and Apparatus, Part 5, Measurement of Quantity of Materials, 1949.

57. Tables of Scattering Functions for Spherical Particles, NBS, App. Math. Series 4, Washington, D. C., 1949.

58. Plass, G. N. and Yates, H., "Atmospheric Phenomena," Handbook of Military Infrared Technology, ed. W. L. Wolfe, Superintendent of Documents, U. S. Government Printing Office, Washington D. C., 20402, 1965.

59. Dabora, E. K., Ragland, K. W., and Nicholls, J. A., "Observed Structure of Spray Detonations," Phys. Fluids, 11, No. 11, 1968.

60. Dabora, E. K., Ragland, K. W., Ranger, A. A., and Nicholls, J. A., "Two Phase Detonations and Drop Shattering Studies," The University of Michigan, 06324-2-T, April 1966.

61. Wegener, P. P., and Stein, G. D., "Light Scattering Experiments and Theory of Homogeneous Nucleation in Condensing Supersonic Flow," to be published.

62. McBride, D. D., "The Condensation of a Metal Vapor in a Rapidly Expanding Inert Carrier Gas," Ph. D. Thesis, The University of Michigan, 1969.

63. Ingebo, R. D., "Atomization, Acceleration and Vaporization of Liquid Fuels," Sixth Symposium (International) on Combustion, Reinhold Publishing Corporation, New York, 1957.

64. Roberts, J. H., and Webb, M. J., "Measurement of Droplet Size for Wide Range Particle Distributions," AIAA Journal, 2, 3, 583, 1964.

65. Dobbins, R. A., "Measurement of Mean Particle Size in a Gas-Particle Flow," AIAA Journal, 1, 1940, 1963.

66. Dobbins, R. A. and Strand, L. D., "A Comparison of Two Methods of Measuring Particle Size of Al_2O_3 Produced by a Small Rocket Motor," AIAA Paper No. 69-146, Seventh Aerospace Sci. Meeting, New York, January 1969.

67. Crowe, C. T., and Willoughby, P. G., "A Mechanism for Particle Growth in a Rocket Nozzle," AIAA J., 4, 9, 1677-1678, 1966.

68. Crowe, C. T., and Willoughby, P. G., "A Study of Particle Growth in a Rocket Nozzle," AIAA J., 5, 7 1300-1304, 1967.

69. Jamieson, J. A., McFee, R. H., Plass, G. N., Grube, R. N. and Richards, R. G., Infrared Physics and Engineering, McGraw-Hill, New York, 1963.

70. Chol, R., Marfaing, Y., Munch, S., Thorel, B., and Combette, P., Les Detecteurs de Rayonnement Infra-rouge, Dunod, Paris, 1966.

71. "Kodak Ektron Detectors," The Infrared Laboratories of the Eastman Kodak Company, Rochester, New York.

72. Blackman, R. B. and Tukey, J. W., The Measurement of Power Spectra, Dover, New York, 1958.

73. Sawyer, R. A., Experimental Spectroscopy, Dover, New York, 1963.

74. Slater, L. J., Confluent Hypergeometric Functions, Cambridge University Press, 1960.

Security Classification

DOCUMENT CONTROL DATA - R & D

(Security classification of title, body of abstract and indexing annotation must be entered when the overall report is classified)

1. ORIGINATING ACTIVITY (Corporate author)	2a. REPORT SECURITY CLASSIFICATION
The University of Michigan Ann Arbor, Michigan 48105	Unclassified
	2b. GROUP

3. REPORT TITLE

AN EXPERIMENTAL STUDY OF COAXIAL TURBULENT MIXING OF LIQUID AND GASEOUS FUEL WITH AIR

4. DESCRIPTIVE NOTES (Type of report and inclusive dates)

Second Annual Technical Report 15 November 1967 to 15 November 1968

5. AUTHOR(S) (First name, middle initial, last name)

LaPointe, Clayton W.

6. REPORT DATE	7a. TOTAL NO. OF PAGES	7b. NO. OF REFS
August 1969	198	74

8a. CONTRACT OR GRANT NO.	9a. ORIGINATOR'S REPORT NUMBER(S)
Air Force AF33(615)-67-C-1122	N/A
b. PROJECT NO.	
c. BPS 7(63 301201 62405214)	9b. OTHER REPORT NO(S) (Any other numbers that may be assigned this report)
d.	AFAPL-TR-69-64

10. DISTRIBUTION STATEMENT

This document is subject to special export controls and each transmittal to foreign governments or foreign nationals may be made only with approval of the Air Force Aero Propulsion Laboratory, APRC, Wright-Patterson AFB, Ohio

11. SUPPLEMENTARY NOTES	12. SPONSORING MILITARY ACTIVITY
	Air Force Aeronautical Propulsion Lab. Wright-Patterson AFB, Ohio

13. ABSTRACT

The supersonic mixing of two-phase systems is investigated using a light scattering technique. It is shown that the liquid particle size distribution for sufficiently high Mach number is effectively monodisperse.

From path-integrated measurements at two wavelengths in the IR region, the radial distribution of particle density is obtained by Abel inversion. It is shown that two distinct regions of the coaxial jets exhibit similarity behavior and that centerline density decay and mixing radii follow power law relations. It is also shown that centerline density may be obtained without Abel inversion.

A non-interfering diagnostic system utilizing absorption spectroscopy and a tracer gas (HF) has also been developed to study gas-gas axisymmetric mixing. Functions are developed for the interpretation of absorption data in terms of absorber density and temperature.

DD FORM 1 NOV 68 1473

UNCLASSIFIED

Security Classification

14. KEY WORDS	LINK A		LINK B		LINK C	
	ROLE	WT	ROLE	WT	ROLE	WT
Turbulence						
Axisymmetric Mixing						
Spectroscopy						
Scattering						

DISTRIBUTION LIST

	Addressee	No. Of Copies
1.	AFAPL (APRT) Wright-Patterson AFB, Ohio 45433 (Plus One Reproducible)	10
2.	AFAPL (APRA) Wright-Patterson AFB, Ohio 45433	1
3.	ASD (ASNPD-30) Wright-Patterson AFB, Ohio 45433	1
4.	NASA Flight Research Center Attn: Technical Librarian Box 273 Edwards, California 93523	1
5.	NASA Marshall Space Flight Center Attn: Technical Librarian Huntsville, Alabama 35800	1
6.	Headquarters Foreign Technology Division Air Breathing & Elec. Prop. Div. (TDEPA) Wright-Patterson AFB, Ohio 45433	1
7.	Arnold Engineering Development Center (AEDC) Attn: Administration & Engr. Bldg. Tech. Library (AEDIM) Arnold AFS, Tennessee 37388	1
8.	NASA Ames Research Center Attn: Hypersonic Aerodynamics Branch Moffitt Field, California 94035	1
9.	NASA Lewis Research Center Attn: Technical Librarian 2100 Brookpark Road Cleveland, Ohio 44135	1

Distribution List

	Addressee	No. Of Copies
10.	NASA Langley Research Center Attn: Technical Librarian Langley Field, Virginia 23365	1
11.	Aerospace Research Laboratories (ARL) Chemistry Research Lab. (ARC) Building 450 Wright-Patterson AFB, Ohio 45433	1
12.	The Rand Corporation Attn: Technical Librarian 1700 Main Street Santa Monica, California	1
13.	NASA Headquarters Attn: Technical Librarian 1512 "H" Street N. W. Washington, D. C.	1
14.	Republic Aviation Corporation Attn: Technical Library Farmingdale, L. I. New York 11735	1
15.	Air University Library Maxwell AFB, Alabama 36112	1
16.	ASD, Research & Technology Division Systems Engineering Group Technical Information Division (SEPDE)	1
17.	The Martin Company, Denver Division Attn: Res. Library, A-52 P. O. Box 179 Denver, Colorado 80201	1
18.	Defense Documentation Center Cameron Station 5010 Duke Street Alexandria, Virginia 22314	20

Distribution List Continued:

	Addressee	No. Of Copies
19.	Boeing Corporation Aerospace Division Attn: Technical Librarian P. O. Box 3707 Seattle, Washington 98124	1
20.	Douglas Aircraft Company, Inc. Missile & Space System Division Attn: Aerophysics Laboratory 2332 E. El Segundo Blvd. El Segundo, California	1
21.	General Dynamics/Convair Attn: Technical Librarian P. O. Box 1950 San Diego, California	1
22.	North American Aviation, Inc. Los Angeles Division Attn: Technical Librarian 5610 Imperial Highway Los Angeles, California	1
23.	HQ. USAF (AFCSAI) Washington, D. C. 20330	1
24.	Department of The Navy Office of Naval Research Attn: Code 429 - Head Power Branch of Material Sciences Division Washington, D. C. 20360	1
25.	Naval Air Systems Command Department of The Navy Attn: AIR-330 Technology Administration Propulsion Washington, D. C. 20360	1
26.	Naval Air Systems Command Department of The Navy Attn: AIR-5367 - Component Technology Branch of Propulsion Division Washington, D. C. 20360	1

Distribution List Continued:

	Addressee	No. Of Copies
27.	Naval Ordnance Systems Command Department Of The Navy Attn: ORD - 0331 - Research and Technology Division Propulsion & Propellant Branch Washington, D. C. 20360	1
28.	Naval Weapons Laboratory Attn: Technical Library Dahlgram, Virginia	1
29.	Ling-Temco - Vought, Inc. LTV Astronautics Division Attn: Technical Librarian P. O. Box 5907 Dallas, Texas 75222	1
30.	Lockheed Missiles & Space Company Propulsion Engineering Division Attn: Technical Librarian 1111 Lockheed Way Sunnyvale, California 94087	1
31.	Bell Aerosystems Attn: Technical Librarian Box 1 Buffalo, New York 14205	1
32.	General Electric Company Flight Propulsion Division Attn: Technical Information Center Evendale Cincinnati, Ohio 45215	1
33.	United Aircraft Corporation Pratt & Whitney Aircraft Division Attn: Technical Librarian 400 Main Street East Hartford, Connecticut 06108	1
34.	Applied Physics Laboratory The Johns Hopkins University Attn: Document Librarian 8621 Georgia Avenue Silver Spring, Maryland 20910	1

Distribution List Continued:

	Addressee	No. Of Copies
35.	McDonnell Company Attn: Technical Library P. O. Box 516 St. Louis, Missouri 63166	1
36.	The Marquardt Corporation Attn: Technical Library 16555 Saticoy Street Van Nuys, California 91409	1
37.	Cornell Aeronautical Laboratory Inc. Hypersonic Facilities Department Attn: Mr. J. F. Martin, Head P. O. Box 234 Buffalo, New York 14221	1
38.	Arnold Engineering Development Center (AEDC) HQ. AEDC Attn: AERL (F. Smith) Arnold AFS, Tennessee 37388	1

UNIVERSITY OF MICHIGAN
3 9015 03466 2182